ADVANCEMENT IN BIOMEDICAL MAGNETIC RESONANCE IMAGING AND SPECTROSCOPY

by

Bijaya Thapa

A dissertation submitted to the faculty of
The University of Utah
in partial fulfillment of the requirements for the degree of

Doctor of Philosophy

in

Physics

Department of Physics and Astronomy

The University of Utah

December 2017

THE UNIVERSITY OF UTAH GRADUATE SCHOOL

STATEMENT OF DISSERTATION APPROVAL

The following faculty members served as the supervisory committee chair and members for the dissertation of **Bijaya Thapa**

Dates at right indicate the members' approval of the dissertation.

Christoph Boehme	, Chair	**08/29/2017** Date
Eun-Kee Jeong	, Member	**08/29/2017** Date
Dennis L. Parker	, Member	**08/29/2017** Date
Anil Seth	, Member	**08/29/2017** Date
Gernot Laicher	, Member	**08/29/2017** Date

The dissertation has also been approved by **Benjamin C. Bromley**

Chair of the Department of **Physics and Astronomy**

and by **David B. Kieda**, Dean of The Graduate School.

ABSTRACT

This dissertation comprises two separate studies: 1) efficacy of an anabolic steroid, oxandrolone, on the energy utilization of the heart of a lamb born with single ventricle (SV) physiology using ^{31}P MR spectroscopy (MRS) and 2) signal behavior of ultra-high-b radial diffusion weighted imaging (UHb-rDWI) in healthy and multiple sclerosis (MS) subjects.

SV infants have the highest mortality of all infants that have congenital heart defects. Their inability to gain weight appropriately may be due to high cardiac energy requirements from their shunt dependent physiology. We hypothesize that oxandrolone, which is already known to markedly improve the nutritional state of burn patients, will improve the energy utilization in the heart. We tested our hypothesis on SV modelled lambs using ^{31}P MRS, home built $^{1}H/^{31}P$ double tuned radio frequency (RF) coil, and ^{1}H and ^{31}P T/R switches. We monitored cardiac energy in the lamb by quantitatively evaluating the first-order forward reaction rate (k_f) of the creatine-kinase (CK) reaction in the heart.

Spinal cord injury due to pathologies, such as MS, may include demyelination and/or axonal damage and lead to varying degrees of neurologic deficit. Noninvasive imaging biomarkers for earlier disease detection and monitoring in the follow-up and treatment stages would be a significant advancement in patient care. Moreover, imaging of the cervical spinal cord (CSC) is technically challenging because of the low signal to

noise ratio from the small cross section of the cord, susceptibility artifact due to tissue-bone interface, and motion induced artifact from breathing and swallowing. To resolve these challenges, we used the UHb-rDWI technique and a CSC dedicated phased array RF coil. We studied the behavior of UHb-rDWI signal over the range of b-values from 0 sec/mm^2 to 7348 sec/mm^2 in the CSC of healthy and MS subjects over multiple time points. In the normal CSC, the signal decays fast at low b and slowly at UHb (b>4000 sec/mm^2). In MS patients, the region affected by active lesions revealed a marked decrease in signal intensities in UHb region. UHb-rDWI could, therefore, be used for establishing an imaging biomarker to distinguish inflammation, demyelination, and axonal loss in the CSC.

To my grandparents, parents, and my wife

CONTENTS

LIST OF TABLES

LIST OF ACRONYMS

PBS	Phosphate Buffered Saline
SV	Single Ventricle
CSI	Chemical Shift imaging
MRI	Magnetic Resonance Imaging
MRS	Magnetic Resonance Spectroscopy
NMR	Nuclear Magnetic Resonance
FID	Free Induction Decay
SE	Spin Echo
RF	Radio Frequency
ROI	Region of Interest
TR	Repetition Time
TE	Echo Time
T/R	Transmit/Receive
FOV	Field of View
NF	Noise Figure
SNR	Signal to Noise Ratio
2D	Two-Dimensional
ADC	Apparent Diffusion Coefficient
SC	Spinal Cord

CSC	Cervical Spinal Cord
DWI	Diffusion Weighted Imaging
MD	Mean Diffusivity
FA	Fractional Anisotropy
WM	White-Matter
GM	Gray-Matter
STE	Stimulated Echo
UHb	Ultra-High-b
UHb-rDWI	Ultra-High-b-Radial Diffusion Weighted Imaging
IA	Intra Axonal
EA	Extra Axonal
FA	Fractional Anisotropy
MD	Mean Diffusivity
T_1	Spin-Lattice Relaxation Time Constant
T_2	Spin-Spin Relaxation Time Constant

ACKNOWLEDGEMENTS

I would like to express my deepest gratitude to my advisor, Prof. Eun-Kee Jeong, for his exemplary guidance, care, and constant encouragement since I joined my current lab. I was so fortunate to experience and learn from his knowledge, patience, and critical thinking which led to the completion of this study. I cannot forget to thank to all my supervisory committee members: Prof. Christoph Boehme, Prof. Dennis L Parker, Prof. Anil Seth, and Prof. Gernot Laicher for their support and valuable suggestions. I must express my sincere thanks to Prof. John Rose, Prof. Lubda M. Shah, and Prof. Deborah Frank for their research guidance, suggestions, and fruitful discussions. The research was generously supported by Alice and Kevin Steiner. I would like to acknowledge their support with immense gratitude.

My completion of this project could not have been accomplished without the support of my current group members, Dr. Nabraj Sapkota, YouJeong Lee, and Kyle Jeong. I would like to offer my special thanks to Michael Mozdy and Colton Thronley for proof reading the thesis. I would not forget my former group members Dr. Xianfeng Shi, who always motivated me to work hard and helped me whenever I was in need. I would like to thank KC Erb, who as a good friend was always willing to help correct my English not only in some of my papers but also in daily speech. I also thank my colleagues from another group at UCAIR, Dr. Joshua Kaggie and Michael Beach and visiting scholar Yukio Kaneko from Hitachi Company, Japan for their amazing help in discussing MRI

hardware. I am indebted to my grandparents, parents, parent in laws, brothers, sister and family members for their love and inspiration with their best wishes. I would like to express my gratitude to my caring and loving wife, Sangita Baniya, for her continuous support and encouragement during my studies. I would like to thank my beloved little son Rayansh Thapa who always relieves my tiredness after my work in the evening and refreshes my morning with his sweet smile, hug, babbling, and playful activities.

Finally, a special thanks goes to my father, Tapta Bahadur Thapa, for his persistent guidance, support, and motivation for fighting against challenges since my childhood. You are the one who led me to accomplish this degree.

CHAPTER 1

INTRODUCTION

1.1 Motivations

This dissertation describes two separate studies: the first examines ^{31}P spectroscopy in a lamb model of single ventricle (SV) physiology, and the second applies our new technique Ultra-High-b Radial Diffusion Weighted Imaging (UHb-rDWI) for the cervical spinal cord of healthy control human volunteers and multiple sclerosis (MS) patients to detect, differentiate, and quantitate demyelination, axonal loss and remyelination.

1.1.1 ^{31}P Spectroscopy

The normal heart has four chambers: the upper two chambers, called atria, receive blood into the heart and the lower two, called ventricles, pump blood out of the heart to the lung and body. In the cardiac cycle, deoxygenated blood from different parts of the body moves in to the right atrium, then to the right ventricle, and then is pumped out through the pulmonary artery into lung. Oxygenated blood from the lung goes into the left atrium and then to the left ventricle and then is pumped out to the body through the aorta.

Single ventricle physiology is a heart defect that causes the complete mixing of

oxygenated and deoxygenated blood at the arterial or ventricular level. The blood exiting from the heart with SV physiology either gets directed to the lungs or the body. Various forms of SV physiology include: 1) hypoplastic left heart syndrome in which the left side of the heart is underdeveloped such that the left ventricle cannot pump blood to the body, 2) tricuspid atresia in which the tricuspid valve (valve between the right atrium and the right ventricle) is either missing or abnormally developed by partially or completely blocking the blood flow from the right atrium to the right ventricle, 3) atrioventricular septal defect which is the lack of separation of atria or ventricles, 4) double outlet right ventricle in which both the pulmonary artery and the aorta are connected to the left ventricle so that oxygen poor blood is circulated in the body, 5) Ebstein's anomaly in which the tricuspid valve either sits lower than normal in the right ventricle or its leaflets are abnormally developed resulting in leaking back of the blood through the valve and leading to enlargement of the heart or heart failure, and 6) pulmonary atresia in which the pulmonary valve (located between the right ventricle and the pulmonary artery) is either missing or so small that the right ventricle cannot efficiently pump deoxygenated blood to the lungs.

Advances in surgical and critical care over the past two decades have markedly improved outcomes for children with SV physiology. Yet children with excellent technical repairs slowly deteriorate in the postoperative period from multiple causes, including wound infections, prolonged effusions, prolonged mechanical ventilation and venous thrombosis. One feature common to virtually all of these complications is that they occur in the presence of poor nutrition, and thus inadequate growth is likely an important risk factor for morbidity in this population. However, promoting growth in

these children has proven difficult by common methods like increasing calories or changing of feeding methods, leading clinicians to search for alternatives. Oxandrolone is an anabolic steroid that has markedly improved the nutritional state of burn patients, resulting in increased lean body mass, less time on the ventilator, and better wound healing. We theorize that oxandrolone will have a similar impact on SV patients recovering from complex repairs. Specifically, it will prevent the development of a catabolic state thereby decreasing the incidence of malnutrition-related complications and death in the postoperative period.

A noninvasive method to monitor the progression of the disease with oxandrolone treatment is crucial to study the efficacy of the steroid. ^{31}P magnetic resonance spectroscopy (MRS) is the only noninvasive method proven to quantitatively assess the improvement in cardiac energy utilization due to oxandrolone by measuring the rate of production of adenosine tri phosphate (ATP), a prime energy source of all cellular activities in the body (1,2). In order to obtain ^{31}P spectroscopy data and analyze them, appropriate MR pulse sequences, hardware, and postprocessing software are required.

Because of short T_2 of the ^{31}P in the phosphorus metabolite, a pulse sequence with short TE ~ 10 ms such as free induction decay (FID) is required to acquire the ^{31}P spectrum. Multivoxel techniques such as chemical shift imaging (CSI) have been commonly used to acquire ^{31}P spectra (3). In CSI, an FID is acquired by applying an excitation pulse followed by phase encoding in one, two, or three directions. However, acquisition time increases proportionally with the number of phase encoding dimensions used in CSI rendering 2D and 3D CSI acquisition time impractically long for *in vivo* application. In this regard, 1D CSI is a good alternative for the ^{31}P spectroscopy of the *in*

vivo heart. Moreover, the ^{31}P signal from the chest muscle is much higher than that from the heart. So, in order not to contaminate the signal from heart with that from the chest muscle, it is imperative to suppress the ^{31}P signal from the chest muscle by using techniques such as slice-selective presaturation pulse.

The low concentration of the ^{31}P metabolites and small gyromagnetic ratio of the ^{31}P compared to the ^{1}H in the human body causes low signal to noise ratio (SNR) of the ^{31}P signal in the heart. In order to overcome this obstacle, researchers must use an optimized and heart-dedicated radio frequency (RF) coil and transmit/receive (T/R) switch. Due to low SNR of the ^{31}P signal, ^{1}H magnetic resonance imaging (MRI) is inevitable for localization and shimming the region of interest. So, in order to perform ^{31}P MRS, a $^{1}H/^{31}P$ double-tuned coil with associated T/R switch plus an additional circuitry that automatically routes the ^{1}H RF pulse to the ^{1}H T/R switch during ^{1}H MRI and the ^{31}P RF pulse to the ^{31}P T/R switch during ^{31}P MRS is needed.

1.1.2 Ultra-High-b Radial Diffusion Weighted Imaging (UHb-rDWI)

The spinal cord extends from the brainstem to its termination in the conus medullaris in the upper lumber spine where it forms the cauda equina. It is the major pathway for communication between the brain and peripheral organs. The cervical section of spinal cord consists of butterfly shaped gray-matter at the core surrounded by a rim of white-matter. The white-matter is comprised of myelinated axons for ascending and descending tracts. The sensory tract primarily occupying the dorsal and external lateral portion of the cord carries the signal to the brain while the motor tracts (ventral and interior lateral portions) carry commands to the effector organs (4). The gray-matter

consists of glial cells, synapses, capillaries, and neurons for brain and autonomic functions.

Injury to the spinal cord results in serious clinical consequences for patients such as weakness or paralysis of the limbs and trunk, with sensory disturbance and dysfunction of the gastrointestinal and genitourinary sphincters (5). Researchers have yet to develop a sensitive, noninvasive technique that can detect the disease at an early stage when clinical symptoms are vague and monitor the disease evolution and treatment. MRI is a noninvasive method that provides an excellent soft tissue contrast and spatial resolution of the spinal cord (6). However, conventional MRI techniques such as T_1- and T_2-weighted imaging are limited in their ability to detect the very early stage of the disease. Diffusion tensor imaging (DTI) has been evolving as a promising method to evaluate spinal cord diseases via the quantitative assessment of DTI indices such as radial diffusivity, axial diffusivity, fractional anisotropy, and mean diffusivity by applying a low-b diffusion weighting gradient. The temporal change in these indices may be used to monitor the progression of the diseases or response to the treatment of the diseases (5). However, DTI correlates poorly with axonal pathology and its results are not always consistent in detecting the axonal dysfunction (7,8). Researchers have begun to investigate high-b and even ultra-high-b ($b > 4000$ sec/mm^2) radial diffusion weighted imaging (UHb-rDWI). Using radial UHb diffusion gradients and echo time of ~70 ms, the signal from extra axonal space and myelin can be completely suppressed to noise level leaving the signal contributed only from intra-axonal water. This effect occurs because the applied radial UHb gradient does not create a noticeable phase dispersion for the spins in restricted water molecules in the intra-axonal space whose motion along the

radial direction is limited by axonal diameter, while it does create a phase dispersion for the spins in mobile water molecules in extra-axonal space.

However, UHb-rDWI of the spinal cord is challenging due to the small cross section, motion artifacts from cerebrospinal fluid (CSF) flow with each cardiac and respiratory movement, and susceptibility artifacts due to tissue-bone interface (9–11). A spin echo-type sequence fails to preserve signal because the UHb gradient in clinical scanners with gradient field strength of 40 mT/m requires a long echo time. Therefore, a stimulated echo-type sequence must be used. Similarly, a single shot diffusion weighted sequence with echo planar imaging read out and reduced field of view in phase encoding direction is commonly employed to get rid of motion and susceptibility related artifacts (12–15). The SNR from the small imaging field of view of the spinal cord acquired within the clinical time frame can be improved using phased array coil optimized at the depth of spinal cord.

1.2 Outline of Dissertation

There are six chapters in this dissertation. Chapter 1 is the introduction. Chapter 2 introduces basic principles and theories of magnetization – both quantum and classical approaches – for each quantitative technique used in the dissertation. The design and development of MRI hardware such as different radio frequency (RF) coils and their interfaces are detailed as well.

Chapter 3 describes the design and construction of our general purpose T/R switch, the high power RF switch for automatic switching of RF pulses in dual nuclei experiment, and the $^{1}H/^{31}P$ double-tuned RF coil dedicated to the lamb's heart. The T/R

switch board is versatile in the sense that the same board can be used to build the T/R switch compatible for a linear, quadrature, and double tuned RF coils of any frequency. The T/R switch and RF coil designed and built in this chapter are mainly for the ^{31}P spectroscopy of a lamb's heart in Chapter 4.

Chapter 4 presents the efficacy of oxandrolone on cardiac energy utilization in the SV lamb through the measurement of the first-order forward reaction rate constant, k_f, of the creatine kinase reaction in the lamb heart using our custom $^{1}H/^{31}P$ double-tuned coil, T/R switches, and magnetization transfer ^{31}P-MR spectroscopy (MT-^{31}P-MRS). Four groups of lambs, control, shunted, oxandrolone-treated shunt, and oxandrolone-treated control, were created and k_f was measured in each group and compared.

In Chapter 5, behavior of UHb-rDWI signal in healthy volunteers and multiple sclerosis (MS) patients is presented. The UHb-rDWI signal was measured using 2D single-shot diffusion weighted stimulated EPI with reduced field of view (2D ss-DWSTEPI-rFOV) pulse sequence and custom spinal cord-dedicated RF coil. The volunteers and the patients were imaged multiple times to study the repeatability of the technique in the case of healthy volunteers and the progression of the disease and the response of medicine in the case of patients. Comparison of the signal behavior of lesion region with heathy region of the same patient or similar region of healthy controls gives the information about severity.

Finally, Chapter 6 summarizes the overall achievements, limitation of the dissertation and suggestions for future work.

CHAPTER 2

PRINCIPLES OF MAGNETIC RESONANCE IMAGING AND SPECTROCOPY

2.1 Nuclear Magnetic Resonance

2.1.1 Introduction

Magnetic resonance imaging and spectroscopy (MRI and MRS) are noninvasive methods, based on the principle of nuclear magnetic resonance (NMR), to study the internal anatomy and physiology of living organisms and *ex vivo* specimens (16). NMR is a phenomenon happening in nuclear magnetic system having nuclear magnetic moment and angular momentum. The nuclear magnetic moment of an atomic nucleus arises from the spin of the nucleons. When such a magnetic system is placed in an external static magnetic field (B_0), the magnetic moment vector prefers aligning in the direction of the field. When a radio frequency (RF) pulse, which is capable of producing an oscillating magnetic field (B_1) in the direction perpendicular to the B_0 field, is irradiated, the magnetic moments nutate down to the transverse plane. The energy released when these magnetic moments go back to the original state (B_0 field direction) is responsible for producing NMR absorption spectra. Pieter Zeeman in 1896 first observed the splitting of energy levels of a magnetic system, called Zeeman splitting and this splitting is proportional to the externally applied magnetic field. The beauty of these resonance methods is that we can selectively study a specific spin-system within many

heterogeneous magnetic systems.

2.1.2 Classical Description of NMR

The magnetic moment $\vec{\mu}$ of the magnetic system consisting of many nuclei coupled together is related to the total angular momentum vector $\vec{J}$ by the relation:

$$\vec{\mu} = \gamma \vec{J}, \qquad [2.1]$$

where γ is the "gyromagnetic ratio" (also known as "magnetogyric ratio") and its value is nucleus dependent. Another commonly used constant is ɣ which is related with γ by

$$ɣ = \frac{\gamma}{2\pi}. \qquad [2.2]$$

In quantum theory, an atomic nucleus having a non-zero spin quantum number I is related to the absolute value of total angular momentum by

$$|\vec{J}| = \hbar\sqrt{I(I+1)}, \qquad [2.3]$$

where $\hbar$ *(= h/2π = 1.05 x 10^{-34} Js)* is the reduced Planck's constant or Dirac constant and *h* is Planck's constant. The spin quantum number *I* can be zero, integer, or half integer, and for any particular nucleus, its value holds the following three basic rules: *I* is 1) half integer for nuclei with uneven mass numbers such as ^{1}H, ^{31}P, and ^{19}F, 2) integer for nuclei with even mass numbers but uneven proton numbers such as ^{2}H, ^{14}N, and ^{6}Li, and 3) zero for nuclei with even mass numbers and even number of protons such as ^{4}He, ^{12}C, and ^{16}O. Substituting Eq. [2.3] into Eq. [2.1], the relation of $|\vec{\mu}|$ in terms of *I* can be written as

$$|\vec{\mu}| = \gamma\hbar\sqrt{I\,(I+1)}\,. \qquad [2.4]$$

The value of γ and *I* of some of the most common MRI active nuclei found in the human body with their natural abundance and elemental abundance are listed in Table 2.1.

Table 2.1: List of some MR active nuclei found in the human body with their spin, gyromagnetic ratio, natural, and elemental abundances.

Nucleus	Spin quantum number (I)	Gyromagnetic ratio (ɤ) (MHz/T)	Natural abundance (%)	Elemental abundance in the human body (%)
^{1}H	1/2	42.58	99.985	63
^{31}P	1/2	17.25	100	0.24
^{23}Na	3/2	11.27	100	0.041
^{14}N	1	3.08	99.63	1.5
^{13}C	1/2	10.71	1.11	9.4
^{17}O	5/2	-5.77	0.037	26

A nucleus with non-zero spin quantum number when placed in an external homogeneous magnetic field $\vec{B}$, experiences a torque given by:

$$\vec{\tau} = \vec{\mu} \times \vec{B}\,, \qquad [2.5]$$

and a potential energy given by:

$$U = -\vec{\mu}\,.\vec{B}. \qquad [2.6]$$

The z component of nuclear magnetic moment of Eq. [2.4] is

$$\mu_z = \hbar\gamma I_z \equiv \gamma m\hbar\,, \qquad [2.7]$$

where m = I, I – 1, …, -I is magnetic spin quantum number. Assuming $\vec{B}$ is along the z direction i.e., $\vec{B} = B_0\,\hat{z}$ and with Eq. [2.7], Eq. [2.6] can be written as:

$$U_m = -\gamma m\hbar B_0. \qquad [2.8]$$

When I=1/2, m = $\pm$ ½, the energy level splits into two energy levels in the presence of an external magnetic field as shown in Figure 2.1. The magnetic moment of the spins is oriented parallel to the field in lower level and antiparallel in the upper level. This splitting of the energy levels in the presence of an external non-zero magnetic field is called Zeeman splitting. As seen from Eq. [2.8], the separation between the Zeeman sublevels is a function of the magnetic field.

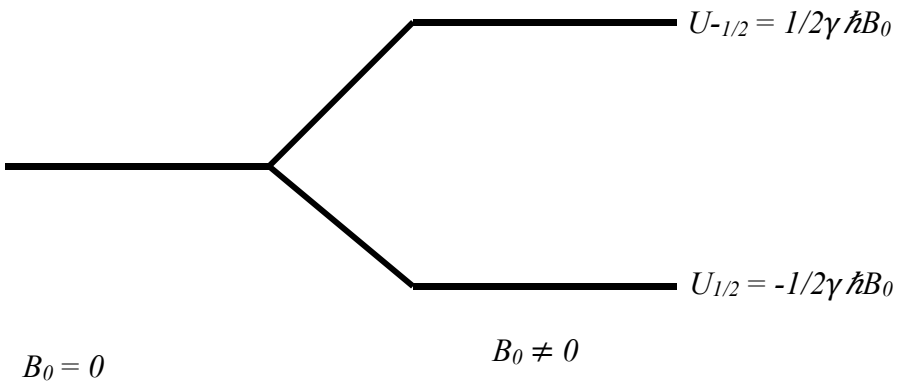

Figure 2.1: The Zeeman splitting of a spin-half system in a non-zero magnetic field.

The difference in energy of the two levels is:

$$\Delta U_{1/2,-1/2} = \gamma \hbar B_0 = \hbar \omega_L. \quad [2.9]$$

This equation yields

$$\omega_L = \gamma B_0. \quad [2.10]$$

This is the frequency at which the nucleus precesses about the external magnetic field, called the Larmor frequency, named after Joseph Larmor. The Larmor frequency can be explained using a classical model in which the time derivative of angular momentum yields the torque:

$$\vec{\tau} = \frac{d\vec{L}}{dt} = \frac{1}{\gamma}\frac{d\vec{\mu}}{dt}. \quad [2.11]$$

From Eqs. [2.5] and [2.11] we find

$$\frac{d\vec{\mu}}{dt} = \gamma\, \vec{\mu} \times \vec{B}. \quad [2.12]$$

In an NMR experiment, we observe the effect of all nuclei not of a single nucleus. In the absence of an external magnetic field, the magnetic moments orient in a random direction so that the net magnetization becomes zero. However, in the presence of the applied field, these magnetic moments align in the field direction there by

producing bulk magnetization of the sample. Using the Boltzmann distribution: exp(-$E_m/KT)/\sum_m \exp(-E_m/KT)$, the bulk magnetization for a spin I system in an external magnetic field B_0 can be calculated as follows:

$$M = N\gamma\hbar \frac{\sum_{m=-I}^{I} m \exp(\gamma\hbar m B_0/KT)}{\sum_{m=-I}^{I} \exp(\gamma\hbar m B_0/KT)} = \frac{N\gamma^2\hbar^2 I(I+1)B_0}{3KT} . \quad [2.13]$$

This is Curie's law of magnetization. In terms of bulk magnetization $\vec{M}$, Eq. [2.12] can be written as:

$$\frac{d\vec{M}}{dt} = \gamma \vec{M} \times \vec{B} . \quad [2.14]$$

Suppose $\vec{B} = B_0\hat{z}$, using Eq. [2.10], Eq. [2.14] becomes:

$$\frac{d\vec{M}}{dt} = \omega_L \vec{M} \times \hat{z} . \quad [2.15]$$

In component from, Eq. [2.15] can be rewritten as:

$$\begin{aligned} \frac{dM_x}{dt} &= \omega_L M_y \\ \frac{dM_y}{dt} &= -\omega_L M_x \\ \frac{dM_z}{dt} &= 0 . \end{aligned} \quad [2.16]$$

Differentiating the first two equations of Eq. [2.16] and rearranging we get,

$$\begin{aligned} \frac{d^2M_x}{dt^2} &= -\omega_L^2 M_x \\ \frac{d^2M_y}{dt^2} &= -\omega_L^2 M_y \\ \frac{dM_z}{dt} &= 0 . \end{aligned} \quad [2.17]$$

The first two equations of Eq. [2.17] are equations of simple harmonic motion. One easy way to solve these second-order differential equations is to consider the solution in the form $Acos(\omega_L t) + Bsin(\omega_L t)$ and setting initial boundary conditions

M(t=0) = ($M_x(0)$, $M_y(0)$, $M_z(0)$), we can write the solutions of Eq. [2.17] as:

$$M_x(t) = M_x(0)\cos(\omega_L t)$$

$$M_y(t) = -M_y(0)\sin(\omega_L t) \qquad [2.18]$$

$$M_z(t) = M_0(0)$$

This equation indicates that the magnetization vector sweeps out a cone of constant angle to the direction of magnetic field with the Larmor frequency as shown in Figure 2.2.

When the spin system is placed under the influence of an oscillating magnetic field of amplitude B_1 and carrier frequency ω, *i.e.*, $\vec{B}_1(t) = B_1 \cos(\omega t)\hat{x}$ in addition to the static magnetic field $B_0\hat{z}$, the equation of motion [2.14] for the spin system can be written as:

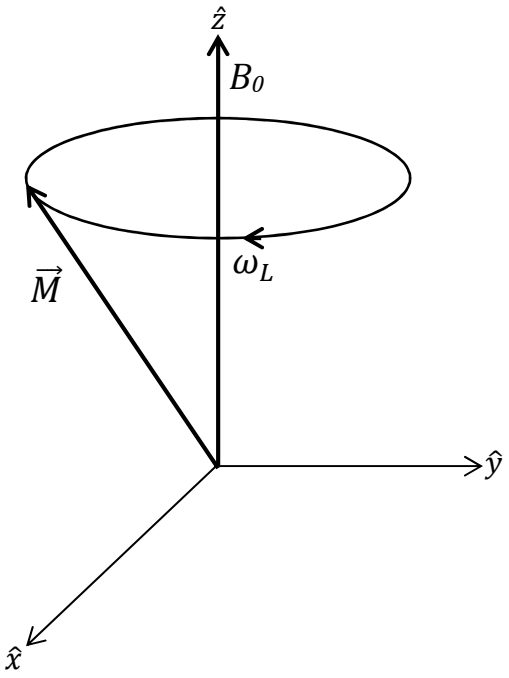

Figure 2.2: Larmor precession of the magnetization vector around an external magnetic field.

$$\frac{d\vec{M}}{dt} = \gamma\, \overrightarrow{M} \times (B_0\hat{z} + \vec{B}_1(t)\,) \qquad [2.19]$$

2.1.3 Quantum Mechanical Description of NMR

We have discussed that the spin in a static magnetic field has Zeeman energy in terms of quantum number m, which is the eigenvalue of I in the direction of applied field B_0, i.e.,

$$E_m = -\gamma m\hbar B_0. \qquad [2.20]$$

The corresponding eigenfunction obtained by solving the time-dependent Schrödinger equation can be written as

$$\Psi(t) = \sum_{m=-I}^{I} c_m u_{I,m} e^{-(i/\hbar)E_m(t)}\,, \qquad [2.21]$$

where c_m is the complex normalization constant for $u_{I,m}$, a spatial eigenfunction of Schrödinger equation. The expectation value of the x-component of magnetic moment with the wavefunction [2.21] is

$$\langle \mu_x(t) \rangle = \int \Psi^*(t)\mu_x\Psi(t)dv. \qquad [2.22]$$

Using $\mu_x = \Upsilon\hbar I_x$ and Eq. [2.21]

$$\langle \mu_x(t) \rangle = \sum_{m,m'} \Upsilon\hbar c^*_{m'} c_m \langle m'|I_x|m\rangle e^{(i/\hbar)(E_{m'}-E_m)t} \qquad [2.23]$$

For a spin ½ system, I=1/2 and m = $\pm$ ½ and considering $c_{1/2} = ae^{i\alpha}$ and $c_{-1/2} = be^{i\beta}$, the expectation values of x-, y-, and z-components of magnetic moments are as follows:

$$\begin{aligned} \langle \mu_x(t) \rangle &= \Upsilon\hbar abcos(\alpha - \beta + \omega_o t) \\ \langle \mu_y(t) \rangle &= -\Upsilon\hbar absin(\alpha - \beta + \omega_o t) \\ \langle \mu_z(t) \rangle &= \Upsilon\hbar(a^2 - b^2)/2 \end{aligned} \qquad [2.24]$$

From these equations one can clearly see that the expectation value of μ_x and μ_y oscillates in time with Larmor frequency and the same amplitude, while the expectation value of μ_z is independent of time.

In quantum mechanics, the equation of motion for any operator F can be expressed in commutation notation as

$$\frac{dF}{dt} = \frac{i}{\hbar}\,[\mathcal{H}, F], \qquad [2.25]$$

where $\mathcal{H}$ is Hamiltonian of the system. For the external magnetic field B_0 along z direction, the Hamiltonian of the spin I is

$$\mathcal{H} = \gamma\hbar B_0 \mathrm{I_z} \qquad [2.26]$$

The equation of motion for the x-, y-, z- components of spin I system would then be

$$\frac{dI_x}{dt} = \frac{i}{\hbar}\,[\mathcal{H}, I_x] = \gamma B_0 I_y$$

$$\frac{dI_y}{dt} = \frac{i}{\hbar}\,\left[\mathcal{H}, I_y\right] = -\gamma B_0 I_x \qquad [2.27]$$

$$\frac{dI_z}{dt} = \frac{i}{\hbar}\,[\mathcal{H}, I_z] = 0$$

In vector notation these equations become

$$\frac{d\vec{I}}{dt} = I \times \gamma\overrightarrow{B_0}. \qquad [2.28]$$

Using $\mu = \gamma\hbar I$, Eq. [2.28] becomes

$$\frac{d\vec{\mu}}{dt} = \gamma\vec{\mu} \times \vec{B}_0\,, \qquad [2.29]$$

which is just the classical Eq. [2.12]. So, the expectation value of magnetic moment follows the classical equation of motion. Thus, considering ensemble of noninteracting spins, the classical equation is sufficient to describe the dynamics of the bulk magnetization.

2.1.4 Effect of Radio Frequency (RF) Field

In presence of oscillating magnetic field $\vec{B}_1(t)$ and in a rotating frame of reference which is rotating at frequency ω about z axis, equation of motion [2.29] becomes

$$\frac{\delta\vec{\mu}}{\delta t} = \gamma\,\vec{\mu} \times [(B_0 - \frac{\omega}{\gamma})\hat{z} + B_1\hat{x}\,] = \gamma\vec{\mu} \times \vec{B}_{eff}\,, \qquad [2.30]$$

where

$$\vec{B}_{eff} = (B_0 - \frac{\omega}{\gamma})\hat{z} + B_1\hat{x}. \qquad [2.31]$$

2.1.5 Free Induction Decay (FID)

Following an RF pulse that perturbs the equilibrium magnetization (longitudinal magnetization), the signal (transverse magnetization) decays with a characteristic time constant called spin-spin relaxation time (T_2). The signal equation of an FID that is originated due to the application of the RF pulse of flip angle θ is

$$S(t) = \sin(\theta)\int_{-\infty}^{\infty}\rho(w)e^{-i\omega t}e^{-t/T_2(\omega)}d\omega \qquad [2.32]$$

where $\rho(w)$ is the spectral density function and t is the time following the RF excitation. In an actual fact, the FID signal decays with a much faster decay constant called T_2^* decay time if there is local field inhomogeneity, in addition to microscopic spin-spin interactions. The dephasing caused by field inhomogeneities is reversible, while that caused by microscopic interaction is irreversible. The FID will be discussed in more detail in section 2.2.4.

2.1.6 T_1, T_2, and T_2^* Relaxation Times

When an external magnetic field is applied to a spin system, the spins are partially polarized. The excess spins in the direction of the applied field constitutes a net magnetization called thermal equilibrium magnetization. In order to observe the NMR signal, an RF pulse is applied to the sample to create the magnetization in the transverse plane. The term "relaxation" is associated with the different physical processes by which the magnetization in a nonequilibrium state returns back to the equilibrium state when the exciting RF pulse is switched off.

Longitudinal or spin lattice relaxation (T_1) is the process by which the excited magnetization recovers its thermal equilibrium state by releasing the excess energy to the surrounding lattice. Due to natural motion such as vibration, rotation, and translation caused by thermal fluctuation of molecules, the fluctuating magnetic field is created in the nucleus. This field is mainly caused by the intermolecular dipole-dipole interaction in biological water (17). The interaction between the resonating spin and the fluctuating magnetic field induces T_1 relaxation.

Spin-spin relaxation time (T_2) is the measure of the loss of the phase coherence of the transverse magnetization in a perfectly uniform external magnetic field. The T_2 relaxation does not involve the transfer of energy between the lattice and spin system; rather it is associated with magnetization exchange due to spin diffusion in microscopic magnetic field inhomogeneity caused mainly by the dipolar interaction between the spins.

In an actual NMR experiment, the transverse magnetization dephases much faster than that caused by T_2 relaxation due to magnetic field inhomogeneity. The inhomogeneity may arise from two sources: one from an imperfect main magnetic field

and the other from susceptibility effects produced by tissue such as air tissue interface (lungs or intestines or sinuses), tissue bone interface (spinal cord) etc., or other materials placed inside the main magnetic field. This dephasing time, which is the combination of transverse relaxation and magnetic field inhomogeneity, is called apparent transverse relaxation time (T_2^*). T_2^* is always less than or equal to T_2. Mathematically, the relation between T_2 and T_2^* can be written as

$$\frac{1}{T_2^*} = \frac{1}{T_2} + \gamma \Delta B_0, \qquad [2.33]$$

where $\gamma \Delta B_0$ is field inhomogeneity.

2.1.7 Bloch Equation

The Bloch equation is the phenomenological equation introduced by Felix Bloch in 1946 (18) that gives the time evolution of nuclear magnetization in the presence of T_1 and T_2 relaxation times.

$$\frac{d\vec{M}}{dt} = \gamma \vec{M} \times \vec{B} + \frac{(M_z^o(t) - M_z(t))}{T_1} \hat{z} - \frac{M_x(t)\hat{x} + M_y(t)\hat{y}}{T_2} \qquad [2.34]$$

where $\vec{B}$ is total magnetic field which is the sum of static field $\vec{B}_0$ and oscillating field $\vec{B}_1$, $M_z^o(t)$ is the thermal equilibrium magnetization, and M_x and M_y are the transverse components of magnetization. In component form, Equation [2.34] can be written as:

$$\frac{dM_x}{dt} = \gamma(\vec{M} \times \vec{B})_x - \frac{M_x(t)}{T_2}$$

$$\frac{dM_y}{dt} = \gamma(\vec{M} \times \vec{B})_y - \frac{M_y(t)}{T_2} \qquad [2.35]$$

$$\frac{dM_z}{dt} = \gamma(\vec{M} \times \vec{B})_z + \frac{(M_z^o(t) - M_z(t))}{T_1}$$

2.2 Theory of Magnetic Resonance Imaging

Magnetic resonance imaging (MRI) is a noninvasive imaging technique based on the principles of nuclear magnetic resonance (NMR) and used mainly in the medical field to produce images of the organs of interest in the human body. Paul Lauterbur in 1972 first demonstrated the MR image of a small test tube sample from NMR signal using a gradient field (magnetic field that varies the strength of main magnetic field from one end of sample to the other) to uniquely encode the spatial information into the NMR signal. In order not to scare people with the term "nuclear," the term MRI was used rather than nuclear magnetic resonance imaging (NMRI) in the late 1970s. Since then, both software and hardware have rapidly advanced for various applications, such as MR angiography, functional imaging, perfusion MRI, diffusion MRI, and MR spectroscopy, etc. In this section we discuss signal collection, imaging gradients, and hardware.

2.2.1 Signal Collection

In the previous section we discussed how bulk magnetization precessing at the Larmor frequency on the transverse plane can be generated by placing an object in an external magnetic field $\vec{B}_0$ and stimulating it with an RF field $\vec{B}_1(t)$. An MR signal is detected by using an RF coil tuned to Larmor frequency according to Faraday's law of electromagnetic induction, which states that an electromagnetic force (emf) induced by a time-varying magnetic field on a closed-loop coil is equal to the rate of change of magnetic flux. According to the classical theory of electrodynamics, current density produced by time varying magnetization (19) is given by

$$\vec{J} = \nabla \times \vec{M}. \qquad [2.36]$$

The magnetic flux linked through the RF coil is

$$\phi_r(t) = \int \vec{B}(\vec{r},t).d\vec{S} = \oint \overrightarrow{A}.d\vec{r} \quad [2.37]$$

$$= \oint \frac{\mu_o}{4\pi} \int \frac{\vec{J}(\vec{r}',t)}{|\vec{r}-\vec{r}'|} d^3\vec{r}'.\, d\vec{r} = \oint \frac{\mu_o}{4\pi} \int \frac{\nabla_{\vec{r}'} \times \vec{M}\ (\vec{r}',t)}{|\vec{r}-\vec{r}'|} d^3\vec{r}'.\, d\vec{r}\ . \quad [2.38]$$

Solving Eq. [2.38] using the identity $\nabla\ \times a\vec{v} = (\nabla a)\ \times \vec{v} + a\nabla\ \times \vec{v}$, we get

$$\phi_r(t) = \int \vec{M}(\vec{r}',t).\vec{B}(\vec{r}')d^3\vec{r}', \quad [2.39]$$

where

$$\vec{B}(\vec{r}') = \frac{\mu_o}{4\pi} \oint \frac{d\vec{r} \times (\vec{r}-\vec{r}')}{|\vec{r}-\vec{r}'|^3} \quad [2.40]$$

is the magnetic field created at point $\vec{r}'$ by a unit steady current in the coil. The emf induced in the coil due to this flux is:

$$\varepsilon(t) = -\frac{d\phi_r(t)}{dt}$$

$$= -\frac{d}{dt} \int [M_x(\vec{r}',t)B'_x(\vec{r}') + M_y(\vec{r}',t)B'_y(\vec{r}') + M_z(\vec{r}',t)B'_z(\vec{r}')]\, d^3\vec{r}'. \quad [2.41]$$

The term $M_z(\vec{r}',t)$ in Eq. [2.41] varies very slowly due to the long T_1 relaxation time compared to the x-, y- terms, so it can be dropped.

$$\varepsilon(t) = -\int [\frac{dM_x(\vec{r}',t)}{dt} B'_x(\vec{r}') + \frac{dM_y(\vec{r}',t)}{dt} B'_y(\vec{r}')]\, d^3\vec{r}'. \quad [2.42]$$

Using $M_{xy}(\vec{r}',t) = M_{xy}(\vec{r}',0)e^{-i\omega_o t}$ obtained by solving the Bloch equation discussed in the previous section 2.1.6 and $B'_{xy}(\vec{r}') = B'_x(\vec{r}') + iB'_y(\vec{r}')$, called coil sensitivity, Eq. [2.42] becomes

$$\varepsilon(t) = -i\omega_o \int M_{xy}(\vec{r}',0)e^{-i\omega_o t} B'_{xy}(\vec{r}')d^3\vec{r}'. \quad [2.43]$$

Since the high frequency signal in Eq. [2.43] with the transverse magnetization precessing at Larmor frequency can be problematic for electronic circuits, a phase sensitive detection (PSD) technique is used to move the signal to a low frequency band

by mixing it with a reference sinusoidal signal and using a low pass filter to remove the high frequency component

$$\varepsilon(t) \approx \omega_o \int M_{xy}(\vec{r}', 0) e^{-i\Delta\omega t} B'_{xy}(\vec{r}') d^3\vec{r}', \quad [2.44]$$

where $\Delta\omega = \omega - \omega_o$.

2.2.2 Field Gradients

The spatial information needed for imaging of an object is accomplished by superimposing the gradient fields that linearly vary the static magnetic field on top of the strong static field. The MRI scanner consists of three independent gradient coils to produce gradient fields along x-, y-, and z-directions. These gradients have identical properties but are applied at different moments. In MRI in general, a slice selective gradient is applied to select the anatomical volume of interest (VOI). Within this VOI, a phase encoding gradient is applied to encode the spatial information along the vertical direction and frequency encoding gradient to encode the spatial information along the horizontal direction. Mathematically the magnetic field gradient is written as:

$$\vec{G} = \frac{dB_z}{dx}\hat{x} + \frac{dB_z}{dy}\hat{y} + \frac{dB_z}{dz}\hat{z}. \quad [2.45]$$

The total magnetic field in the presence of a gradient field can be expressed as:

$$\vec{B} = \vec{B}_0 + (\vec{G}.\vec{r})\hat{z}. \quad [2.46]$$

2.2.2.1 Slice Selective Gradient

The first step of spatial encoding is the selection of the slice plane. The selection of a slice is achieved by simultaneously applying the RF pulse together with a gradient field along the slice selection direction (G_{ss}) as shown in Figure 2.3 (a). The slice

selection gradient linearly varies the magnetic field along the slice selection direction, thereby creating the position-dependent frequencies on the spins. The simultaneously applied RF pulse of a certain bandwidth excites the spins of that band.

Mathematically, the Larmor frequency of the spin at position z from the magnet's isocenter in the presence of the slice selection gradient is

$$f = \frac{\gamma}{2\pi}(\vec{B}_0 + \vec{G}_{ss}.\vec{z}) \qquad [2.47]$$

The relation between bandwidth (Δf) of RF pulse, gradient strength, and slice thickness can be expressed as

$$\Delta f = \frac{\gamma}{2\pi} G_{ss} \Delta z \ . \qquad [2.48]$$

This equation reflects that increasing the slice selection gradient decreases the slice thickness for a given bandwidth of the RF pulse as shown in Figure 2.3 (b).

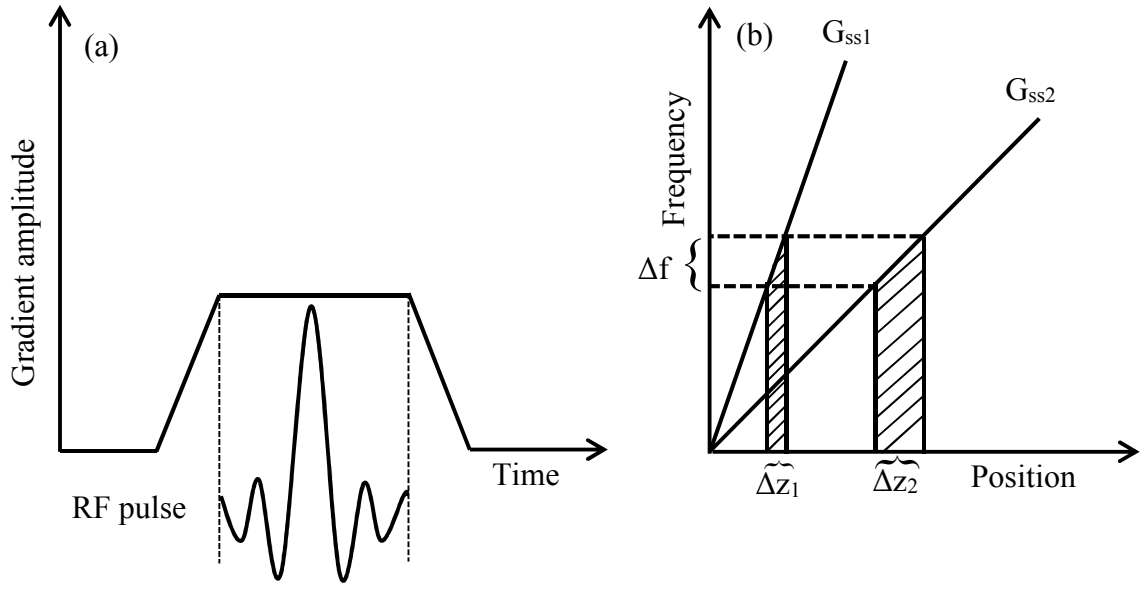

Figure 2.3: Relationship between the slice selection gradient, RF bandwidth, and slice thickness. (a) The slice selection gradient applied concurrently with a RF pulse. (b) Graph of Larmor frequency as a function of position along the slice selection gradient direction. The slope of each line indicates the strength of each gradient. For a fixed bandwidth of the RF pulse, the stronger the gradient, the thinner the slice thickness.

2.2.2.2 Frequency Encoding Gradient

The frequency encoding of the imaging object is obtained by applying the frequency encoding gradient during readout. This gradient assigns a unique precession frequency to each isochromat so that different frequencies are encoded into the time domain signals depending on their positions along the gradient direction. The frequency content in the signal is obtained by inverse Fourier transformation of the time domain signal. Assuming the frequency encoding gradient (G_x) is along the x-direction, the resonant frequency $\omega(x)$ at position x can be expressed as

$$\omega(x) = \omega_o + \gamma G_x x. \quad [2.49]$$

This equation shows that the resonant frequency varies linearly with position x due to G_x. The data acquisition duration (T_{acq}) is determined from receiver bandwidth ($\Delta\nu_r$) and the number of k-space data points (n_x) along the readout direction according to the relation

$$T_{acq} = \frac{n_x}{2\Delta\nu_r} = \Delta t. n_x \,, \quad [2.50]$$

where Δt is sampling time or dwell time. The spacing between k space data points (Δk_x) for a constant readout gradient is given by

$$\Delta k_x = \frac{\gamma G_x \Delta t}{2\pi} = \frac{\gamma G_x T_{acq}}{2\pi n_x} = \frac{1}{FOV_x} \,, \quad [2.51]$$

where FOV_x is readout field of view. Combining Eqs. [2.50] and [2.51], we get

$$G_x = \frac{4\pi\Delta\nu_r}{\gamma FOV_x} \,. \quad [2.52]$$

2.2.2.3 Phase Encoding Gradient

The phase encoding gradient is employed before the frequency encoding and after the slice selection gradients by applying the gradient lobe whose area varies with time to

get the entire k space lines with different amounts of linear phase. The extra phase introduced to the transverse magnetization due to this gradient is

$$\Phi(y) = \gamma y \int_t^{t+T} G_y(t)dt = 2\pi y k_y \,, \qquad [2.53]$$

where T is the gradient duration. The spacing between the k space data points along the phase encoding direction (Δk_y) is related with the difference in the gradient strength (ΔG_y) by the relation

$$\Delta k_y = \frac{\gamma}{2\pi}\Delta G_y T = \frac{1}{FOV_{phase}} \,. \qquad [2.54]$$

2.2.3 Imaging Hardware

An MRI system consists of very complex instruments, and their design and specification vary depending on the type of scanner being used. However, all MRI scanners have several essential common components. A schematic diagram of a MRI scanner is shown in Figure 2.4. An MRI scanner has a main magnet to produce a homogeneous magnetic field B_0 that creates a net magnetization in the subject to be scanned. The main magnet can be one of three types: permanent, superconducting and electromagnet. The spatial encoding in the signal is performed by using three mutually orthogonal gradient coils. The gradient coil is, in general, either Maxwell coil or saddle coil type. The transverse magnetization is obtained by applying the RF pulse to the subject using one or more RF coils.

The RF coil is used to produce the B_1 field that produces transverse magnetization in the sample and receives the NMR signal from the sample. A single RF coil can be used as both a transmitter and a receiver, or separate coils can be used for a transmitter and receiver. Based on geometric shape, RF coils are defined as volume and surface coils. A

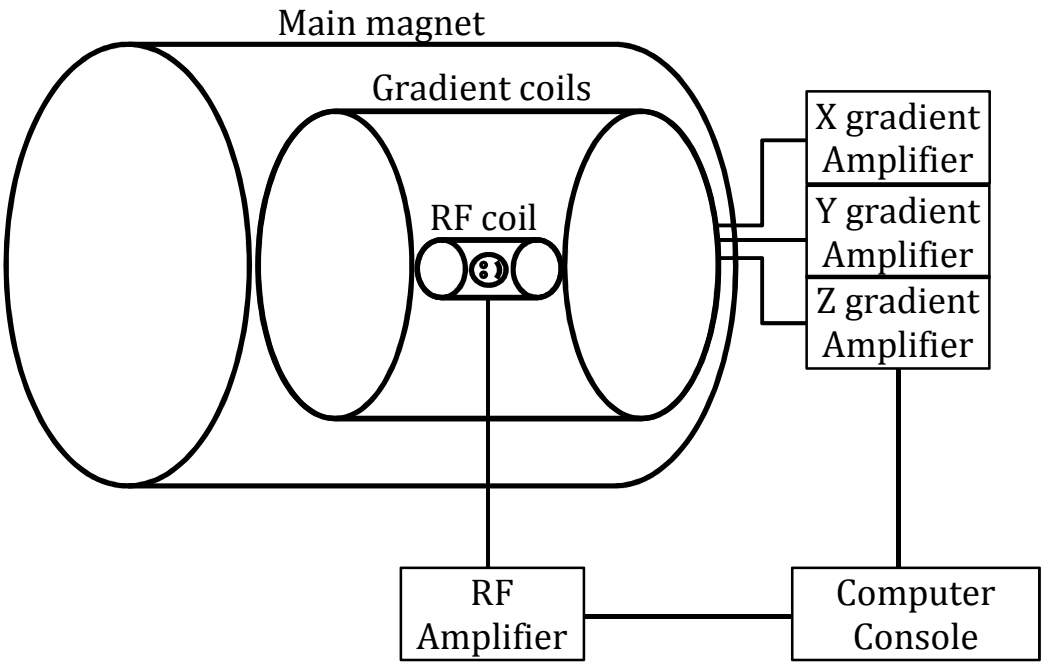

Figure 2.4: Schematic diagram of an MRI scanner. The MRI system mainly consists of a main magnet, gradient coils, gradient amplifiers, RF amplifiers, and computer console.

volume coil, in general, is large and placed around the entire object to produce better B_1 field homogeneity, while a surface coil is relatively small and placed on the surface of the object to get higher sensitivity. Both B_1 field homogeneity and higher sensitivity can be obtained by using a volume coil as a transmitter and a surface coil as a receiver.

2.2.4 Fundamental Pulse Sequences in MRI

A pulse sequence in MRI is a complete time description of a series of events consisting RF pulses, gradient waveforms, and data acquisition. The pulse sequence manipulates the magnetization to produce the signal in MRI. To understand the subtlety of MRI applications, this section introduces the physical basis of the most fundamental MRI pulse sequences, such as free induction decay (FID), gradient echo (GRE), spin

echo (SE), stimulated echo (STE), and echo planner imaging (EPI). The MRI pulse sequence is a vast and complicated subject; this section presents the fundamentals of basic MRI pulse sequences.

2.2.4.1 Free Induction Decay (FID)

An FID is a transient MR signal that decays towards zero with characteristic time constant T_2 once the transverse magnetization is generated following the excitation RF pulse. The pulse sequence diagram is shown in Figure 2.5. When an RF pulse of flip angle ϕ is applied to net magnetization, M precessing around B_0, called longitudinal magnetization, some component of M is tipped into the transverse plane which induces an emf in the coil based on Faraday's law of electromagnetism. The signal is a damped sine wave dephasing with time constant T_2:

$$S(t) = sin\emptyset \int_{-\infty}^{\infty} \rho(\omega) e^{-t/T_2(\omega)} e^{-i\omega t}, \quad [2.55]$$

where $\rho(\omega)$ is the spectral density function that determines the characteristics of an FID signal. For instance the FID of an isochromat oscillating with the Larmor frequency, ω_o, can be written as:

$$S(t) = M_z^0 sin\emptyset e^{-t/T_2} e^{-i\omega_0 t}, \quad [2.56]$$

where M_z^0 is the thermal equilibrium value of bulk magnetization. In Eq. [2.55] or [2.56], the signal decays with time constant T_2; however, in the real world, the signal dephases more rapidly with a time constant T_2^* due to main magnetic field inhomogeneity and/or magnetic susceptibility of tissues given by Eq. [2.33]. So, the FID provides T_2^* weightings to the acquired signal. The dephasing caused by the field inhomogeneity is reversible, as the phase difference can be reversed by using a refocusing pulse (180° RF pulse).

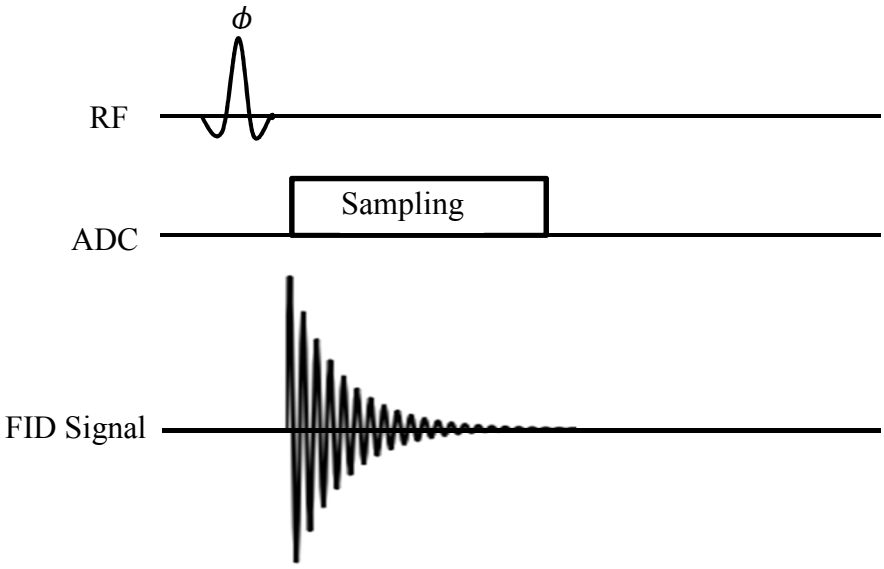

Figure 2.5: Free induction decay pulse sequence diagram.

2.2.4.2 Gradient Echo Imaging Sequence

The gradient echo imaging (GRE) sequence consists of a single RF pulse followed by dephasing and rephasing gradient pulses on the frequency encoded axis to form an echo. A small flip angle excitation is often used in GRE sequence for fast imaging such as in vascular and cardiac imaging. With a flip angle less than 90°, no lengthy time is required for T_1 recovery, so TR (2-50 ms) of GRE sequence is usually short. As a negative x-gradient is turned on, the loss of phase coherence can be expressed as

$$\emptyset(x,t) = -\gamma \int_0^t G_x x dt \ . \qquad [2.57]$$

When a positive gradient of the same strength is applied, the transverse magnetization rephrases, and the peak of the echo is formed when the area under the two gradient lobes is equal. The phase evolution after the second gradient echo can be expressed as

$$\emptyset(x,t) = -\gamma \int_0^t G_x x dt \; + \; \gamma \int_t^{2t} G_x x dt \; . \qquad [2.58]$$

A typical diagram of GRE pulse sequence is shown in Figure 2.6. GRE images are T_2^* weighted rather than T_2 weighted as in spin echo images.

2.2.4.3 Spin Echo Imaging Sequence

Spin echo (SE) sequence is a fundamental pulse sequence in MRI formed by an excitation pulse (90˚) and one or more refocusing pulses (180˚). The formation of a spin echo signal by 90° - τ - 180° excitation scheme is shown in Figure 2.7. A 90° pulse flips the net magnetization into the transverse plane, and the spins precess about the z-axis. Some spins pressess faster than others due to local magnetic field inhomogeneities, thereby losing the phase coherence with time. The 180° pulse flips the spins over to the

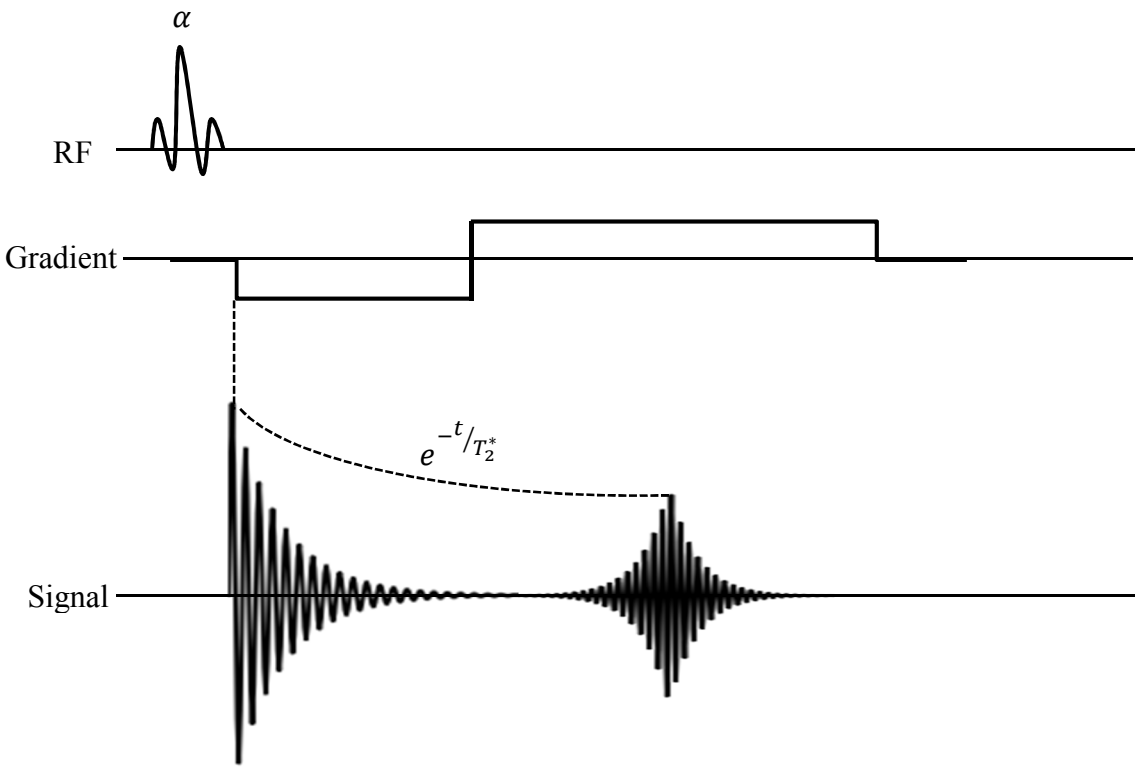

Figure 2.6: Gradient echo pulse sequence diagram.

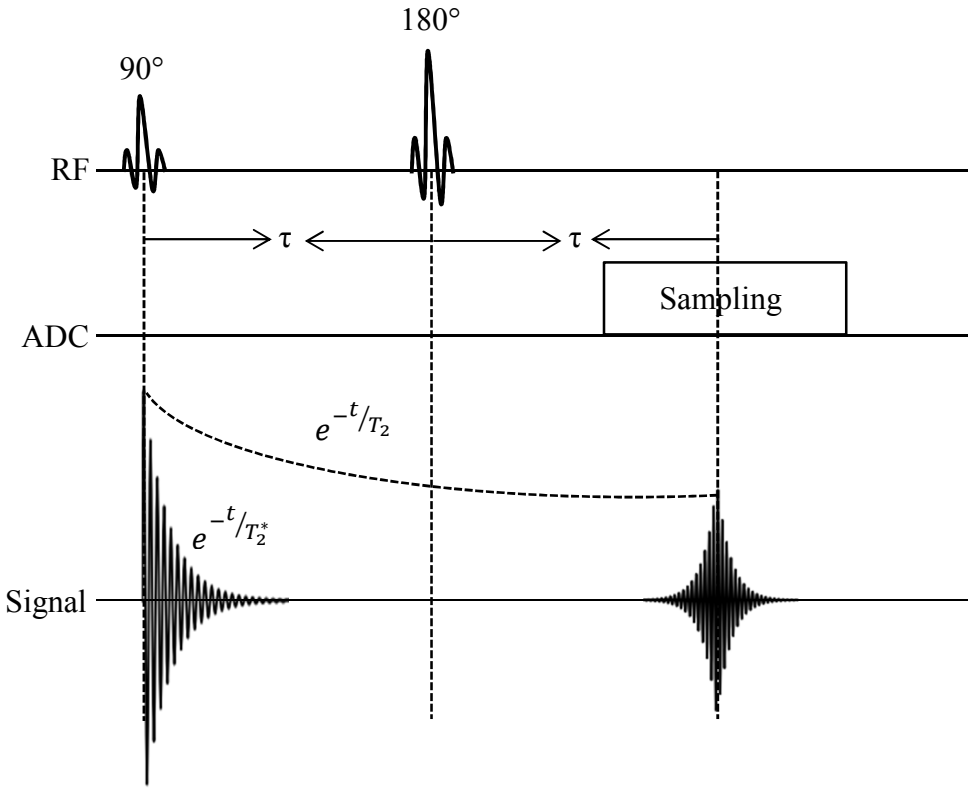

Figure 2.7: Spin echo pulse sequence diagram. Spin echo is formed at time 2τ after the 90° pulse.

other side of the transverse plane, so that slower spins lead the faster ones by the same phase angle with which they were lagging behind prior to the 180° pulse. The fast spins catch up with the slow ones at time τ after the 180° pulse, thus forming a peak of an echo at time 2τ after the 90° pulse. Detailed mathematical description of the formation of SE is given elsewhere (20).

Since the SE sequence refocuses off-resonance effects, SE provides greater immunity to the artifacts resulting from off-resonance effects such as main magnetic field inhomogeneity and susceptibility artifacts, and SE sequence is T_2 weighted.

2.2.4.4 Stimulated Echo (STE) Imaging Sequence

In an STE sequence, at least three RF pulses of flip angles 90° or less are used. There is no selective or nonselective 180° RF pulse as needed for conventional spin-echo imaging sequence. The general pulse sequence scheme is $\alpha - \tau_1 - \beta - \tau_2 - \gamma$. The pulse sequence diagram is shown in Figure 2.8. Three FIDs and five echoes are formed from a three pulse scheme. Among five echoes, three are conventional spin echoes (SEs) formed by each possible pair of RF pulses; one is secondary spin echo, and one is stimulated echo produced by the combined effect of all three RF pulses.

The FID_α generated by the α pulse is refocused by the β pulse to produce spin echo $SE_{\alpha\beta}$ at $t=2\tau_1$and by the γ pulse to produce the spin echo $SE_{\alpha\gamma}$ at $t = 2(\tau_1 + \tau_2)$. The FID_β generated by the β pulse is refocused by the γ pulse resulting in the spin echo $SE_{\beta\gamma}$ at $t = \tau_1 + 2\tau_2$. The spin echo $SE_{\alpha\beta}$ is refocused by the γ pulse to produce the spin echo $SE_{\alpha\beta\gamma}$ at $t = 2\tau_1 + \tau_2$. Finally, the stimulated echo $STE_{\alpha\beta\gamma}$ is produced at $t = 2\tau_2$ when a part of transverse magnetization flipped by α pulse is stored in the longitudinal direction by the β pulse and flipped back to the transverse plane by the γ pulse. The STE magnetization suffers T_1 decay during time τ_2 in the longitudinal plane, and T_2 decay in the transverse plane during time $2\tau_1$ between α and β pulses, and between γ pulse and the center of the stimulated echo. During the time τ_2, the phase accumulated during time τ_1 when it was in transverse plane was retained in the magnetization. This is called phase memory.

The amplitude of all echoes and their echo times obtained from the stimulated echo pulse sequence are detailed in Table 2.2 (20). From this table it can be seen that the maximum stimulated signal can be obtained when $\alpha = \beta = \gamma = 90°$.

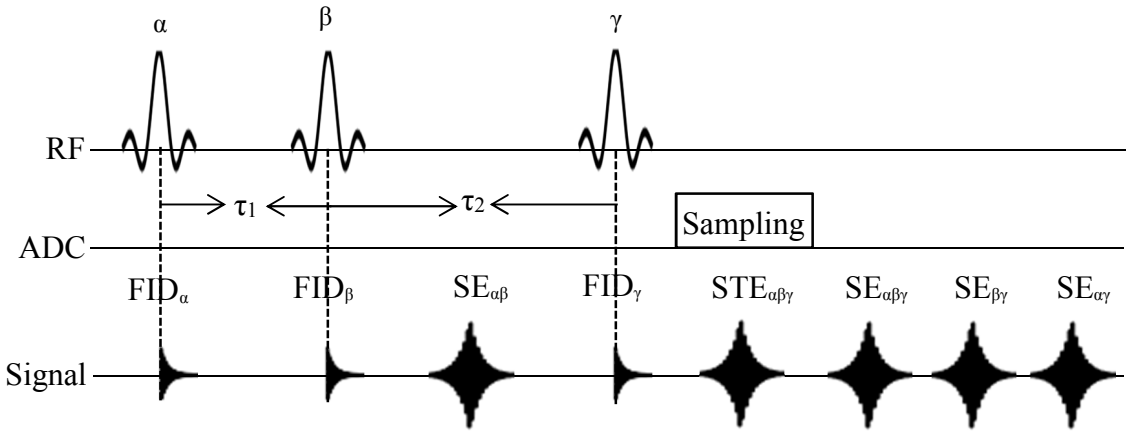

Figure 2.8: Stimulated echo pulse sequence diagram with a train of three RF pulses producing five echoes and three FIDs.

Table 2.2: The amplitude and echo times of 5 echoes formed by a three pulse sequence.

Echo	Echo time	Echo amplitude
$SE_{\alpha\beta}$	$2\tau_1$	$M_z^0 sin\alpha sin^2(\beta/2)e^{-2\tau_1/T_2}$
$STE_{\alpha\beta\gamma}$	$2\tau_1 + \tau_2$	$\frac{1}{2}M_z^0 sin\alpha \sin\beta \sin\gamma e^{-\tau_2/T_1} e^{-2\tau_1/T_2}$
$SE_{\alpha\beta\gamma}$	$2\tau_2$	$-M_z^0 sin\alpha sin^2(\beta/2) sin^2(\gamma/3) e^{-2\tau_1/T_2}$
$SE_{\beta\gamma}$	$\tau_1 + 2\tau_2$	$M_z^0[1-(1-cos\alpha)e^{-\tau_1/T_1}] sin\beta sin^2(\gamma/3) e^{-(\tau_1+2\tau_2)/T_2}$
$SE_{\alpha\gamma}$	$2(\tau_1 + \tau_2)$	$M_z^0 \, sin\alpha cos^2(\beta/2) sin^2(\gamma/3) \, e^{-2(\tau_1+\tau_2)/T_2}$

2.2.4.5 Echo Planar Imaging (EPI) Sequence

In EPI multiple lines of imaging data are acquired after a single RF excitation by repetitively switching the frequency and phase encoding gradients, forming a train of gradient echoes in contrast to the conventional imaging sequence where one line of imaging data is collected within each TR period. Each oscillation of the frequency encoding gradient corresponds to one line of k space, and that of phase encoding gradient corresponds to a transition from one line to the next in k-space. EPI can be performed using single or multiple excitation pulses (shots) and can be gradient or spin echo based.

A single shot gradient based EPI, as shown in Figure 2.9, is the fastest pulse sequence primarily used in real time cardiac, diffusion, perfusion and BOLD (blood oxygen level dependent) imaging (21). Several artifacts such as Nyquist ghost artifact, chemical shift artifact, susceptibility artifact, and image blurring arise in EPI.

2.3 Transmit/Receive (T/R) Switch and RF Coil

In order to get the MR signal from the sample in an NMR/MRI experiment, first it is excited by the RF pulse and then MR signal from the sample is obtained after turning off the RF pulse. Depending on many factors, such as the size of the RF coil, the value of specific absorption rate (SAR), the part of anatomy to be scanned etc., a wide range of very high power RF pulses, typically few kilowatts, are applied for short durations during RF transmission, while a very feeble NMR signal of a few millivolts is received during

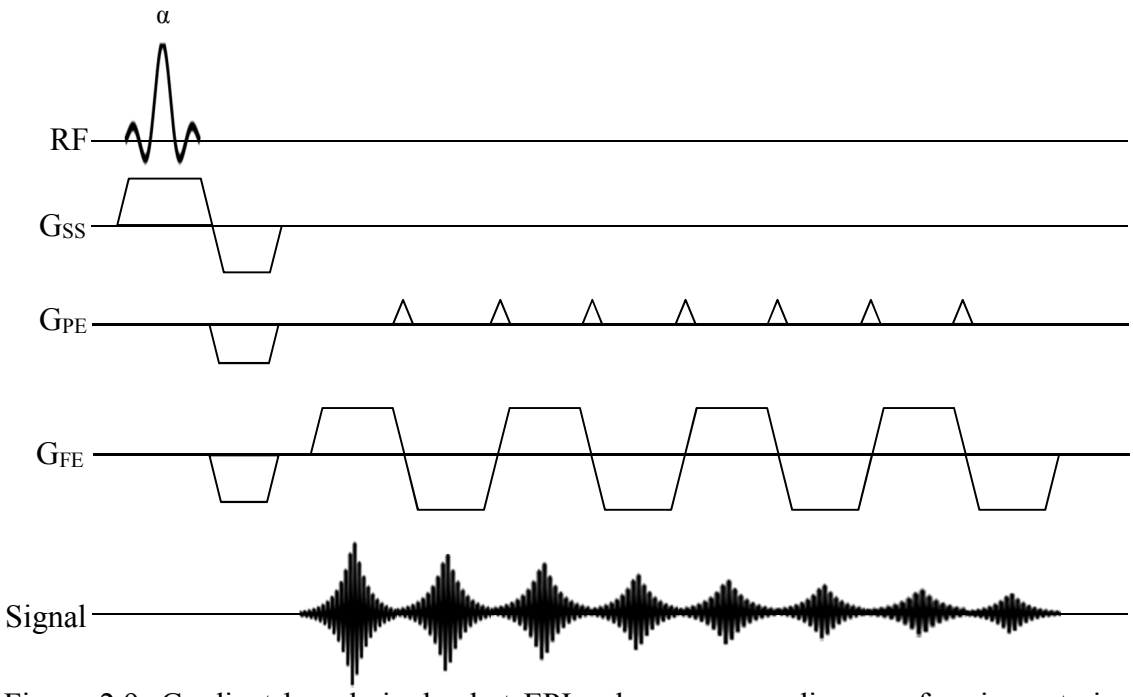

Figure 2.9: Gradient based single shot EPI pulse sequence diagram, forming a train of gradient echoes.

signal reception. A preamplifier is needed to boost the strength of the signal without considerably degrading the signal to noise ratio (SNR). The preamplifier is so delicate that the RF pulse can easily destroy it, so it is imperative to protect the preamplifier from high input power during transmission of the RF pulses by isolating the receive path from the transmit power during the time the RF pulse is transmitted to the RF coil.

Several strategies have been employed to isolate the preamplifier from transmit power. In the case of the receive-only RF coil (usually body coil is used as a transmit coil and the local coil for receive), the preamplifier is isolated from the transmit power by using an active and a passive trap in the coil. An active trap is an LC parallel circuit with PIN diode driven by PIN current, and a passive trap is that with crossed switching diodes activated by the transmit RF field in case the active trap fails. However, for the transmit-receive RF coil, which is used both in transmit and receive modes, the most widely adopted strategy is the use of a transmit/receive (T/R) switch.

The block diagram of the T/R switch is shown in Figure 2.10. The T/R switch, hardware interface between transmitter/preamplifier and the RF coil, connects the transmit and receive paths to the shared RF coil during the RF transmission and the signal reception, respectively. Beside switching action, the primary job of the T/R switch is to protect the preamplifier from damage caused by the RF pulse during transmission and to allow the MR signal to be passed undistorted and undiminished, without coupling any noise from the transmitter and with minimal addition of noise resulting in a maximal SNR (22) to the preamplifier via the receive path.

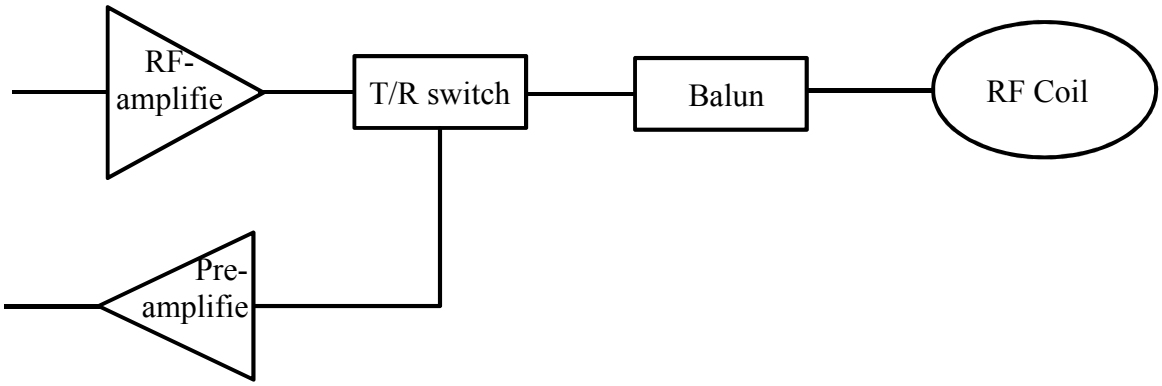

Figure 2.10: Block diagram of a typical transmit-receive RF coil connected with T/R switch.

2.3.1 Linear T/R Switch

The simplest linear T/R switch consists of a pair of crossed PIN diodes on the transmit path and a quarter wave transmission line terminated by a PIN diode on the receive path as shown in Figure 2.11. A PIN diode is a semiconductor device that acts as a variable resistor for the RF signal. When forward biased, either passing direct current (dc) or high power RF pulse during RF transmission, it offers a very low impedance (typically 0.1 Ω) to the RF pulse. When the PIN diode is zero or reverse biased by applying reverse voltage during reception, it acts as an open circuit with a small capacitance (typically 1 pF). The quarter wave transmission line is made by taking the length of the coaxial cable equal to one fourth of the wavelength corresponding to the desired frquency times velocity factor of the coaxial cable and terminating the center conductor of the cable to the ground via PIN diode. The quarter wave transmission line transforms its output impedance (Z_{output}) according to the equation (23):

$$Z_{input} = \frac{Z_0^2}{Z_{output}}. \qquad [2.59]$$

During RF transmission, the crossed diodes at the end of the quarter wave cable

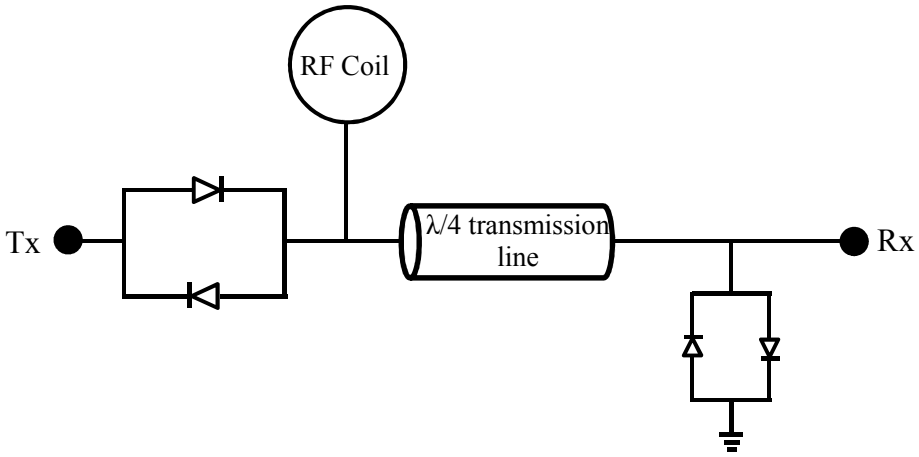

Figure 2.11: Circuit diagram of a simple T/R switch with crossed PIN diodes on transmit path and quarter wave cable on receive side.

are shorted by the RF pulses so that input impedance becomes infininte, acting as if the receive path is entirley disconnected from the RF coil. During reception, the crossed diodes are open so that input impedance is equal to Z_o (50 Ω), thereby allowing the MR signal to be passed undiminished to the preamplifier. A lumped circuit element such as π or Tee network as shown in Figure 2.12 can be used in place of the quarter wave transmission line. The equation for computing L and C values of π or Tee network corresponding to the desired frequency is discussed in Chapter 3. The L and C values for some MR active nuclei at 3T field are detailed in Table 2.3.

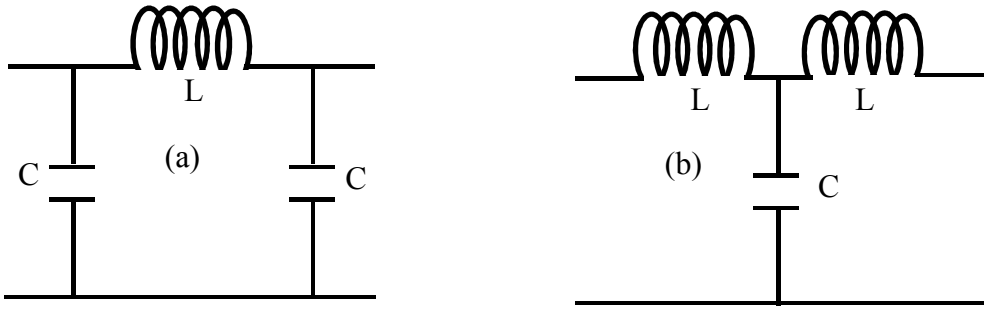

Figure 2.12: Circuit diagram of (a) π (b) Tee networks.

Table 2.3 : L and C values of π or Tee network for selected MR active nuclei at 3T field.

Nuclei	^{1}H	^{31}P	^{19}F	^{23}Na	^{13}C	^{7}Li	^{3}He
f (MHz)	123.24	49.89	115.95	32.60	30.99	47.90	93.93
L (μH)	0.065	0.160	0.069	0.244	0.257	0.166	0.0845
C(pF)	25.8	63.8	27.5	97.6	102.7	66.5	33.9

2.3.2 Quadrature T/R Switch

In NMR/MRI a quadrature RF coil (formed by arranging two RF coils such that their fields are equal in magnitude and differ in phase by 90°) is often used to achieve a low specific absorption rate (SAR) during RF transmission and a high SNR during signal reception. A quadrature coil produces a circularly polarized field, which is twice as efficient as using a linear RF coil (which produces a linearly polarized field) in exciting the nuclear magnetization. This is because both of its rotating components interact with the precessing spins. Also a quadrature coil has a receiving sensitivity improvement by a factor of $\sqrt{2}$ over a linear coil. A quadrature T/R switch is needed in driving the quadrature coil. The simplest quadrature T/R switch can be made by connecting the transmit and receive arms of the linear T/R switch with a quadrature hybrid as shown in Figure 2.13. The quadrature hybrid has four ports. The port “In” is connected to the transmit section of the quadrature T/R switch. The output ports “0°” and “90°,” having a phase difference of 90°, are connected to the quadrature RF coil. The port “Iso” is connected to the receive section of the T/R switch. The isolation property of this port prevents of the leakage of the RF pulse to the preamplifier during transmission. The quadrature hybrid is very symmetrical such that any port can be used as input port. A more complicated quadrature T/R switch circuit design is discussed in detail in section 3.3.2.

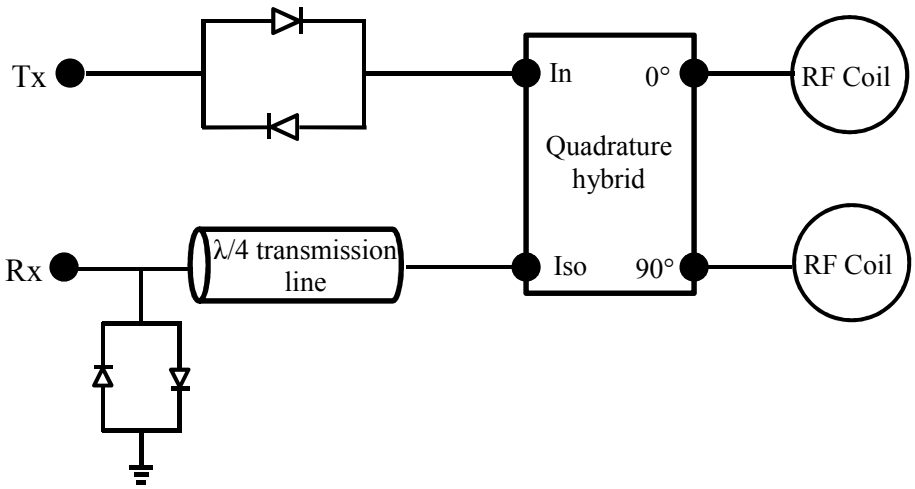

Figure 2.13: Circuit diagram of a quadrature T/R switch with a quadrature hybrid and RF coils. The quadrature hybrid has four ports, namely In, Iso, 0°, and 90° ports.

2.3.3 Quadrature Hybrid

A quadrature coil is composed of two linear RF coils whose fields are out of phase by 90°. In order to drive a quadrature coil, a circuit is needed which splits the transmit power equally into quadrature mode during transmission and combines the two NMR signals from the quadrature RF coil which are 90° out of phase during reception. A quadrature hybrid performs this action. The transmit power from port 1 of the quadrature hybrid shown in Figure 2.14 equally splits into input ports 2 and 3 with phase difference of 90°. The MR signals appearing at ports 2 and 3 during reception from the quadrature coil are out of phase by 90˚. The two quadrature signals from the quadrature RF coil are summed up in phase at port 4 while they are summed up out of phase at port 1, thus cancelling any leakage signal going towards the transmitter (23) during reception. If the quadrature coil is connected incorrectly to the quadrature hybrid, no signal will reach the preamplifier. Swapping the coils connection to the quadrature hybrid helps in retrieving the MR signal.

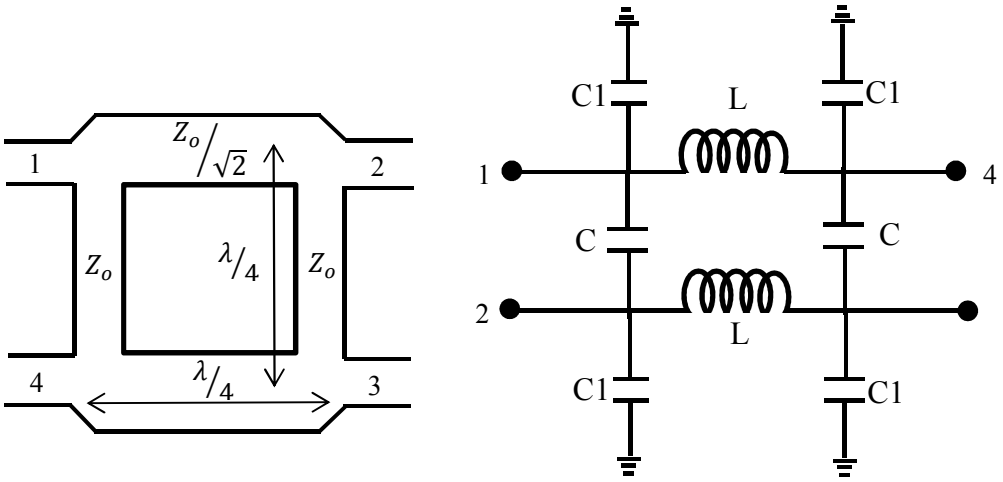

Figure 2.14: Quadrature hybrid's (a) schematic diagram and (b) simple circuit diagram using lumped elements.

2.3.4 Trap Circuit

A trap circuit is a parallel LC circuit that has numerous applications in NMR/MRI devices. In multinuclear MRI/S, a trap tuned to the ^{1}H frequency is placed in a nonproton RF coil to minimize coupling between the two coils. In a receive only RF coil, a trap driven by a PIN diode (active trap) and a trap driven by crossed-switching diodes (passive trap) are used to detune the coil during RF transmission. Most MR scanners have a single transmit port and multiple receive ports. In dual-nuclear experiments in such scanners, two traps tuned to the two desired frequencies are connected suitably prior to two T/R switches so that the ^{1}H RF pulse goes only to the ^{1}H T/R switch and the nonproton RF pulse goes only to the nonproton T/R switch.

The impedance of an LC parallel trap circuit as shown in Figure 2.15 can be written as

$$\frac{1}{Z} = \frac{1}{jX_L} + \frac{j}{X_c}. \qquad [2.60]$$

Solving Eq. [2.60] using $X_L = \omega L$ and $X_C = 1/\omega C$, we get

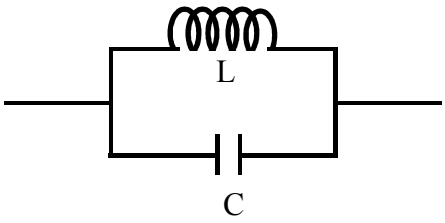

Figure 2.15: Circuit diagram of an LC trap.

$$\boldsymbol{Z} = -\frac{j\omega}{C(\omega^2 - {}^{1}/_{LC})}. \qquad [2.61]$$

Thus at resonance, $\omega = \omega_o = {}^{1}/_{\sqrt{LC}}$ so that the circuit has an infinite impedance at the frequency to which it is tuned. This property is used for detuning the elements in the case of receive-only and multinuclear RF coils. In dual-nuclear experiments this circuit blocks the frequency to which it is tuned while allowing all other frequencies to pass. If the frequency of the other nucleus, ω, is greater than the resonance frequency, ω_o, the circuit is slightly capacitive for ω and an inductor of suitable value may be placed in series with this trap for maximum power delivery. On the other hand, if $\omega < \omega_o$, the circuit will be slightly inductive for ω, so a capacitor would be placed in series with this trap for maximum power delivery. In fact, in dual-nuclear experiments, two trap circuits tuned to two desired frequencies in series with either a capacitor or an inductor connected prior to two T/R switches enable automatic switching between the two frequencies without the need to physically replace the TR switch during the experiment.

2.3.5 RF Coil

The RF coil is an integral part of the MRI system which is used to create a B_1 field that excites spins in a sample and to acquire the MR signal emitted by the resonating

nuclei in the sample. Typically, during transmission, high B_1 field homogeneity for obtaining identical excitation over the entire region of interest is desired, while during reception, high sensitivity for detecting small MR signal rather than B_1 homogeneity becomes very important. Therefore different RF coil geometries are considered to obtain a balance between B_1 homogeneity and coil sensitivity. The various types of RF coils are categorized based on their size, shape, function etc.

Depending on its function, the RF coils are differentiated into three groups: 1) transmit- and receive-only, 2) transmit-only, and 3) receive-only RF. Based on geometrical shape RF coils can be categorized as 1) volume, 2) surface, and 3) phased array.

2.3.5.1 Transmit- and Receive-Only RF Coil

A single RF coil can be used both as a transmitter for producing the B_1 field to excite the spins in the imaging volume and as a receiver to receive the MR signal from this volume. The simplest form of a transmit- and receive-only RF coil is a single loop RF coil placed with its plane lying at a right angle to the direction of B_0 field. Both homogeneity and sensitivity cannot be obtained using a single RF coil for both transmission and reception.

For such a transmit-receive RF coil, it is imperative to protect the preamplifier from the high-power transmit pulse during RF transmission and to avoid the coupling of noise from the RF transmitter into the MR signal during reception. A T/R switch (as discussed in sections 2.3.1 and 2.3.2) is used to switch between these two modes for this purpose.

2.3.5.2 Transmit-Only RF Coil

Separate RF coils can be used for transmission and reception. Either a body RF coil or a volume RF coil that is capable of producing a homogeneous field is used as a transmit-only RF coil.

2.3.5.3 Receive-Only RF Coil

In most MRI/S applications, a volume or body coil is used as a transmit-only coil and a bunch of surface coils are used as receive-only RF coils so that both B_1 field homogeneity during transmission and maximum coil sensitivity during reception can be obtained. A complete circuit diagram of a receive-only coil with interface circuitry is shown in Figure 2.16. The receive-only coil has active and passive traps in order to protect the preamplifier from the high-power RF pulse during transmission. The interface circuitry of a receive-only coil comprises: a balun, a phase shifter, a DC line, and a preamplifier. Details of each circuit are discussed in the following subsections.

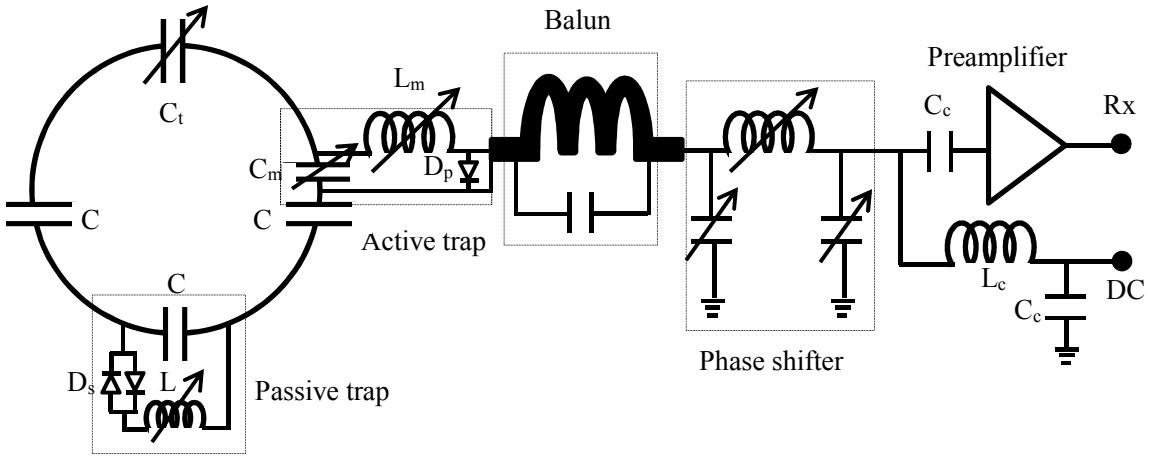

Figure 2.16: A complete circuit diagram of a single loop receive only coil with dedicated receiver circuit consisting of a balun, phase shifter, preamplifier and DC path.

2.3.5.3.1 RF Coil Construction

An RF coil, in general, is constructed by placing equal value capacitors in the coil's conductor break points. It is very important to decide the number of break points for the capacitor. Using too many capacitors in the circuit lowers the quality factor (Q) of the RF coil, while using too few such that the length of conductor is much greater than a tenth of the wavelength corresponding to the tuning frequency reduces the RF coil's efficiency. Likewise, using a thin wire or a narrow copper tape for the coil's conductor increases the resistance of the coil and hence decreases the Q value. The use of thick wire or wide copper tape brings problems such as eddy-current heating, B_1 field inhomogeneity, self-shielding etc. (24). Once the coil is built, it has to be tuned to a desired frequency and matched to a characteristic impedance of the coaxial cable used in order to get the maximum possible SNR from the coil. Tuning and matching the RF coil is performed by adjusting a tuning capacitor C_t, matching capacitor C_m, and matching inductor L_m such that the reflection coefficient S11 of the network analyzer is below -20 dB at the desired frequency as shown in Figure 2.17.

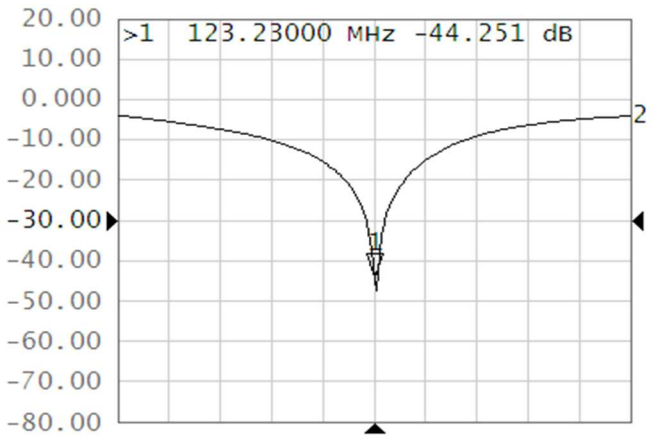

Figure 2.17: Typical S11 curve showing tuning and matching of the RF coil at 123.23 MHz frequency.

2.3.5.3.2 Detuning Circuit

An active/passive detuning circuit is required to detune the receive-only circuit during RF power transmission in order to avoid adverse effects such as damaging the preamplifier, local heating of the patient's body near the coil (i.e., burning the patient), and increasing the B_1 field inhomogeneity. Commonly used active and passive detuning circuits consist of an LC trap circuit as discussed in section 2.3.4 driven by respectively a PIN diode (D_p) and crossed switching diodes (D_s) as shown in Figure 2.16. Both circuits provide ideally infinite impedance when active during RF power transmission. The difference is that forward biasing the PIN diode (by applying 100 mA DC current from MRI system during the transmission) activates the active trap. The crossed-switching diodes of the passive trap are activated by an RF voltage induced in the coil during transmission. In fact, the passive trap is an extra protection for the preamplifier; in case the active trap is broken, the induced current in the coil due to the transmission voltage activates the passive trap. The tuning of the trap circuit is found by looking for a dip in the S11 measurement using a small pick-up coil lightly coupled to the inductor of the trap circuit and adjusting the inductor (stretching or compressing the hand-wound inductor) such that the dip corresponds to the target resonant frequency. The performance of these trap circuits in the RF coil is measured on the bench by looking at the transmission coefficient (S21) in the network analyzer using a set of overlapping decoupled pick-up coils before and after supplying an external DC current to the diodes. The S21 curves before and after the DC current is applied to the diodes are shown in Figure 2.18 (a) and 2.18 (b), respectively. The resonant peak turns into a resonant valley when the DC is applied to the diode. The typical difference in S21 values is at least 30 dB.

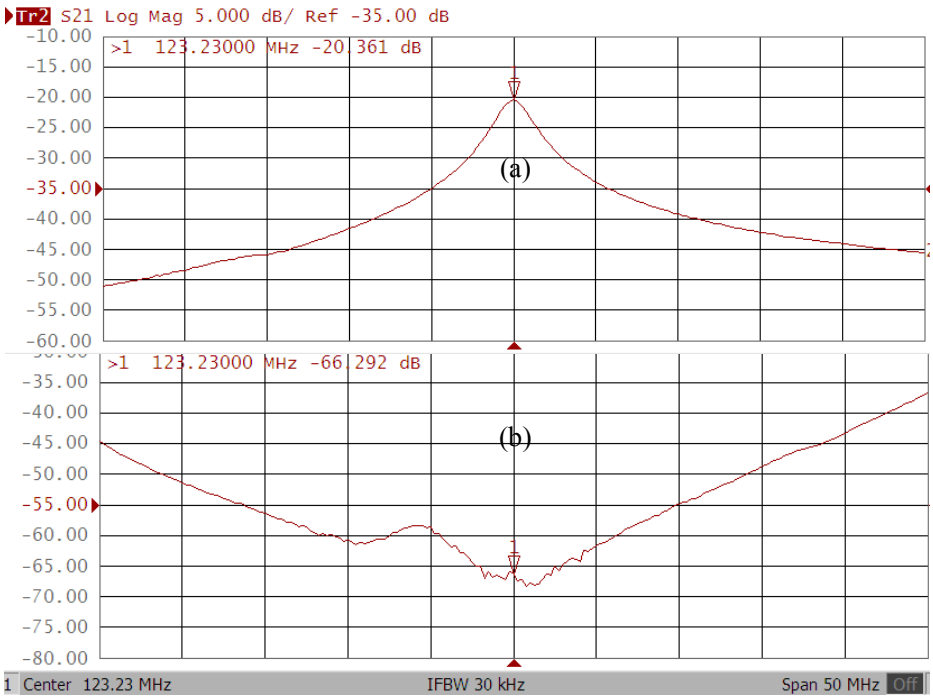

Figure 2.18: S21 curves (a) before and (b) after DC current is applied to the diodes.

2.3.5.3.3 Balun

In a coaxial transmission line, the MRI signal is propagated as a differential-mode current in which equal and opposite currents flow in the two conductors. In addition, there can be a common-mode current which is the in phase current flowing in the same direction in the cable shield. The common mode current can have several deleterious effects in MRI: it modifies the tuning and matching of the coil, it picks up noise from the surroundings, it affects the coupling between the coils in a phased-array or multituned RF coil, it causes image inhomogeneity, it perturbs the differential-mode current, and worst of all it causes the patient burns near the coil. So, it is imperative to suppress the common-mode current without affecting the differential-mode signal. A more efficient and more commonly used technique to suppress the common mode current is to make a cable trap by winding the coaxial cable into a solenoid with a few turns and placing an

appropriate value of capacitor to the shield conductor in parallel as shown in Figure 2.16 so that it is tuned to the resonant frequency of interest.

2.3.5.3.4 Phase Shifter Circuit

In order to use a low-input impedance preamplifier to minimize the coupling between the elemental coils in a phased-array coil, the electrical length of the coaxial cable from the feed point of the RF coil to the phase-shifter circuit shown in Figure 2.16 has to be equivalent to λ/2 (or 180° phase) at the input of preamplifier so that the inductor L_m, capacitor C_m, and the preamplifier forms a parallel resonant circuit that suppresses the current flowing in the RF coil, while it still receives and transfers the MR signal to the preamplifier (25). The capacitor C_m and inductor L_m have to be iteratively adjusted so that they satisfy both 50 Ω matching and preamp decoupling conditions. The necessary steps for adjusting a π-network (two variable capacitors (typically 3-36 pF) and a variable inductor) phase shifter circuit to provide the electrical length of the cable plus phase shifter equivalent to λ/2 cable are:

1) Tune the balun of the feed board (contains baluns, phase shifter, preamplifier, and DC path) to the desired frequency.

2) Calibrate port 1 of a network analyzer by opening the Smith chart of the analyzer.

3) Hook up cable which has length equal to the length of the coaxial cable of the RF coil between port 1 and the coil side of the preamp board.

4) With the input port of the preamplifier in the feed board open, adjust one of the capacitors to set the marker at the resonant frequency in the smith chart to the open

position.

5) With input of the preamplifier port shorted to ground, dial the other capacitor to set the marker to the short position in the smith chart.

6) By connecting the input of the preamp port and ground with 50 ohms, dial the variable inductor to bring the marker to the 50-ohm position in the smith chart.

2.3.5.3.5 Preamplifier

As discussed in section 2.1.2, MRI is the least sensitive technique and the MR signal is on the order of mV. Noise is being continuously added as it passes along the receive pathway to the receiver thereby deteriorating the SNR and obscuring the weak MR signal. Preamplifiers are used to boost the MR signal. The low input impedance preamplifier (having input impedance ~ 1 Ω) is used with a receive-only phased array RF coil to decouple the array elements while amplifying the MR signal. In addition to amplifying the MR signal and associated noise, the preamplifier also adds extra noise into the signal which is characterized by its noise figure (NF) and can be expressed as (26):

$$NF = 10\log\left(\frac{S_i/N_i}{S_o/N_o}\right) = 10\log\left(\frac{S_i/N_i}{GS_i/(N_p+GN_i}\right) = 10\log\left(\frac{N_p+GN_i}{GN_i}\right). \quad [2.62]$$

where G is the gain of the preamplifier. Np and N_i are respectively the noise added by the preamplifier and the noise level at its input. Thus, from Eq. [2.62] it is seen that the preamplifier degrades the SNR as the signal passes through the preamplifier. So, a low noise figure is desired for the minimum noise added by the preamplifier.

2.3.5.3.6 DC Path

DC is sent to the feed board via the choke inductor, Lc (33 μH) as shown in Figure 2.16. In order to absorb any noise associated the DC, a shunt capacitor, Cc (15000 pF) to the ground is connected before the choke inductor. In order to not let the DC enter into the preamplifier, another capacitor, Cc is inserted at the input of the preamplifier. The DC then goes to the active trap circuit and to the ground via the phase shifter and balun.

2.3.5.4 Volume RF Coil

A volume coil is placed around the entire sample being imaged and produces a homogeneous magnetic field throughout the sample volume so that the coil has a large field of view (FOV) as required for imaging larger objects. Using the volume coil as a receiver has two disadvantages: 1) since the sensitive volume of the volume coil is much greater than the region of interest, the coil also collects noise from the entire sample there by degrading the SNR and 2) it does not offer spatial selectivity. For these reasons, the volume coil, in general, is used for the transmission of the RF pulse. Commonly used volume coils in NMR/MRI are the solenoidal coil, birdcage coil, Helmholtz coil, saddle coil, and Alderman-Grant coil (23).

2.3.5.5 Surface RF Coil

The surface coil, as its name suggests, is placed around the surface of the object being imaged. A simple single-loop surface coil is shown in Figure 2.19. The surface coil usually is smaller and offers higher sensitivity and spatial selectivity for superficial

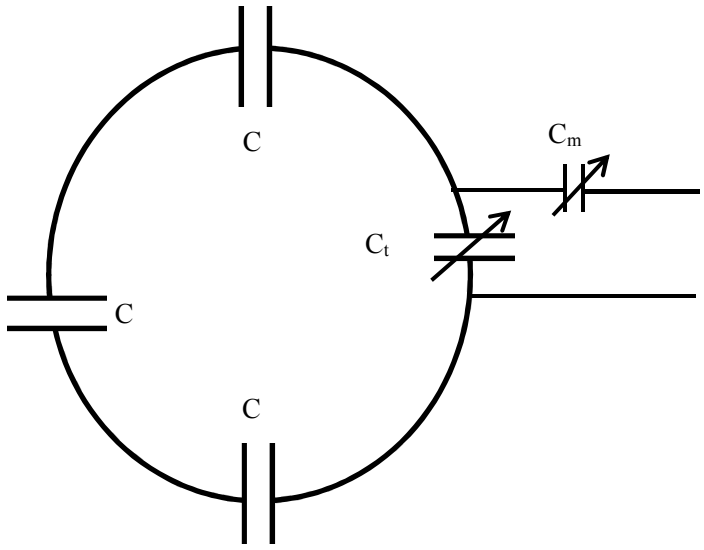

Figure 2.19: A schematic of a single loop circular surface coil with 4 equally spaced tuning capacitors and capacitive matching.

tissue. The coil not only sees the sample at the superficial region but it also collects noise only from this limited region, the result is that the SNR of the surface coil is higher than that of the volume coil at superficial tissue, while the volume coil delivers higher SNR than the surface coil deep inside the sample volume. In order to get both maximum SNR near the surface of the imaging object and uniform excitation, the volume coil is used during transmission and the surface coil is used during reception.

2.3.5.5.1 Calculation of SNR of the Surface Coil

The signal induced in the RF coil due to nuclear spins precessing at frequency ω in a sample of volume V_s is given by (27)

$$Signal \propto V_s \omega^2 B_{1xy}, \quad [2.63]$$

where B_{1xy} is the transverse component of the rotating magnetization produced in the

sample per unit DC current in the RF coil.

The noise in MRI can be calculated using the fluctuation dissipation theorem which says noise originates from the thermally activated random fluctuation generated by a dissipative medium (28). There are two major sources of noise in MRI: i) the coil resistance, r_{coil}, due to the skin effect which depends on frequency and ii) sample resistance, r_{sample}, due to magnetic and dielectric losses. The RMS noise voltage due to these resistances is given by:

$$V_n = \sqrt{4KT\Delta f(r_{coil} + r_{sample})}\,, \qquad [2.64]$$

where K is Boltzmann's constant (1.38 X 10^{-23} J/K), T is the effective temperature of the sample and coil in Kelvin, and Δf is the sampling bandwidth in Hz.

Using a conductor of bigger cross section and smaller resistivity to build the RF coil can decrease the coil losses. The magnetic losses, caused by magnetically induced eddy currents on the sample due to RF field, are unavoidable while dielectric losses, caused by currents on the sample by the electric field of the RF field, can be mitigated by equally distributing the tuning capacitors around the RF coil (29). The SNR of the coil is therefore (30)

$$SNR \propto \frac{V_s\omega^2 B_{1xy}}{\sqrt{r_{coil} + r_{sample}}}. \qquad [2.65]$$

2.3.5.5.2 Quality Factor

Quality factor of an RF coil is a measure of energy storage efficiency of the circuit. Mathematically, it is given by the relation (23)

$$Q = \frac{2\pi(Maximum\ energy\ stored)}{average\ energy\ disspated\ per\ cycle}\,. \qquad [2.66]$$

Q of the RF coil on the bench is measured by measuring the resonant frequency, ω of the coil and the bandwidth, Δω that exists between the -3dB points of the response of the circuit:

$$Q = \frac{\omega}{\Delta\omega}. \quad [2.67]$$

It can also be estimated from the coil's inductance and resistance according to the relation (31):

$$Q = \frac{L\omega}{r}. \quad [2.68]$$

The idea of Q factor for loaded and unloaded RF coils is to estimate the coil's sensitivity. Mathematically, the sensitivity of the surface coil can be expressed as:

$$Sensitivity = \frac{Q_{unloaded}}{Q_{loaded}} = \frac{R_{coil} + R_{sample}}{R_{coil}}. \quad [2.69]$$

For the coil to see the sample effectively, the sensitivity has to be greater than or equal to 5.

2.3.5.6 Phased-Array Coil

A single circular surface RF coil is effectively sensitive to a region whose dimensions are comparable to the diameter of the RF coil (32) and thus has a small field of view (FOV). A single surface RF coil is used for better signal reception at the surface of an organ of interest close to the coil. In most MR applications, a single surface RF coil does not acquire the signal from the whole anatomy of interest. An RF coil with bigger FOV is required to cover the entire anatomy of interest. The limited FOV of a single surface RF coil can be dramatically enhanced without loss of sensitivity by using an assembly of multiple decoupled surface RF coils, called a phased-array RF coil. Besides having high SNR over a large FOV, each elemental RF coil of a phased-array RF coil

acquires its image independently and simultaneously; these can be combined into a single image through postprocessing image-reconstruction techniques. The fact that each RF coil in the array has to be connected to its own preamplifier makes this kind of RF coil very expensive.

In order to get an optimal SNR from a phased-array coil, it is necessary to make the noise from coil to coil uncorrelated. This can be achieved by making the electromagnetic interaction between the coils minimal. A common way to decouple adjacent coils of the array is to arrange them so that they overlap in an optimal pattern. The optimal pattern that forces the mutual coupling to zero depends on the geometry of the RF coil. The interaction between the distant coils of the array can be minimized through preamplifier decoupling technique by connecting the coils to low-input-impedance preamplifiers as shown in Figure 2.16.

To understand how the decoupling scheme is obtained, let us consider a system of two identical coils: coil 1 and coil 2 coupled through the mutual inductance M as shown in Figure 2.20. An AC current I_1 flowing in coil 1 induces a current I_2 in coil 2. The output voltage in coil 1 due to the induced NMR signal V_1, current I_1 and mutual inductance M is given by (24):

$$V_{out} = V_1 + (R_1 + i(\omega L_1 - \frac{1}{\omega C_1}))I_1 + \mathrm{i}\omega M I_2 \ . \qquad [2.70]$$

In Eq. [2.70], the second and third terms are the noise related to coil 1 and coil 2, respectively. The second term can be minimized by tuning and matching coil 1. The third term vanishes if either M = 0 or I_2 = 0. M = 0 is possible only between adjacent coils through proper overlapping between the two coils or using lumped elements such as a capacitor or an inductor between the coils. The interaction between nonoverlapping coils

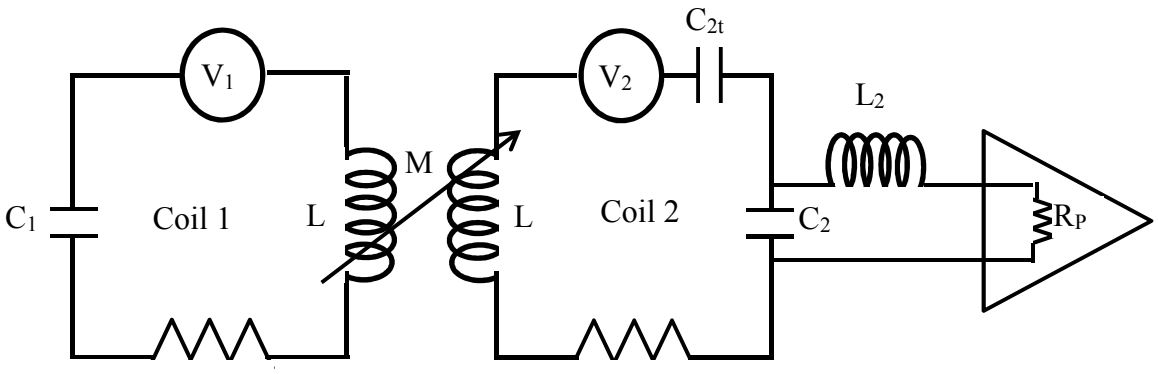

Figure 2.20: A system of two identical RF coils: coil 1 and coil 2 coupled through a mutual inductance M and connected to a low-impedance preamplifier.

in the array can be forced to zero by making $I_2 = 0$ in Eq. [2.70]. This technique is called preamp decoupling.

Using a low-input impedance preamplifier, the preamplifier resistance, $R_P \approx 0$, the matching inductor L_2 and the capacitor C_2 can be adjusted such that the combination can be tuned to the target frequency to form a trap when looked at from the side of the RF coils so that $I_2 = 0$. In this coil-preamplifier design, the preamplifier performs a voltage measurement across the coil 2 (33). At the same time with iterative adjustment of L_2 and C_2, the RF coil can be matched to 50 Ω when looked at from the preamplifier provided the preamplifier has a noise match of 50 Ω.

Preamplifier decoupling is measured on the bench by setting the network analyzer to S21 measurement and measuring the S21 values before and after the preamp is inserted in the feed board provided the RF coil is connected to the feed board. This difference is ~ -30 to -40 dB. Typical S21 curves for the preamplifier decoupling measurement before and after the preamplifier is inserted into the feed board are shown in Figure 2.21.

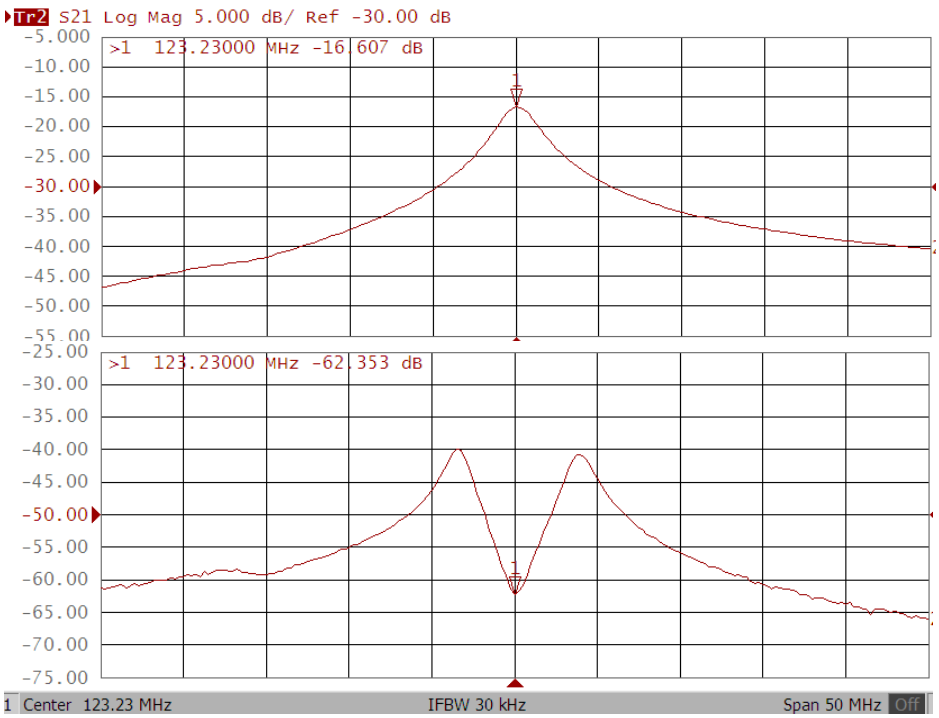

Figure 2.21: The S21 curves for preamp decoupling measurement on the bench using a set of decoupled picker coils: (a) without preamp in the feed board and (b) with preamp in the feed board.

2.4 ^{31}P NMR Spectroscopy

In vivo ^{31}P MRS is very useful in noninvasive studies of the high energy phosphate metabolites that play a key role in energy metabolism and phosphorous containing markers of disease. Since ^{31}P has a nuclear spin of ½, gyromagnetic ratio of 17.24 MHz/T and 100% natural abundance, it is useful in NMR spectroscopy. Through the use of ^{31}P MRS, one can assess metabolites like adenosine triphosphate (ATP), phosphocreatine (PCr), inorganic phosphate (Pi), phosphodiesters, and phosphomonoesters. ATP has three peaks: α-, β-, and γ-ATP, while the two peaks of adenosine diphosphate (ADP) coincide with α- and γ-ATP. Other phosphorus-containing biological molecules (such as membrane phospholipids bound to macromolecule) are

either MR invisible due to short T_2 or represented by broad signals underlying the metabolite peaks (16). A typical ^{31}P spectrum is shown in Figure 2.22. By convention, the PCr peak is assigned as the chemical shift reference point of 0.00 ppm. Other peaks such as Pi, γ, α, and β–ATPs appear respectively at 5.02 ppm, -2.48 ppm, -7.52 ppm, and -16.26 ppm. Because of the short T_2 relaxation time of ^{31}P, phosphorous spectroscopy requires a pulse sequence with short TE such as the FID pulse sequence.

2.4.1 Chemical Shift

When a nuclei system with non-zero spin is placed in an external magnetic field, B_0, the net magnetic field experienced by a particular nucleus is a sum of the external magnetic field and the field due to nearby nuclei and electrons and is given by:

$$B_{eff} = B_0(1-\sigma), \qquad [2.71]$$

where σ indicates the shielding constant which depends on the electron density around the nucleus. This extra field alters the Larmor frequency of the nucleus by a small fraction, known as the chemical shift. The expression of Larmor frequency incorporating chemical shift becomes,

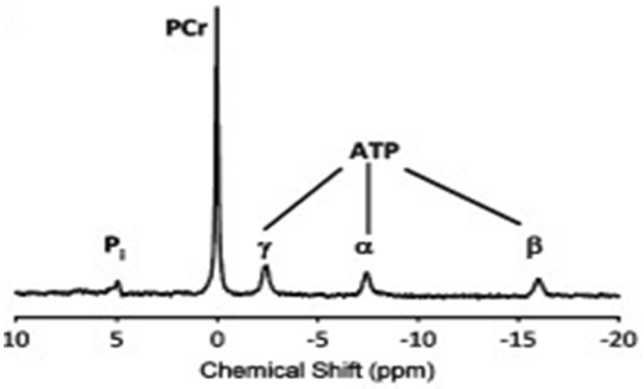

Figure 2.22: Typical ^{31}P MR spectrum.

$$\omega_L = \gamma B_0(1-\sigma). \quad [2.72]$$

Eq. [2.72] shows that the frequency shift of Larmor frequency of the metabolite containing different chemical groups depends both on the shielding constant and the strength of the external magnetic field. Therefore, the higher the external magnetic field is, the greater the frequency separation between the peaks is. The chemical shift is usually expressed in a dimensionless unit of ppm (part per million) to ease comparisons among the data acquired at different fields. An example of chemical shift is the shifting of the resonant frequency of fat protons to a lower frequency side by nearly 3.5 ppm in the frequency encoding direction (readout direction) relative to water protons.

Due to chemical shift, we get an NMR spectrum with a series of peaks. A typical example of ^{31}P MR spectrum is illustrated in Figure 2.22. The frequencies of the peaks reflect the electronic environments of the resonant nucleus. By analyzing the peaks in NMR spectrum, one can identify the type of metabolites present in the tissue and estimate their concentration. This procedure forms a basis for MRS.

2.4.2 Chemical Shift Imaging (CSI)

Due to the short T_2 of *in vivo* ^{31}P in phosphorous metabolites, ^{31}P spectroscopy requires a pulse sequence with short TE such as the chemical shift imaging FID (CSI-FID) sequence. CSI-FID, also known as multivoxel spectroscopy acquires an FID by employing an excitation pulse followed by a phase encoding pulse. Since frequency encoding is not allowable in spectroscopy, phase encoding has to be used in the direction whose spatial information is required. It is applied in one direction for 1D CSI, in two directions for 2D CSI and in three directions for 3D CSI. Figure 2.23 is the coronal slice

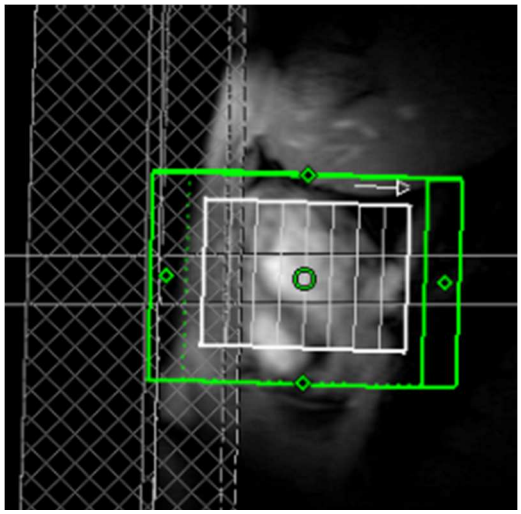

Figure 2.23: Coronal slice of a lamb thorax obtained using 1D CSI with 8 phase encoding steps. The saturation slabs are placed on the thorax wall to eliminate signal contamination originating from the muscle in the thorax wall.

of a lamb's heart obtained using a 1D CSI-FID sequence with eight phase encoding CSI grids. The signal from the chest wall is saturated by a saturation slab on the chest wall. One can use 3D CSI with 8 x 8 x 8 phase encoding steps to get high spatial resolution. But the acquisition time becomes very long (512 TRs) which is almost impossible for *in vivo* applications.

2.4.3 Bloch Equation for Creatine-Kinase (CK) Reaction

In the CK reaction, the CK enzyme catalyzes the reaction in which a chemical exchange of a phosphate group between phosphocreatine (PCr) and γ-adenosine triphosphate (γ-ATP) takes place:

$$PCr^{2-} + ADP^{-} + H^{+} \rightleftarrows Cr + ATP^{2-}$$

The reaction proceeds in forward and backward directions with rate constants k_f and k_r, respectively. The Bloch equation [2.33] for longitudinal magnetization of PCr and γ-ATP

can be written as:

$$\frac{dM_{PCr}(t)}{dt} = \frac{M^o_{PCr}(t) - M_{PCr}(t)}{T_{1PCR}} - k_f M_{PCr}(t) + k_r M_{\gamma ATP}(t) \quad [2.73]$$

$$\frac{dM_{\gamma ATP}(t)}{dt} = \frac{M^o_{\gamma ATP}(t) - M_{\gamma ATP}(t)}{T_{1\gamma ATP}} + k_f M_{PCr}(t) - k_r M_{\gamma ATP}(t). \quad [2.74]$$

In magnetization transfer ^{31}P phosphorous spectroscopy (MT-^{31}P-MRS), an MT pulse is applied to selectively saturate either at the γ-ATP so that $k_r = 0$ or at the PCr to make $k_f = 0$. With a MT pulse at γ-ATP to evaluate k_f, Eqs. [2.73] and [2.74] become:

$$\frac{dM_{PCr}(t)}{dt} = \frac{M^o_{PCr}(t) - M_{PCr}(t)}{T_{1PCR}} - k_f M_{PCr}(t). \quad [2.75]$$

$$M_{\gamma ATP}(t) = 0. \quad [2.76]$$

With $R_1' = {}^1/_{T_{1PCr}} + k_f = R_1 + k_f$, Eq. [2.75] becomes:

$$\frac{dM_{PCr}(t)}{R_1 M^o_{PCr}(t) - R_1' M_{PCr}(t)} = dt\,. \quad [2.77]$$

Solving Eq. [2.77] in the limit $t \approx \infty$, we get the expression of steady state magnetization:

$$M_{ss}^{PCr} = \frac{R_1}{R_1'} M^o_{PCr} = \frac{R_1' - k_f}{R_1'} M^o_{PCr}\,. \quad [2.78]$$

Rearranging Eq. [2.78], we get an expression for the rate constant of the CK reaction:

$$k_f = R_1'\left(1 - \frac{M_{ss}^{PCr}}{M^o_{PCr}}\right). \quad [2.79]$$

As γ-ATP is only 2.5 ppm apart from the PCr peak, the MT pulse used to selectively saturate the γ-ATP peak is never perfectly selective, i.e., the pulse also affects the PCr peak a little bit due to the effect of RF bleed-over. With this RF-bleed-over effect of an MT pulse, Eq. [2.75] can be written as:

$$\frac{dM_{PCr}(t)}{dt} = \frac{M^o_{PCr}(t) - M_{PCr}(t)}{T_{1PCr}} - k_f M_{PCr}(t) - \eta M_{PCr}(t), \quad [2.80]$$

where η is the rate of loss of PCr magnetization due to RF bleed-over effect. The

expression for PCr magnetization with RF-bleed-over effect, $M_{PCR}^{o\prime}$ can be written as:

$$M_{PCR}^{o\prime} = \frac{R_1}{R_1+\eta} M_{PCr}^{o} \quad [2.81]$$

Using $R_1'' = R_1 + k_f + \eta$ and Eq. [2.81], Eq. [2.80] can be solved to get the expression:

$$\eta = \frac{R_1'' M_{ss}^{PCr}}{M_o} \left(\frac{M_o}{M_o'} - 1\right) \quad [2.82]$$

2.5 Diffusion MRI

Water molecules in tissue undergo Brownian motion, which is the random microscopic displacement due to thermal agitation. This property of water molecules is called diffusion. Diffusion MRI uses this property of water molecules to generate contrast in MRI images. In intact tissue, movement of water molecules is restricted by cell membranes. Diffusivity of water molecules is increased if the membrane ruptures. Diffusion MRI uses this property of water molecules in the NMR signal by using bipolar magnetic field gradient pulses to identify certain lesions and damages in the tissue (34).

In most tissues, the diffusive motion of water molecules is not free where the water molecule diffuses in all direction with equal probability; it is rather restricted or hindered by the tissue structures, where it is faster along one direction and slower along others. For example, the diffusion of water in human CSF is free. Restricted diffusion occurs in a restricted geometries such as intracellular space, intra-axonal space etc. The diffusion of a water molecule in restricted geometries obeys a non-Gaussian distribution. Hindered diffusion refers to the diffusion of water in hindered spaces such as extracellular space and extra-axonal space where the water is comparatively much more mobile than that in restricted space. Hindered diffusion obeys a Gaussian displacement pattern given by (5):

$$P(r,t) = \frac{1}{(4\pi Dt)^{1/2}} e^{-\frac{<r-r_0>^2}{4Dt}}, \quad [2.83]$$

where D is the diffusion coefficient and $< r - r_0 >$ is the mean displacement during time t and is given by:

$$< r - r_0 > = \sqrt{6Dt}\ . \quad [2.84]$$

2.5.1 Bloch Equation with Diffusion Term

Torrey in 1956 added the diffusion term in the Bloch equation. The modified Bloch equation is given by

$$\frac{d\vec{M}}{dt} = \gamma\vec{M} \times \vec{B} + \frac{(M_z^0(t) - M_z(t))}{T_1}\hat{z} - \frac{M_x(t)\hat{x} + M_y(t)\hat{y}}{T_2} + D\nabla^2\vec{M}(t). \quad [2.85]$$

In the presence of time varying gradient field, B field can be written as

$$\vec{B} = (\vec{G}.\vec{r})\hat{z}. \quad [2.86]$$

With Eq.[2.86] and using $M_{xy} = M_x + iM_y$, the transverse component of Eq. [2.85] can be written as

$$\frac{dM_{xy}}{dt} = \gamma(\vec{G}.\vec{r})M_{xy} - \frac{M_{xy}}{T_2} + D\nabla^2 M_{xy}, \quad [2.87]$$

of which solution can be:

$$M_{xy} = M_0 e^{-\frac{t}{T_2}} e^{-bD}, \quad [2.88]$$

where b, generally known by the term "b-value," describes the strength of diffusion gradient and timing according to the following relation,

$$b = \gamma^2 \int_0^{TE} (\int_0^t G(t')dt')^2 dt\ . \quad [2.89]$$

2.5.2 Diffusion Tensor Imaging

A diffusion tensor is a 3 x 3 symmetric covariance matrix that is used to study the diffusion property of anisotropic media such as diffusion of water in axon where water diffuses more rapidly along the axial direction than along the radial direction. Mathematically, the diffusion tensor, D can be expressed as:

$$D = \begin{bmatrix} D_{xx} & D_{xy} & D_{xz} \\ D_{yx} & D_{yy} & D_{yz} \\ D_{zx} & D_{zy} & D_{zz} \end{bmatrix}. \quad [2.90]$$

The matrix element D_{xy} is positive and symmetric, $D_{xy} = D_{yx}$, $D_{xz} = D_{zx}$, and $D_{yz} = D_{zy}$. As a result, diffusion weighted imaging (DWI) data must be acquired in at least six non-collinear directions in order to solve the matrix equation $D\hat{e} = \lambda\hat{e}$ (35). The eigenvalues λ_1, λ_2, and λ_3 and corresponding eigenvectors $\hat{e}_1$, $\hat{e}_2$, and $\hat{e}_3$ of the diffusion tensor can be found from the diagonalization of D. The eigenvalues and eigenvectors describe the apparent diffusivities and the directions along the axes of the local symmetry system and can be visualized using ellipsoid representation with ellipsoidal radii along principal axes indicating eigenvalues and their direction indicating the eigenvectors as shown in Figure 2.24 (36). The diffusion tensor matrices commonly known as diffusion tensor indices such as fractional anisotropy (FA), mean diffusivity (MD), axial diffusivity (AD), radial diffusivity (RD), and trace can be derived from these eigenvalues using the following relations:

$$FA = \sqrt{\frac{3}{2}} \frac{\sqrt{(\lambda_1 - <D>)^2 + (\lambda_2 - <D>)^2 + (\lambda_3 - <D>)^2}}{\sqrt{(\lambda_1^2 + \lambda_2^2 + \lambda_3^2)}} \quad [2.91]$$

For isotropic diffusion, $\lambda_1 = \lambda_2 = \lambda_3$ so that FA is 0 while for anisotropic diffusion, the magnitude of these eigenvalues is markedly different ($\lambda_1 > \lambda_2 > \lambda_3$). So, the value of FA

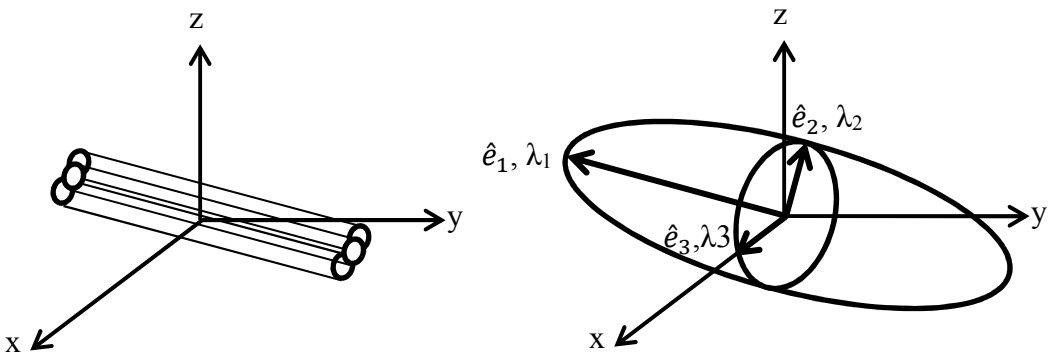

Figure 2.24: Schematic diagram of ellipsoid representing the diffusion displacements in fibers where the direction of greatest diffusivity is along the axial direction.

is scaled from 0 to 1.

$$MD = \frac{\lambda_1 + \lambda_2 + \lambda_3}{3} \quad [2.92]$$

$$AD = \lambda_{||} = \lambda_1 \quad [2.93]$$

$$RD = \lambda_{\perp} = \frac{\lambda_2 + \lambda_3}{2} \quad [2.94]$$

$$Trace\ (D) = \lambda_1 + \lambda_2 + \lambda_3 \quad [2.95]$$

These diffusion metrics are useful in demonstrating the relationship to the white-matter pathology. For instance, the radial diffusivity is used to study the demyelination and axial diffusivity is used to study the axonal damage in white-matter (37).

2.5.3 Basic Diffusion MRI Pulse Sequences

2.5.3.1 Spin Echo-Based DWI sequence

The spin echo (SE) based DWI sequence with Stejskal and Tanner diffusion gradients (of width δ, and spacing between the leading edges Δ) (34) before and after the 180° refocusing pulse is shown in Figure 2.25. The phase accumulation experienced by a spin in the presence of a magnetic field gradient applied for time t is given by

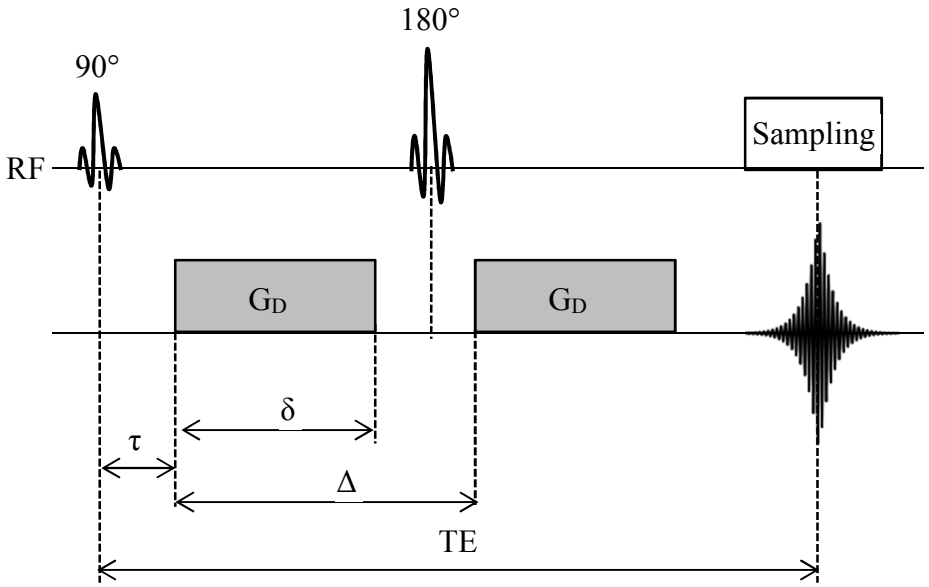

Figure 2.25: Diffusion weighted spin echo pulse sequence diagram with diffusion weighting gradient G_D, duration δ, and spacing Δ.

$$\phi(t) = \gamma B_0 t + \gamma \int_0^t G_D(t').x(t')dt', \quad [2.96]$$

where the first term is the phase accumulation due to the main magnetic field B_0 and the second term is that due to gradient field. The total phase shift of a particular spin at time TE in Figure 2.25 is therefore

$$\phi(TE) = \gamma \int_\tau^{\tau+\delta} G_D(t').x(t')dt' - \gamma \int_{\tau+\Delta}^{\tau+\Delta+\delta} G_D(t').x(t')dt' \quad [2.97]$$

If there were no motion, the first and the second term of Eq. [2.97] would equal so that they cancel each other resulting in net zero phase. However, in the case of diffusion, the displacement *x(t)* caused by random motion is not the same for the two diffusion gradient duration which is responsible for signal loss. The signal equation at time TE can be expressed as

$$S = S_0 e^{(-TE/T_2)} e^{-bD}, \quad [2.98]$$

where D is apparent diffusion coefficient (ADC) and b is diffusion sensitizing factor

which can be expressed as:

$$b = \gamma^2 G^2 \delta^2 \left(\Delta - \frac{\delta}{3}\right). \quad [2.99]$$

Using Eq. [2.98] and performing two experiments one with b = 0 and the other with finite b value ADC can be calculated for isotropic medium in which molecules diffuse equally in all direction using

$$D = -\frac{1}{b - b_0} \ln\left(\frac{S_b}{S_{b_0}}\right). \quad [2.100]$$

2.5.3.2 Stimulated Echo-Based DWI Sequence

To get the greater diffusion weighted contrast and less T_2 weighted effect, high-b DWI (38) and even ultra-high-b DWI (UHb-DWI) (39) have been used. UHb-DWI using SE based sequence requires a long Δ which dramatically increases TE leading to a strong T_2 decay and resulting in a poor SNR (40). To resolve this problem stimulated echo (STE) based DWI sequence (41,42) with three RF pulses (RF pulse must not necessarily be 90° for STE) with two diffusion encoding gradients: one between 1st and 2nd RF pulse and the other after 3rd RF pulse as shown in Figure 2.26 have been used. The 1st 90° pulse rotates the magnetization in transverse plane where they lose phase coherence. The 2nd 90° pulse flips the half of this magnetization to the longitudinal direction where the memory of their phase is stored during TM (the duration between 2nd and 3rd RF pulses). They are only affected by much slower T_1 decay and not by gradient fields and T2 decay during TM so that DW signal can be well preserved even with a long Δ. The 3rd RF pulse restores the phase angles again to the transverse plane with reversed sign so that the magnetization vectors converge to form a DWSTE (43) at time TE+TM. TE here is the sum of duration between the 1st and 2nd RF pulse and that between 3rd RF pulse and the

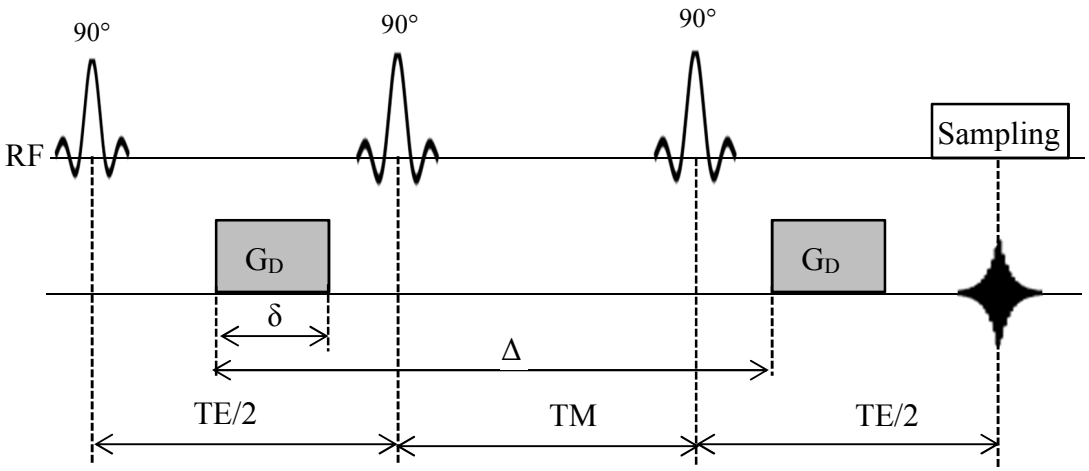

Figure 2.26: Diffusion weighted stimulated echo pulse sequence diagram with a train of three RF pulses and diffusion gradient applied after the 1st and 3rd RF pulses.

center of k space during which magnetization undergoes T_2 decay. The signal equation of STEDWI is given by

$$S = \frac{1}{2} S_0 e^{(-TE/T_2)} e^{(-TM/T_1)} e^{-bD}. \quad [2.101]$$

CHAPTER 3

DESIGN AND DEVELOPMENT OF A GENERAL PURPOSE TRANSMIT/RECEIVE (T/R) SWITCH FOR 3T MRI, COMPATIBLE FOR A LINEAR, QUADRATURE AND DOUBLE-TUNED RF COIL

This chapter relies on the paper entitled "Design and development of a general-purpose transmit/receive (T/R) switch for 3T MRI, compatible for a linear, quadrature, and double tuned RF coil" published in the journal Concept of Magnetic Resonance Part B (CMRB) in April 2016, and authored by Bijaya Thapa, Joshua Kaggie, Nabraj Sapkota, Deborah Frank, and Eun-Kee Jeong.

3.1 Abstract

This work presents the design and development of a general purpose T/R switch for MR imaging and spectroscopy, compatible with single and double tuned RF coils using linear, quadrature, or both modes at a low cost and with minimum development time using simple electronic circuits. This T/R switch was demonstrated with a custom double tuned $^{1}H/^{31}P$ transmit receive surface RF coils built for ^{31}P MRS of a lamb's heart with surgically created congenital heart defects. Two passive trap circuits tuned to ^{1}H and ^{31}P frequencies fed from a common drive point were built to filter two different

frequency T/R switches. The T/R switch was built for a ^{1}H linear RF coil and ^{31}P quadrature RF coil. This T/R switch design is easily modifiable to linear, quadrature and double tuned RF coils of relatively wide range of frequencies, so as to enable imaging of proton and X-nuclei at 3T field. The performance of the custom T/R switch was tested with bench measurements of its isolation, insertion loss and switching time, under pulsed conditions, and on a phantom with a 3T magnet by comparing the signal to noise ratio with a commercial T/ R switch. A high isolation, low insertion loss and fast switching time in the range of nanoseconds were obtained on the bench. Identical isolation was observed under pulsed conditions. An improvement of about 29% gain in signal to noise ratio was obtained with this T/R switch compared to the commercial T/R switch.

3.2 Introduction

Magnetic resonance imaging/spectroscopy (MRI/S) of nuclei other than hydrogen is used to obtain information about metabolic processes in humans and animals (44–49). For nonproton MRI/S, ^{1}H MRI is essential for localization and shimming the region of interest (50–52), which cannot be done using the nonproton nuclei due to its low signal-to-noise ratio (SNR). The low SNR in nonproton MRI/S is mainly caused by the low concentration and gyromagnetic ratio of the nonproton nuclei in the human body (48,52,53). Therefore, a double tuned radio frequency (RF) coil, which requires appropriate transmit/receive (T/R) switching hardware, is generally desired for MRI/S of a nucleus other than ^{1}H. Double-tuned RF coils, which require appropriate hardware, reduce image registration problems and the inconvenience of physically replacing the RF coils and T/R switches for different nuclear experiments (54).

A T/R switch directs the high power RF signal from the RF amplifier to a transmit-receive RF coil and the low power nuclear magnetic resonance (NMR) signal from the RF coil to the preamplifier. One important role of the T/R switch is to protect the preamplifier from damage due to high power during the RF transmission (55), while allowing the NMR signal from the RF coil to be passed undistorted and undiminished to the preamplifier (56). Several strategies have been reported to protect the preamplifier from high power RF pulses during transmission such as using ferrite based circulators in combination with PIN diodes as passive components (56), LC resonant circuits switchable by field effect transistor (FET) (57), transistor based technologies (58) or microelectromechanical system (MEMS) (59). Another commonly used method in MRI incorporates switches deploying PIN diodes as active components and other circuitry enabled by PIN diodes. This method is used due to its low insertion loss in the forward bias state, high isolation in the reverse bias state, very short switching time, high power handling capability, low distortion, small physical size and high reliability (60). We adapted the later technique to build the general-purpose T/R switch. For double-frequency T/R switching, a passive high-power RF switch consisting of two trap circuits directs the RF signal from the MRI system to the T/R switch with the appropriate frequency without need of manually replacing the T/R switch during the experiment.

In the present work, we designed and developed a general-purpose T/R switch with high isolation and low insertion loss for use with $^{1}H/^{31}P$ dual tuned transmit-receive lamb RF coils. We have focused on increased isolation to the receive path during the RF transmission. This is particularly important for imaging a small animal or specimen in a clinical MRI system, which is equipped with a large RF power amplifier.

3.3 Methods

Most clinical MR systems have a single RF transmit port for both ^{1}H and ^{31}P frequencies and multiple receive ports. A high power RF switch consisting of two trap circuits are positioned prior to the T/R switches to passively switch the RF pulses to either the ^{1}H or ^{31}P T/R switch for ^{1}H MRI or ^{31}P MRS, respectively (53). Depending on whether the RF coil is driven in linear or quadrature mode, the T/R switch can be linear or quadrature. Since the $^{1}H/^{31}P$ double tuned transmit-receive RF coils consist of a ^{1}H linear loop and quadrature ^{31}P loops, the ^{1}H T/R switch is linear and the ^{31}P T/R switch is quadrature.

3.3.1 $^{1}H/^{31}P$ Dual-Tuned RF Coils

The $^{1}H/^{31}P$ RF coils were optimized for the ^{31}P signal detection at the heart of four- to six-week-old lambs with surgically created congenital heart defects (61,62). The RF coils were mounted on a laboratory-built frame made of fiberglass cloth (917, Evercoat), epoxy (105 part 1, West System) and hardener (206 part 2, West System). The ^{31}P RF coils consisted of a 14.5 cm long and 7.1 cm wide butterfly loop of 4 mm wide copper strip and a central crossover angle 165° overlapped with an 8.7 cm long and 8.5 cm wide rectangular loop of copper strip of width 4 mm as shown in Figure 3.1. The long axis of the butterfly coil was set perpendicular to the main magnetic field during the MRI/S experiment. These ^{31}P loops were made by etching a copper clad laminate (FR9150R, DuPont Electronic Technologies, Research Triangle Park, NC, USA) which contains copper foil of 305 g/m^2 mass on one side. These RF coils were separately matched to 50 Ω, tuned to 49.9 MHz and decoupled adjusting the overlapping region of

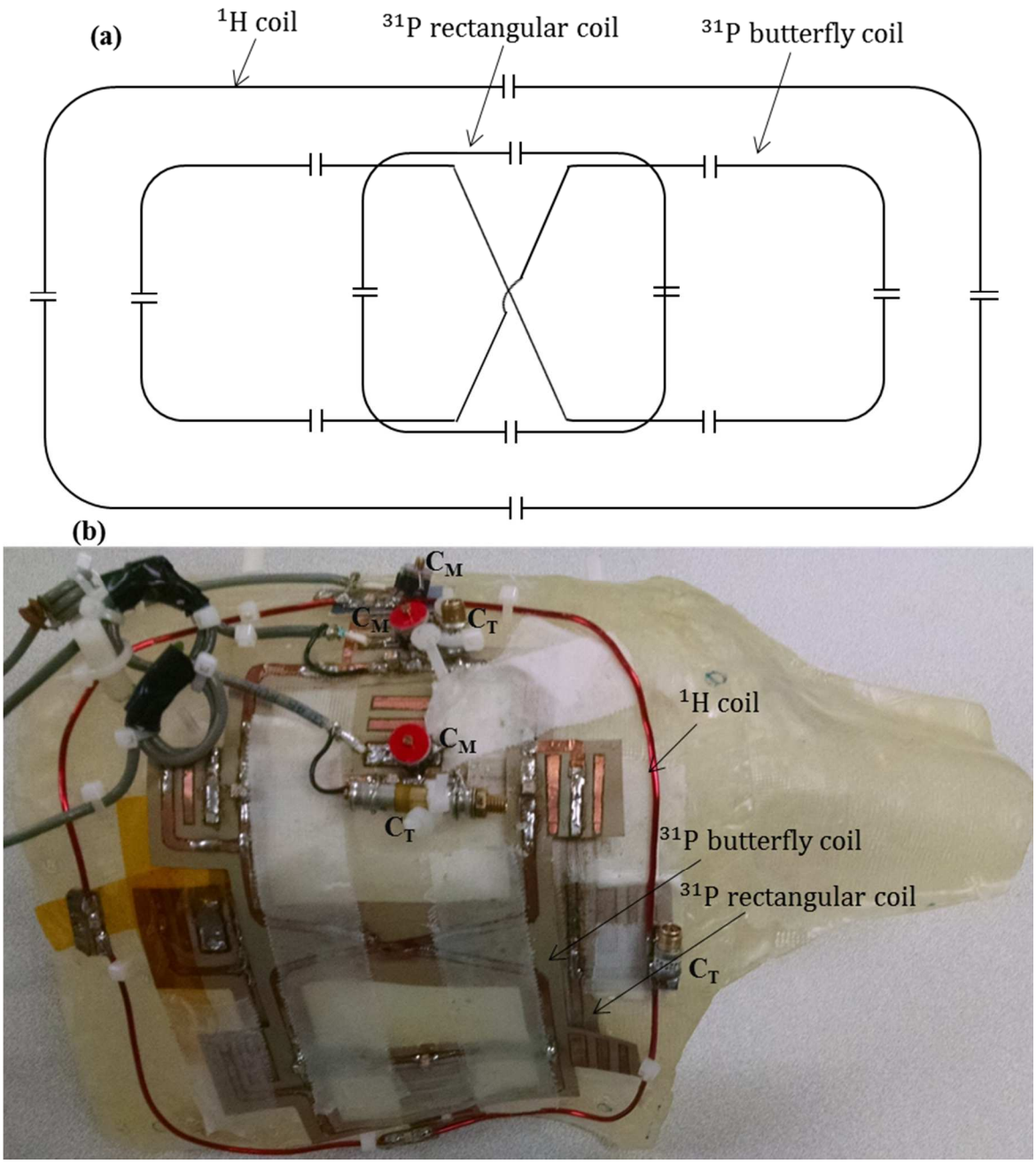

Figure 3.1. The ^{1}H/^{31}P dual tuned lamb RF coils: (a) circuit diagram and (b) photograph. The ^{31}P RF coil consisted of a butterfly loop and an inner rectangular loop decoupled geometrically for a quadrature mode. The outer rectangular loop was the ^{1}H RF coil.

the RF coils (63) utilizing the orthogonal nature of B_1 fields produced by the coils. Their coupling was minimal when their centers were on top of each other.

Five nonmagnetic 100 pF capacitors (American Technical Ceramics, Huntington Station, NY, USA) accompanied by a parallel combination of a 82 pF capacitor and one 1-25 pF high voltage trimmer capacitor (Voltronics Corp., Denvile, NJ, USA) were used in six equal segments of butterfly RF coil for tuning and 8-80 pF trimmer capacitor (Sprague-Goodman Electronics, Westbury, NY, USA) for matching of the butterfly RF coil while one 82 pF capacitor and a parallel combination of 27 pF capacitor and 1-60 pF high voltage trimmer capacitor were used in two equal segments of the rectangular RF coil for tuning and one 8-80 pF trimmer capacitor for matching.

The ^{1}H RF coil was tuned to 123.23 MHz frequency using three 12 pF capacitors and one 1-25 pF high voltage trimmer capacitor in four equal segments of the RF coil and matched to 50 Ω using 3-36 pF trimmer capacitor. The ^{1}H RF coil that surrounded the ^{31}P RF coil as shown in Figure 3.1 is 18.5 cm long and 15 cm wide and was made of a solid copper wire of 1.7 mm diameter. Copper clad laminate was used to enable easy positioning and removal of the ^{31}P RF coil during decoupling. This design allowed us to separately tune and match the ^{1}H and ^{31}P RF coils (64). The ^{1}H RF coil was in quadrature mode with the ^{31}P butterfly RF coil and it is decoupled with the ^{31}P rectangular RF coil by making its surface area large compared to the rectangular RF coil.

3.3.2 T/R Switch

The T/R circuitry for our $^{1}H/^{31}P$ dual-tune RF coil consists of a linear T/R switch for the ^{1}H RF coil and a quadrature T/R switch for the ^{31}P RF coil. A double-layered

circuit layout was designed using Eagle software (Cadsoft, version 6) and a printed circuit board (PCB) was fabricated on a 10 x 8 cm^2 circuit board. The board diagram is shown in Figure 3.2, which indicates the bottom layer of the board being used as a ground plate. The islands on the board were designed such that the same board can be utilized to build both linear and quadrature T/R switches for any MR active nucleus at a 3T magnetic field. There are additional ports on the RF coil side of the board to connect the transmit and receive paths for linear operation and several additional solder pads and connections for electronic components required for a quadrature T/R switch, such as

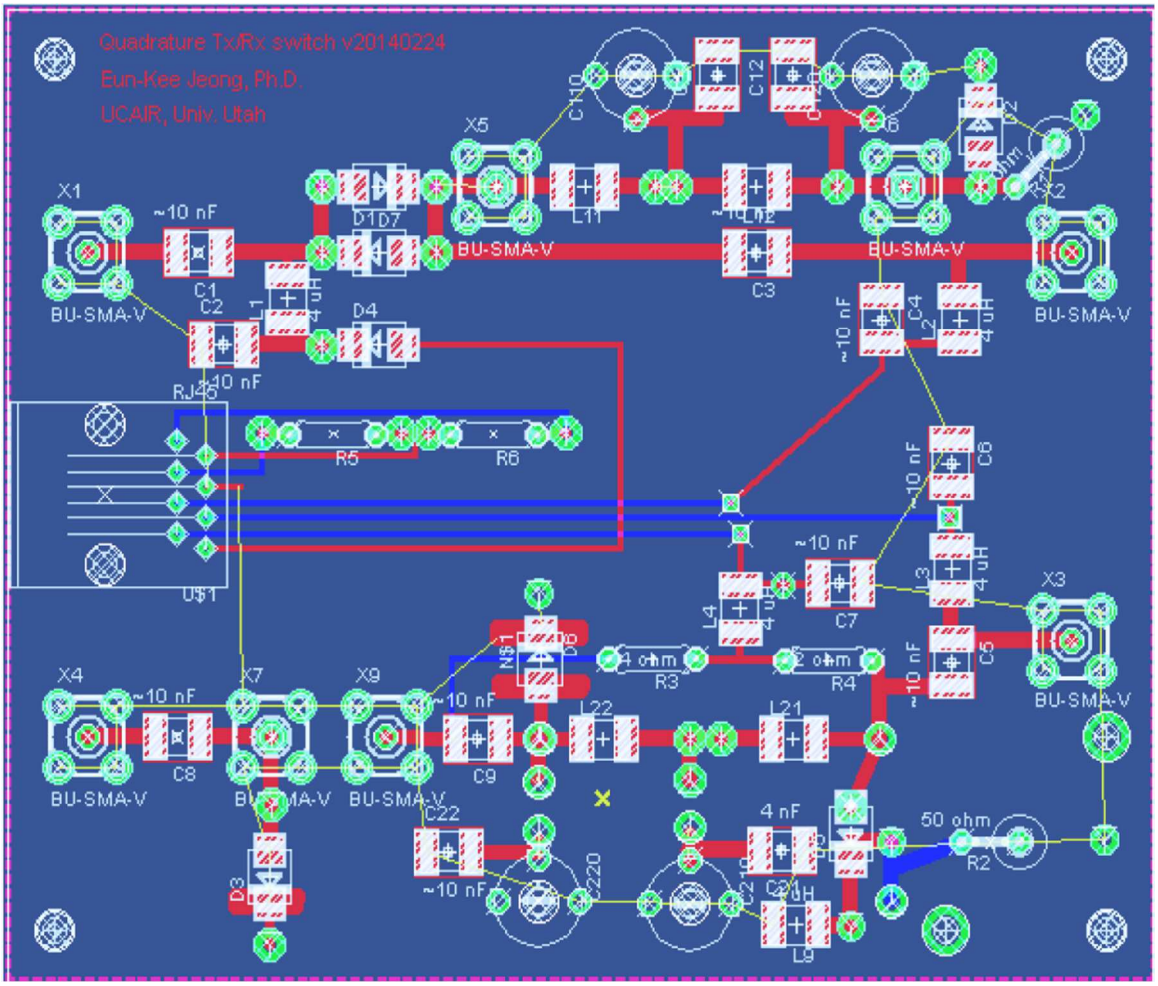

Figure 3.2: The board diagram of T/R switch.

capacitors, resistors, inductors, diodes and quarter wave cables. The circuit diagrams of quadrature and linear T/R switches are shown in Figs. 3.3a and 3.3b. The transmit path consists of a single serial PIN-diode, D_1 (MA4P7104F, MACOM Technology Solutions Inc.) that is DC biased during transmit, whereas the receive path consists of a Pi-network and a quarter wave cable in series; each is terminated by a shunt PIN-diode, D_2 to improve the isolation. The combination is followed by a shunt crossed-diode pair (not shown in Figure) in a separate box for additional protection of the preamplifier.

The quarter wave cable was made from a 50 Ω coaxial cable (B7805R, type RG-

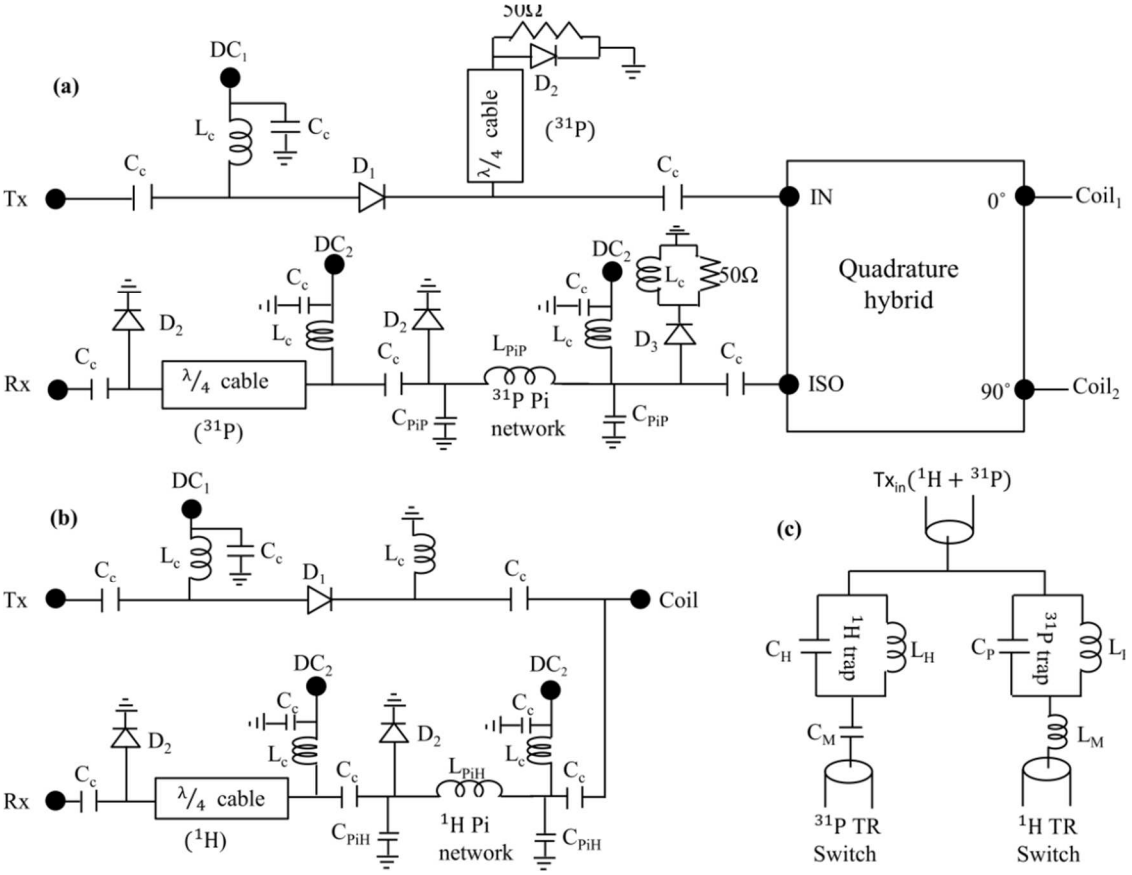

Figure 3.3: The circuit diagram of the (a) quadrature ^{31}P T/R switch accompanied by a quadrature hybrid to split the RF pulse to the quadrature RF coil and to combine the MR signal from the coil in quadrature mode, (b) ^{1}H linear T/R switch and (c) high-power passive RF switch.

174, Belden) at lengths of 40 cm and 102 cm for the ^{1}H and ^{31}P frequencies, respectively. A second quarter-wave circuit consists of a Pi-network (C_{Pi}-L_{Pi}-C_{Pi}) using an inductor and two capacitors. The values of inductance (L_{Pi}) and capacitance (C_{Pi}) of this Pi-network are given by (60):

$$L_{Pi} = \frac{Z_o}{2\pi f}, \quad [3.1]$$

$$C_{Pi} = \frac{1}{2\pi f Z_0}. \quad [3.2]$$

Here, Z_0 is 50 Ω so that the impedance matches to that of the cable. The values at 3T are 0.065 μH and 25.8 pF for the ^{1}H quarter wave circuit and 0.160 μH and 63.8 pF for the ^{31}P quarter wave circuit, respectively. 15,000 pF chock capacitors, C_c (GRM31BR72E153KW01L, Murata Electronics) and 33 μH RF choke inductors, L_c (1812CS_333X_L_, Coilcraft) are used to block direct current (DC) and RF, respectively. The only frequency dependent sections of the T/R switch are the quarter wave cable and the Pi-network. By changing the length of the quarter wave cable, the LC values of the Pi-network, and the LC element values of the trap, the T/R switch can be adjusted to work at any frequency in a 3 Tesla magnetic field.

Using coil control files within the Siemen's MRI system that control the duration and time of PIN current, the PIN-diodes are forward biased with +100 mA DC during transmission and reverse biased with -30 V DC during reception. The PIN current DC_1 was used in transmit path while the PIN current DC_2 was used in receive path to forward bias the PIN-diodes. DC_2 was split equally between two PIN-diodes in linear T/R switch using choke inductors of same DC resistances and among three PIN-diodes in quadrature T/R switch using choke inductors of different DC resistances. The PIN current 33 mA is enough to forward bias a PIN diode in the receive path of quadrature T/R switch, as seen

on bench measurement. During forward biasing, the PIN-diode is actively shorted and has low impedance (~ 0.5 Ω), while during reverse biasing the diode is open and has high impedance (~ 600 KΩ). The forward biasing of the PIN-diodes at the end of the quarter wave cable and the Pi-network open the receive path for the RF pulse, while the reverse bias makes the receive path act like a 50 Ω cable. This can be seen from the expression of the input impedance of the quarter wave cable of length l=λ/4 with characteristic impedance Z_o and connected to a load impedance Z_L (65):

$$Z_{in} = Z_o \frac{Z_L + jZ_o \tan\left(\frac{2\pi l}{\lambda}\right)}{Z_o + jZ_L \tan\left(\frac{2\pi l}{\lambda}\right)} = \frac{Z_o^2}{Z_L}. \quad [3.3]$$

In the case of a Pi-network, when the output is short circuited by a PIN-diode, the capacitive impedance at the input side is equal to the inductive impedance so that input impedance becomes infinity (23) for an ideal LC network. However, for a real inductor (which is always associated with lossy resistance), the input impedance of the LC network resonating at frequency ω_o and having quality factor Q is given by $Q\omega_o L$ (typically larger than1KΩ) (66). When diode is off by reverse bias, LC values are chosen according to Eqs. (1) and (2) such that the Pi-network provides impedance equal to 50 Ω. Thus, the RF pulse from transmitter is routed only to the RF coil during the transmission and the NMR signal from the RF coil only to the receive-pathway during the reception.

A commercial quadrature hybrid (10540-3, Anaren Microwave Inc., East Syracuse, NY) with port isolation of -20 dB and insertion loss of -0.5 dB is placed after the quadrature T/R switch. In order to absorb the reflected powers due to any imperfect matching between the quadrature RF coil and quadrature hybrid, additional circuitry is added on both transmit and receive paths of the quadrature T/R switch. A shunt quarter wave cable followed by parallel combination of a PIN diode, D_2 and a 50 Ω resistor (67)

is added after the PIN-diode, D_1 on the transmit path. A shunt PIN-diode, D_3 followed by a parallel combination of a 33 μH inductor and a 50 Ω resistor is placed prior to the Pi-network on the receive path. For additional protection of the preamplifier, a crossed-diode pair consisting of two fast standard switching diodes (1N914B, Fairchild Semiconductor Corp., San Jose, CA) in a separate box is placed between the receive path of the T/R switch and the preamplifier.

3.3.3 High-Power Passive RF Switch

The high-power passive RF switch was constructed on PCB formed by etching a copper coated board with PCB etching solution (22-239, GC electronics). The high-power passive RF switch consisted of two parallel LC trap circuits followed by an inductor and a capacitor (68) as shown in Figure 3.3c. The ^{31}P trap was constructed using a 68 pF chip capacitor and a custom 6 turned inductor of 6 mm diameter while the ^{1}H trap was constructed using a 27 pF capacitor and a custom 3 turned inductor of 6 mm diameter. Magnet wire of 0.9 mm diameter was used to make the inductor, and the traps were tuned to the respective frequencies by stretching or compressing the inductor. The power handling capacity of the trap circuit depends on the voltage rating of the capacitor used in the circuit. Using a high voltage capacitor, the trap circuit can handle the increased power. The impedance of the trap circuit is given by:

$$Z = \frac{jwL}{1-w^2LC}. \qquad [3.4]$$

The trap provides ideally an infinite impedance at the frequency to which it is tuned and a low impedance at all other frequencies. The ^{1}H trap is slightly inductive at the ^{31}P frequency (47), while the ^{31}P trap is slightly capacitive at the ^{1}H frequency

(69,70). The inductive reactance of the ^{1}H trap at the ^{31}P frequency is given by:

$$Z_P = \frac{j\omega_H L_H \Upsilon_H \Upsilon_P}{\Upsilon_H^2 - \Upsilon_P^2}, \quad [3.5]$$

where, Υ_P and Υ_H are gyromagnetic ratios of ^{31}P and ^{1}H, respectively. The capacitive reactance of the ^{31}P trap for the ^{1}H frequency is given by:

$$Z_H = -\frac{j\omega_P L_P \Upsilon_P \Upsilon_H}{\Upsilon_H^2 - \Upsilon_P^2}. \quad [3.6]$$

To nullify the inductive reactance of the ^{1}H trap at the ^{31}P frequency and the capacitive reactance of the ^{31}P trap at the ^{1}H frequency, a capacitor C_M (132 pF) and an inductor L_M (single turned, 6 mm diameter) were added to the ^{1}H trap and ^{31}P trap, respectively. Thus, the high-power passive RF switch was built to automatically direct the ^{1}H RF pulse to the ^{1}H T/R switch and the ^{31}P RF pulse to the ^{31}P T/R switch without the loss of transmit power.

3.3.4 Bench Tests

The performances of the T/R and passive RF switches were measured using a vector network analyzer (E5061B ENA Series, Agilent Technologies, Englewood, Colorado, USA). An RF combiner/splitter was used to combine the signals from the quadrature hybrid during transmission and split a signal from the network analyzer into two with 90° phase difference during reception before feeding to the quadrature hybrid for the bench measurement.

We also measured the switching time of the T/R switches using a rectangular RF pulse with 100 μs width from a NMR pulse-programmer board (RadioProcessor-G, SpinCore Technologies, Inc. Gainesville, FL USA) at frequencies of 49.9 MHz and 123.23 MHz. The transmit pulse from the RadioProcessor-G was split to channel 1 of an

oscilloscope (2465A, Tektronix, Beaverton, OR, USA) and the Tx input port of the T/R switch. The output of the T/R switch was fed to channel 2 of the oscilloscope. The switching time of the T/R switch is given by the time lag between the two pulses on the scope.

3.3.5 MRI Experiments

The isolation measurement of the ^{31}P and ^{1}H T/R switches was performed under high power pulsed conditions on a 3T clinical MRI system (Tim-Trio, Siemens Medical Solution, Erlangen, Germany) equipped with narrowband 34 kW and broadband 10 kW RF amplifiers for ^{1}H and other MR active nuclei, respectively, using an FID pulse sequence with a rectangular RF pulse of 400 μs duration with variable transmit gain from 50 V to 200 V. The RF power was fed to the Tx port of the T/R switch and the voltages at the coil and Rx ports of the T/R switch were measured on the 50 Ω terminated oscilloscope with two 10 W/10 dB attenuators (10-A-MFN-10, Bird Electronic Corp., Solon OH, USA) in series at its input. The output of T/R switch was measured by terminating its coil port to 50 Ω in the case of a linear T/R switch, while in the case of a quadrature T/R switch it was measured in two ways: by terminating its coil port to 50 Ω and by connecting the coil port to the ^{31}P quadrature coil.

We also performed MRI and MRS on a 250 mL saline bag phantom replacing saline water with 250 mL of distilled water dissolved with 23 tablets of phosphate buffered saline (PBS). The ^{1}H image of the PBS phantom was acquired with a localizer using the ^{1}H T/R switch and ^{1}H RF coil of the double tuned RF coils. Three MRS experiments were performed on the PBS phantom using the ^{31}P RF coil of the double

tuned RF coils and FID pulse sequence with TR/TE = 4 s/0.3 ms, hard RF pulse of 400 μs duration and flip angle 90°. The T/R switch and RF coil setup were tested using three different combinations of 1) the custom T/R switch with passive RF switch developed in-house, 2) the custom T/R switch that bypasses the high-power RF double-resonant passive switch, and 3) a commercial T/R switch (Clinical MR Solutions, LLC, Brookfield, WI, USA). The T/R switches were placed at the same position in all three cases. The raw data were processed using software developed in-house in the Python programming environment. The signal to noise ratio (SNR) of the ^{31}P RF coils for these three cases was calculated as the ratio of the peak intensity of the FID signal to the standard deviation of the noise.

3.4 Results

3.4.1 Bench Measurement

The isolation and insertion losses of the ^{31}P T/R switch, ^{1}H T/R switch, and the high-power passive RF switch, measured on the bench using the Vector Network analyzer, are listed in Table 3.1 and are shown in Figure 3.4. The isolation for the ^{31}P T/R switch was roughly -88 dB and for the ^{1}H T/R switch was approximately -49 dB during transmission. The isolation from the trap circuits was around -45 dB for both ^{1}H and ^{31}P frequencies. The insertion loss was less than -1.2 dB for the T/R switches and was less than -0.3 dB for the trap circuits. The switching time of the T/R switch was in the nanosecond range.

Table 3.1: Isolation and insertion loss of T/R switches and traps in dB unit.

	Transmit mode		Receive mode	
Circuit	Isolation (dB)	Insertion loss (dB)	Isolation (dB)	Insertion loss (dB)
^{1}H T/R switch	-49 (Tx-Rx)	-0.8 (Tx-coil)	-31 (Tx-Rx)	-0.7 (coil-Rx)
^{31}P T/R switch	-88 (Tx-Rx)	-1.0 (Tx-coil)	-83 (Tx-Rx)	-1.2 (coil-Rx)
^{1}H trap	-44 (^{1}H pulse)	-0.3 (^{31}P pulse)		
^{31}P trap	-46 (^{31}P pulse)	-0.1 (^{1}H pulse)		

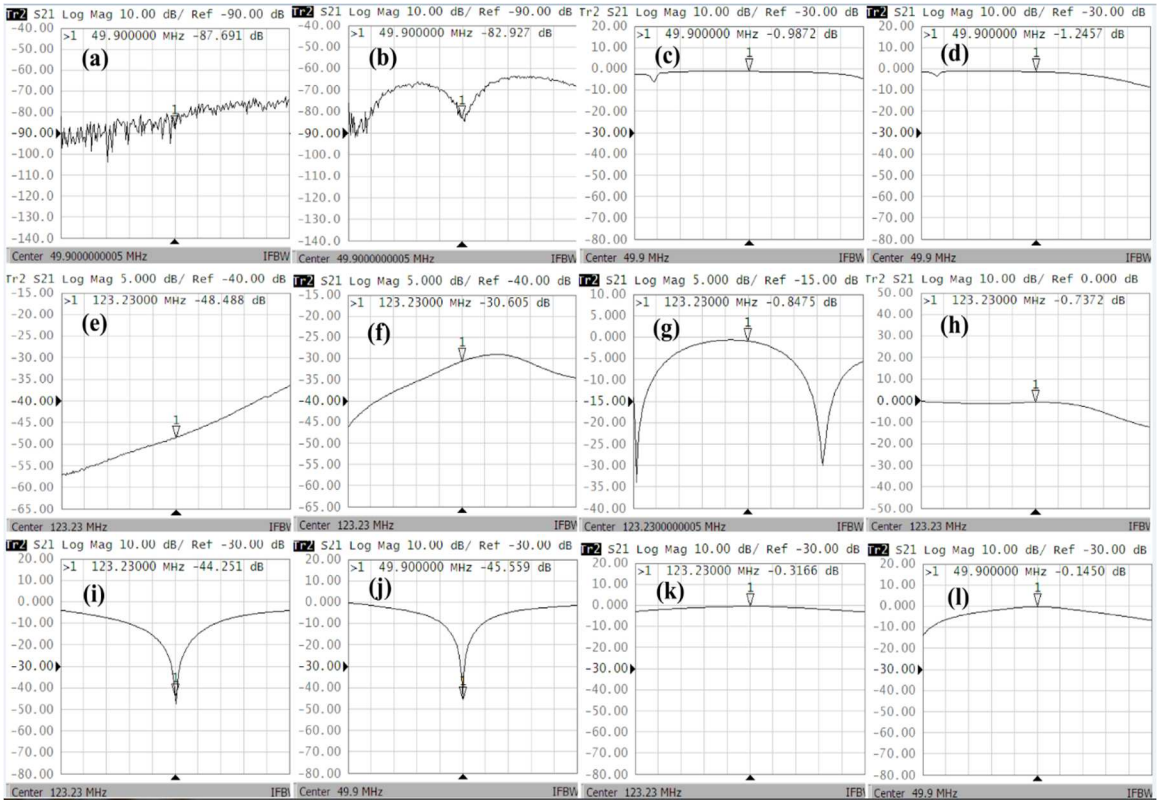

Figure 3.4: The isolation between Tx and Rx during (a) transmission, (b) reception, the insertion loss between (c) Tx and coil during transmission, and (d) coil and Rx during reception for the ^{31}P T/R switch. For the bench measurement, a splitter/combiner was used to combine two signals from the quadrature hybrid during transmission and to generate two signals that are out of phase by 90° from a single signal from the network analyzer during reception. The transmission refers to the state of the T/R switch where all PIN-diodes of the T/R switch are forward biased and the RF power is transmitted to the RF coil and the reception refers to the state in which all PIN-diodes are reverse biased and the NMR signal from the RF coil is routed to the receiver. The isolation for the ^{1}H T/R switch between Tx and Rx during (e) transmission, (f) reception, the insertion loss between (g) Tx and coil during transmission, and (h) coil and Rx during reception. The isolation of the (i) ^{1}H trap at the ^{1}H frequency, (j) ^{31}P trap at the ^{31}P frequency, the insertion loss of the (k)^{31}P trap at ^{1}H frequency, and (l) ^{1}H trap at the ^{31}P frequency.

3.4.2 MRI Experiments

The isolations of the ^{31}P quadrature and ^{1}H linear T/R switches are listed in Table 3.2. The linear relation for the voltage at the coil and Rx ports (not shown in the table) was observed at higher values of transmit gain. The isolation of the ^{1}H T/R switch for 50 Ω load on the coil port was -48 dB while that of ^{31}P T/R switch was -82 dB for a 50 Ω load on the coil port and -68 dB for the coil port connected to the ^{31}P quadrature coil.

Figure 3.5a shows the localizer image (sagittal) of water bag phantom (containing 23 PBS tablets dissolved in 250 mL distilled water) acquired with the ^{1}H RF coil of the $^{1}H/^{31}P$ double-tuned RF coil. Figures 3.5(b~d) are respectively the FIDs of the phantom obtained with the ^{31}P RF coil of the $^{1}H/^{31}P$ double-tuned RF coil and employing the custom-built T/R switch with high-power passive RF switch, custom T/R switch bypassing the high-power passive RF switch, and commercial T/R switch. The SNR were measured as 23.64, 23.83 and 18.36 from the phantom using the custom T/R switch with high-power passive RF switch, custom T/R switch with no high-power passive RF switch and commercial T/R switch, respectively. This gain is around 29% higher than that of the commercial T/R switch. Figures 3.5 (e~g) are the corresponding ^{31}P spectra. The baseline of the spectrum obtained from the commercial T/R switch is cleaner than that from the custom T/R switch.

Table 3.2: Isolation measurement of T/R switches under high power pulsed conditions.

T/R switch	Transmit gain (V)	Voltage at the coil port (V)	Voltage at Rx for 50 Ω at coil port (mV)	Voltage at Rx for coil conne-cted to coil port (mV)	Isolation for 50 Ω at coil port (dB)	Isolation for coil connected to coil port (dB)
^{1}H	50	1.9	7.9		-48	
^{31}P	50	13	1	5	-82	-68

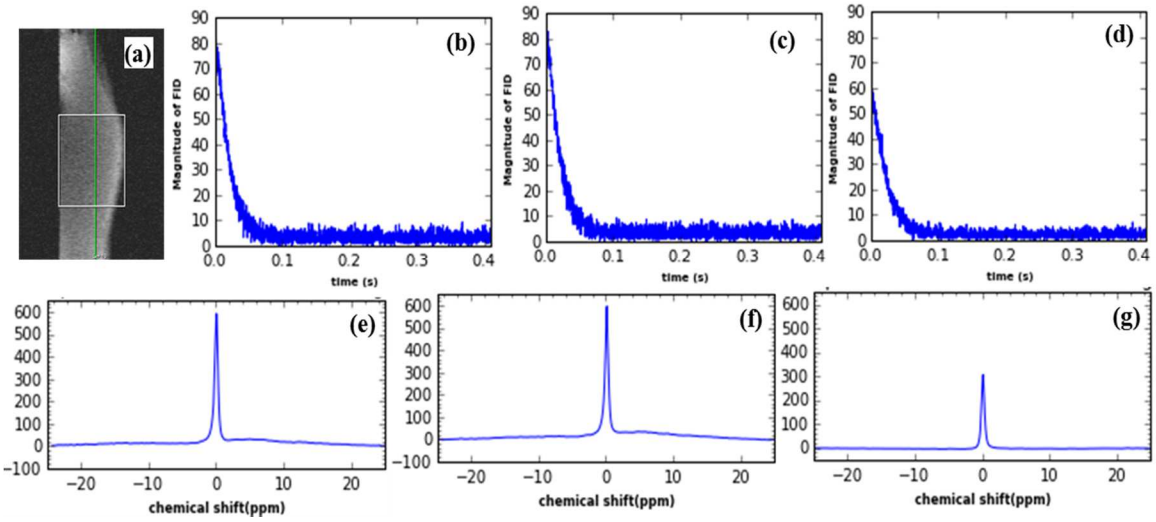

Figure 3.5: Scout image, ^{31}P FIDs, and spectra of a PBS phantom. (a) Scout image. FIDs obtained using the lamb ^{1}H/^{31}P RF coils with (b) home built T/R switch with high-power passive RF switch, (c) home-built T/R switch bypassing high-power passive RF switch, and (d) a commercial T/R switch. ^{31}P spectra obtained with home-built ^{1}H/^{31}P lamb RF coils and (e) home-built T/R switch with high-power passive RF switch (f) home-built T/R switch bypassing high-power passive RF switch, and (g) a commercial T/R switch. The gain in SNR obtained with home-built T/R switch is around 29% higher than that of the commercial T/R switch.

3.5 Discussion and Conclusions

This RF coil and T/R switch combination enabled us to perform ^{1}H/^{31}P dual nuclear MRI/MRS automatically without the need to physically move and replace either the RF coil or T/R switch during the experiment. The RF coil and T/R switch were made to optimize the SNR of the ^{31}P signal, while the ^{1}H channel was used for shimming and localization.

We designed and constructed a T/R and high power passive RF switches with high isolation, low insertion loss and high power handling capability to ensure their excellent performance (71), at a low cost and with minimum development time. The linear T/R switch has three-stage protection: Pi-network, quarter wave cable, and crossed-diodes before preamplifier. The quadrature T/R switch has four-stage protection:

shunt diode followed by parallel combination of inductor and 50 Ω resistor, Pi-network, quarter wave cable, and crossed-diodes for the preamplifier. The quadrature ^{31}P T/R switch provided higher isolation (~ -88 dB) than the linear ^{1}H T/R switch (~ -49 dB) on both bench measurement and under high power operating conditions (when 50 Ω load is connected to the coil port of the T/R switch) owing to the additional isolation introduced by the quadrature hybrid connected to the quadrature T/R switch. We observed a similar isolation for the ^{1}H quadrature T/R switch (not reported in the paper) to that of the ^{31}P quadrature T/R switch, which indicates a frequency independent isolation. A reduced isolation (-68 dB) was measured under pulsed conditions when a quadrature RF coil was connected to the coil port of quadrature T/R switch. This may be due to two reasons: i) some fraction of the transmit power is reflected due to slight variation of matching of the RF coil from 50 Ω in the MR environment and ii) power leakage during ring down of the RF coil entering into the receive path when the transmit pulse is turned off. Power is attenuated by the shunt diode followed by the parallel combination of an inductor and a 50 Ω resistor of the T/R switch and a crossed-diode pair. This isolation is still sufficient to protect the preamplifier. The high isolation between Tx and Rx ports during RF transmission ensures that RF power does not enter the receive pathway during the RF transmission. The high isolation during the signal reception insures that the MR signal from the RF coil is routed only to the receive pathway, and noise from the RF amplifier does not pass to the receiver.

Almost identical transmit gain and SNR of the phantom at a 3T magnetic field was obtained using the home-built ^{1}H/^{31}P RF coils and T/R switch with high-power passive RF switch and using the T/R switch that bypassed the high-power passive RF

switch, which confirms the losslessness of the high-power passive RF switch. There is around 29% gain in SNR for a double tuned $^{1}H/^{31}P$ RF coils with the home-built T/R switch compared with that using a commercial T/R switch. However, the baselines of the spectra measured using the custom T/R switch are little bit distorted, which may be caused by the magnetic components in the T/R switch.

T/R switch is RF coil and frequency specific (72). Moreover, most clinical RF coils have built-in T/R switches. This has previously restricted us to either designing a new RF coil compatible with the available T/R switches or purchasing a commercial T/R switch for each new application. Our T/R switch with a high-power RF switch design for the $^{1}H/^{31}P$ RF coils is flexible in that it can be easily modified to other frequency RF coils by changing the length of quarter wave cable and the components on the Pi-network section. This design can be easily employed to make linear, quadrature, double linear or double quadrature T/R switches for any MR active nuclei in a 3T magnetic field.

CHAPTER 4

QUANTITATIVE EVALUATION OF THE FIRST-ORDER CREATINE-KINASE REACTION RATE CONSTANT IN *IN VIVO* SHUNTED OVINE HEART TREATED WITH OXANDROLONE USING MAGNETIZATION TRANSFER ^{31}P MAGNETIC RESONANCE SPECTROSCOPY (MT-^{31}P-MRS) AND ^{1}H /^{31}P DOUBLE TUNED SURFACE RF COIL: A PRELIMINARY STUDY

This chapter is based on a manuscript entitled "Quantitative evaluation of the first-order creatine-kinase reaction rate constant in in vivo shunted ovine heart treated with oxandrolone using Magnetization Transfer ^{31}P Magnetic Resonance Spectroscopy (MT-^{31}P-MRS) and ^{1}H/^{31}P double tuned surface coil: A preliminary study" authored by Bijaya Thapa, Marjanna Dahl, Eugene Kholmovski, Phillip Burch, Deborah Frank, and Eun-Kee Jeong. The manuscript has been accepted in the journal Investigatve Magnetic Resonance Imaging (iMRI).

4.1 Abstract

Children born with single ventricle physiology have poor growth rate and malnutrition which lead to increased morbidity and mortality in this population. We assume that an anabolic steroid, oxandrolone, will promote growth in these infants by

improving myocardial energy utilization. The purpose of this paper is to study the efficacy of oxandrolone on myocardial energy consumption in these infants. We modeled single ventricle physiology in a lamb by prenatally shunting the aorta to the pulmonary artery and postnatally monitored cardiac energy utilization by quantitatively measuring the first-order reaction rate constant, k_f of the creatine-kinase reaction in the heart using magnetization transfer ^{31}P magnetic resonance spectroscopy, home built $^{1}H/^{31}P$ transmit/receive double tuned coil, and transmit/receive switch. We also performed cine MRI to study the structure and dynamic function of the myocardium and the left ventricular chamber. The spectroscopy data were processed using home developed python software while cine data were analyzed using Argus software. We quantitatively measured both the first-order reaction rate constant and ejection fraction in the control, shunted, and oxandrolone-treated lambs. Both k_f and ejection fraction of shunted lamb are found significantly reduced in shunted lamb than control lamb and they are increased in oxandrolone-treated lamb. Some improvement was observed in both the first-order reaction rate constant and ejection fraction for the lamb treated with oxandrolone in our preliminary study.

4.2 Introduction

Infants with single ventricle (SV) physiology account for a significant proportion of child healthcare resources, but tools for efficient comparison of new or even standard treatment strategies are lacking. Multiple specific types of congenital cardiac malformations result in single ventricle physiology including hypoplastic left heart syndrome and tricuspid atresia. The vast majority of SV infants require a series of two to

three palliative surgeries (Fontan) (73) because the heart cannot be surgically corrected in ways to allow for normal cardiac physiology. SV infants have a mortality rate of approximately 25% in the first year of life and survivors experience significant lifetime morbidity. Children with even excellent technical repairs may slowly deteriorate in the postoperative period from multiple causes, including wound infections, prolonged effusions, prolonged mechanical ventilation and venous thrombosis. Growth failure and malnutrition are common to virtually all of these complications in this population (74), and poor growth is associated with increased morbidity and mortality (75). The growth failure in SV infants may be due to high cardiac energy requirements from their shunt dependent physiology (76,77). The growth has been difficult to modify and simply increasing calories or changing the method of feeding has not proven uniformly successful (78). We hypothesize that an anabolic steroid, oxandrolone, will promote growth in SV infants by improving myocardial energy utilization.

Oxandrolone is approved to promote growth in children with extensive surgery, severe trauma or burns, chronic infections, constitutional growth delay, and Turner's syndrome (79–82). The most extensive experience with oxandrolone is in pediatric burn patients, (83–85) in whom oxandrolone has been safely administered for 1 year with beneficial effects on lean body mass and bone mineral content identifiable 5 years post-treatment (80). Echocardiographic evaluation in this study suggests more efficient myocardial energy usage in patients on oxandrolone compared to placebo at the completion of therapy and 1 year following completion (80). Oxandrolone as a therapy to improve metabolic efficiency has not been implemented in the treatment of either newborn infants or patients with congenital heart defects (CHD).

To investigate the effects of oxandrolone on myocardial energy consumption in the SV infants, we developed a neonatal animal model in which SV physiology was mimicked in a lamb by prenatally shunting the aorta to the pulmonary artery (86). Sheep are the species of choice for development of this model because newborn lambs are of similar size (3-5 kg) to human newborns, pregnant ewes typically carry 1-3 fetuses per pregnancy, and both ewes and fetuses are tolerant of surgical intervention. After birth the lambs were treated with oxandrolone for the first month of life. The change in myocardial energy utilization with oxandrolone treatment of the lambs was determined by measuring the first-order reaction rate (k_f) of the creatine-kinase (CK) reaction in the heart using magnetization transfer ^{31}P-MR spectroscopy (MT-^{31}P-MRS). We also performed cine MRI on the lamb to study the structure and dynamic function of myocardium and the loading of the left ventricle by evaluating end diastolic volume (EDV), end systolic volume (ESV), stroke volume (SV) and ejection fraction (EF).

^{31}P spectroscopy allows noninvasive monitoring of phosphorous metabolites and is being investigated as a tool to interrogate the bioenergetics in both health and disease of many bodily organs (87). Several ^{31}P MRS techniques such as conventional saturation-transfer MRS (ST MRS) (88), four-angle ST (FAST) (89), three acquisition ST (novel strategy method) (90), triple repetition time ST (TRiST) (91), two repetition time ST (TwiST) (92), time-dependent ST (TDST) (93) Bloch-Siegert four angle ST (BOAST) (94) have been employed to evaluate pseudo first-order rate constant of creatine-kinase reaction in human and animal heart. In the present work we adapted three acquisition ST methodology in one-dimensional MT-^{31}P-CSI pulse sequence to study the myocardial energy metabolism in animal models of congenital cardiac malformations.

4.2.1 Theory

The CK reaction is essential for the buffering and rapid regeneration of adenosine triphosphate (ATP) in heart tissue (93). The heart uses this energy to contract. The CK enzyme catalyzes the reaction, in which the exchange of phosphate between ATP and phosphocreatine (PCr) takes place according to the reaction:

$$\mathrm{PCr^{2-}} + \mathrm{ADP^{-}} + \mathrm{H^{+}} \rightleftarrows \mathrm{Cr} + \mathrm{ATP^{2-}} \quad [4.1]$$

The reaction proceeds in both the forward and reverse directions with k_f and k_r as the pseudo first-order forward and reverse rate constants, respectively. One approach to quantify k_f is to saturate γ-ATP so that the reverse reaction brings no magnetization from ϒ-ATP to PCr. In MT-^{31}P-MRS, a train of sinc RF pulses with a narrow bandwidth (75 Hz) is applied to saturate γ-ATP line. The rate equation of longitudinal magnetization of PCr during these saturation pulses is given by modified Bloch equation:

$$\frac{dM_{PCr}(t)}{dt} = \frac{M^{o}_{PCr}(t) - M_{PCr}(t)}{T_1} - k_f M_{PCr}(t). \quad [4.2]$$

The detailed solution of Eq. 4.2 can be found elsewhere (95–97). The expression of k_f obtained by solving this first-order differential equation can be written as:

$$k_f = R'_1\left(1 - \frac{M^{PCr}_{SS}}{M^{o}_{PCr}}\right), \quad [4.3]$$

where the apparent relaxation rate, R'_1 measured using γ-ATP saturated is given by the following expression:

$$R'_1 = R_1 + k_f = \frac{1}{TR} ln\left(1 - \frac{M^{PCr}_{TR}}{M^{PCr}_{SS}}\right), \quad [4.4]$$

where, M^{PCr}_{TR} is the PCr magnetization obtained with a short TR and continuous saturation pulses at γ-ATP and $R_1 = 1/T_1$ is the intrinsic relaxation rate.

Since ϒ-ATP is separated from PCr only by 2.5 ppm, which is about 125 Hz at

3T, the RF pulse used to selectively saturate ϒ-ATP also partially saturates PCr peak. The rate equation of longitudinal magnetization of PCr incorporating the RF bleed-over effect in the CK reaction is given by the modified Bloch equation (98):

$$\frac{dM_{PCr}(t)}{dt} = \frac{M^{o}_{PCr}(t) - M_{PCr}(t)}{T_1} - k_f M_{PCr}(t) - \eta M_{PCr}(t). \quad [4.5]$$

Here, η is the rate of loss of PCr magnetization due to an RF saturation pulse. The value of η can be estimated by measuring the PCr magnetizations with saturation pulse irradiated at +2.5 ppm and +20 ppm on the opposite side of ϒ-ATP. The expression of RF bleed-over obtained by solving Eq. 4.5 can be written as:

$$\eta = \frac{R_1'' M_{ss}^{PCr}}{M_o}\left(\frac{M_o}{M_o'} - 1\right), \quad [4.6]$$

where M_o' and M_o are the thermal equilibrium magnetization with saturation pulse irradiated at +2.5 ppm and +20 ppm, respectively and $R_1'' = R_1 + k_f + \eta$.

4.3 Methods

4.3.1 Animal Model

Both timed pregnant ewe that preferably carried twins/triplets and the fetuses were anesthetized at approximately 140 days of gestation (term gestation 145 days) for the surgical procedure. The ewe had an abdominal incision, and then a uterine incision to allow exposure of the left forelimb and chest of the fetus. A left lateral thoracotomy was performed on the fetus and a 2 mm length of 8.0 mm diameter Gore-Tex vascular graft (a gift of W. L. Gore & Associates, Inc) was interposed between the ascending aorta and main pulmonary artery. All incisions were closed, and the ewe was recovered from anesthesia. Antibiotics were given intraoperatively and daily to the ewe until 2 days after delivery. Lambs were allowed to deliver spontaneously, and were cared for by the ewe

until approximately 1 month of age when MR studies were performed. The lambs rejected by the mother were bottle fed. Unoperated twins of the shunted lambs served as controls. Four groups of total 9 lambs (~2 lambs per group): control (n = 3), shunted (n = 2), oxandrolone–treated (ox-treated) control (n = 2), ox-treated shunt (n = 2) were created. The ox-treated animals were given 0.1 mg/kg orally twice daily beginning on day of life 2. All animal work was performed under a protocol approved by the local IACUC and euthanasia was performed in accordance with AVMA requirements.

4.3.2 Pulse Sequence

Siemens' product pulse sequence, CSI-FID was modified to implement one-dimensional MT-^{31}P -CSI pulse sequence by adding outer-volume-suppression (OVS) pulses with user-selectable number of iterations, adiabatic-half-passage (AHP) RF pulse for excitation, a train of narrowband RF pulses to saturate ϒ-ATP, and 1D CSI with correct localization to the existing functionalities using the pulse sequence development environment software (IDEA, Siemens Medical Solutions, Erlangen, Germany). The schematic timing diagram of MT-^{31}P-CSI is shown in Figure 4.1.

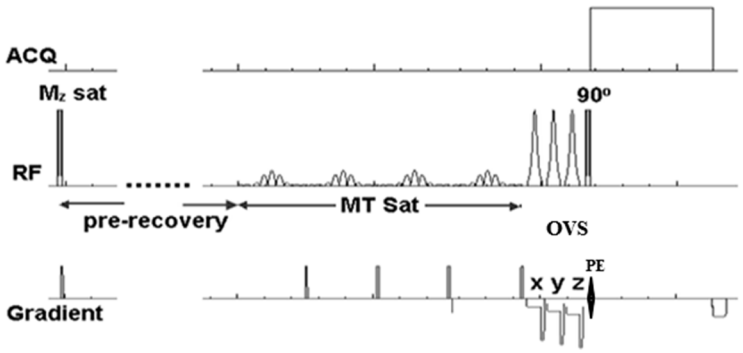

Figure 4.1: Timing diagram of pulse sequence, 1D MT-CSI.

The 1D MT-CSI protocol for the lamb's heart is detailed in Table 4.1. Three hard pulses of 400 μs duration and a flip angle of 110° followed by a spoiling gradient were applied to null the longitudinal magnetizations of all metabolites. A sinc RF pulse with bandwidth 75 Hz and flip angle 300° was used as a MT saturation pulse to saturate the γ-ATP for the duration t_{sat} by repetitive application so that the reverse transfer of magnetization from γ-ATP to PCr could not proceed. Six OVS pulses and gradients were applied to prevent the contamination on the ^{31}P signal of the heart from the ^{31}P signal of the chest muscle. An AHP pulse of bandwidth 4 kHz was used for excitation.

4.3.3 Hardware

Most clinical MR systems have a single RF transmit port for both ^{1}H and X-nuclei frequencies. An additional circuitry is required to automatically direct the ^{1}H RF pulse to the ^{1}H T/R switch and the X-nuclei RF pulse to the X-nuclei T/R switch. For this, we made a high power RF switch that is positioned prior to the ^{1}H and ^{31}P TR switches as shown in Figure 4.2 for the automatic switching of the RF pulses to either the ^{1}H or ^{31}P TR switch for ^{1}H MRI or ^{31}P MRS, respectively.

Table 4.1: The 1D MT-CSI protocol for the lamb's heart

	Δf_{MT} (ppm)	**TR (s)**	**N_{MzSat}**	**t_{preSat} (s)**	**t_{MT} (s)**
$\mathbf{M_o^{PCr}}$	0	20	0	0	0
$\mathbf{M_{PCr}^{SS}}$	-2.7	minimum	0	2.5	3.5
$\mathbf{M_{PCr}^{Tsat}}$	-2.7	minimum	2	0	2

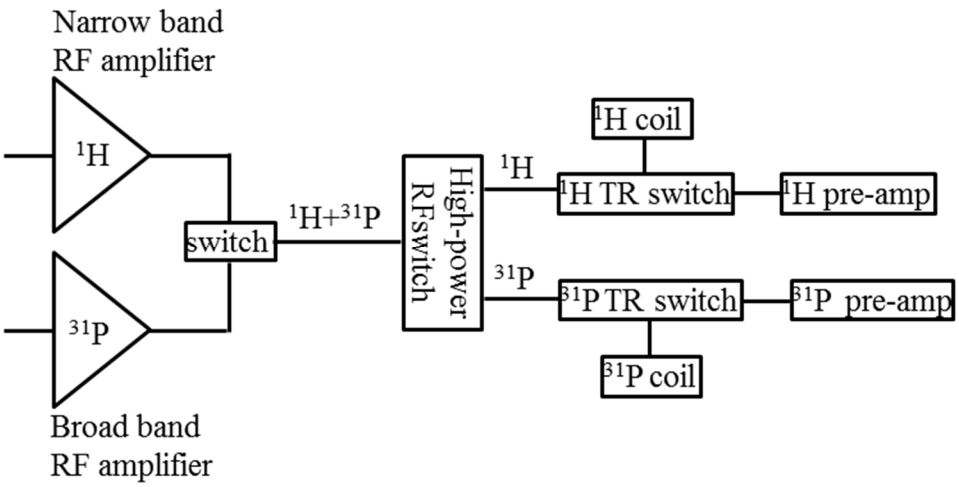

Figure 4.2: Block diagram of hardware.

4.3.3.1 $^{1}H/^{31}P$ Dual-Tuned RF coils

Due to a low concentration and relatively small gyromagnetic ratio of ^{31}P in human and animal tissue compared to protons (52,99), a dedicated ^{31}P coil optimized for the ^{31}P nucleus accompanied by a ^{1}H coil for the scout imaging and shimming of the region of interest is required. We built a quadrature ^{31}P coil with dimensions optimized to the heart of lambs aged 4 to 6 weeks and a relatively large ^{1}H linear coil. The detailed explanation for the construction of the coil is given in the author's previous paper (100). The ^{31}P coil consisted of a butterfly loop decoupled with a rectangular loop for a quadrature mode as shown in Figure 3.1 by adjusting the overlapping region of the coils. The ^{1}H RF coil that surrounded the ^{31}P coil as shown in the Figure 3.1 was positioned such that it is decoupled with the ^{31}P butterfly coil for quadrature mode. The coupling between the ^{1}H and ^{31}P rectangular coil was minimized by choosing the large dimension of the ^{1}H coil compared to the rectangular coil. The loaded isolation between the ^{1}H and ^{31}P butterfly coils measured using vector network analyzer (E5061B ENA Series, Agilent

Technologies, Englewood, Colorado, USA) and 250 mL saline bag phantom at the ^{1}H frequency was -23.2 dB and that at the ^{31}P frequency was -28.7 dB while that between the ^{1}H and ^{31}P rectangular coils at the ^{1}H frequency was -22.8 dB and at the ^{31}P frequency was -26.7 dB. Moreover, the ^{31}P coil affects the ^{1}H SNR far more than the ^{1}H coil affects the ^{31}P SNR (101). This is because ^{31}P coils have relatively high capacitor values compared to the ^{1}H coil which provides low impedance at the ^{1}H frequency (53). The isolation between the ^{1}H and ^{31}P RF coils at ^{1}H frequency could be further increased by inserting the^{1}H traps at the ^{31}P coils with a little compromise of the ^{31}P signal. No extra lossy components on the ^{31}P coil were added so that the performance of the ^{31}P coil is the same as the same coil on the same frame without ^{1}H coil. The separate coil design for each nucleus allows us to independently match and tune the ^{1}H and ^{31}P coils.

4.3.3.2 T/R and High Power RF Switches

The T/R circuitry for our $^{1}H/^{31}P$ dual-tuned transmit-receive lamb RF coil consists of a linear T/R switch for the linear ^{1}H RF coil and a quadrature T/R switch for the quadrature ^{31}P RF coil with high-power passive RF switch (100,102) consisting of two trap circuits placed prior to the T/R switches to automatically direct the ^{1}H RF pulse to the ^{1}H T/R switch during ^{1}H MRI and the ^{31}P RF pulse to the ^{31}P T/R switch during ^{31}P MRS.

4.3.4 MRI Experiments

MT-^{31}P-MRS experiments were carried out on 9 lambs aged 4 to 6 weeks and in four groups: control (n=3), ox-treated control (n=2), shunted (n=2) and ox-treated

shunted (n=2), using the custom built $^{1}H/^{31}P$ double tuned surface transmit/receive coil and $^{1}H/^{31}P$ T/R switch described above on a 3T clinical MRI system (Tim-Trio, Siemens Medical Solutions, Erlangen, Germany). Lambs were anesthetized with 2% isoflurane mixed with oxygen throughout the experiment. The heart rate was monitored using an MR Monitoring System (Medrad Veris model 8600, Medrad Inc. One Medrad Drive Indianola, PA 15051). The RF coils were matched and tuned with the lamb in the scanner using portable RF sweeper probe tuner (405NV+, Morris Instruments Inc., Ottawa, Ont., Canada).

^{1}H MR anatomical images were first acquired using ^{1}H RF coil of the $^{1}H/^{31P}$ RF coil with the lamb in the scanner in a feet first left lateral position to determine the position of RF coils using the localizer. The ^{1}H image of the small bead containing ^{1}H attached to the center of the $^{1}H/^{31}P$ RF coil was used to adjust the RF coil at the position of heart. The ovine heart was then shimmed to homogenize the B_o field over the region of heart. Cardiac-triggered, 1D CSI with eight phase encodes and saturation bands on the chest to minimize contamination from the chest muscle were used for ^{31}P spectroscopy. Three experiments were carried out to measure k_f. M^{o}_{PCr} was obtained using TR=20 sec with no MT and M_z saturation pulses, M^{TR}_{PCr} using three hard RF pulses with flip angle 300˚ as M_z saturation RF and a spoiling gradient pulses followed by MT saturation pulses at -2.7 ppm away from PCr (i.e., at the position of γ-ATP) for 2 sec, and M^{ss}_{PCr} was measured with presaturation delay of 2.1 sec and MT saturation at -2.7 ppm for 3.5 sec (90). The total scan time for measuringM^{o}_{PCr}, M^{ss}_{PCr}, and M^{TR}_{PCr} was 37 minutes 40 sec. The value of rate of loss of PCr peak due to RF bleed-over effect was obtained by measuring M_o and M'_o and using Eq. (4.6). The thermal equilibrium magnetization, M'_o

under RF bleed-over was measured by irradiating saturation RF pulses at +2.5 ppm for t_{sat}=20 sec. The same experiment was repeated to measure thermal equilibrium magnetization, M_o without RF bleed-over effect by irradiating saturation RF pulses at +20 ppm (98). The rate of loss of magnetization of γ-ATP due to MT saturation pulse, η was then computed using Eq. 4.6. All experiments were performed with a receiver bandwidth of 2.5 kHz and 512 data points.

Only 4 out of 9 lambs: one from each group of control, shunted, ox-treated control, and ox-treated shunted lambs underwent cine MRI after ^{31}P MRS using Siemens' coil (Flex large 4, a 3T Tim) as a receiver and the body coil as a transmitter. Both long axis and short axis scout images were acquired for planning short axis cine images. Cine images covering the whole heart in short axis orientation were acquired using TRUFI (true fast imaging with steady state free precession) pulse sequence with retrospective electrocardiographic (ECG) gating. The imaging parameters were: typical field of view (FOV) = 260 X 142 mm^2, typical matrix size 208x114, in-plane resolution = 1.25 X 1.25 mm^2, contiguous stack of slices of 6 mm thickness, TE/TR= 1.48 ms/3.4 ms, flip angle = 40°, and temporal resolution = 23.6 ms.

The raw ^{31}P MRS data were processed using home-developed processing software in Python language that performs 10 Hz Gaussian and Lorentzian broadening, zero filling to 4-k of data points, fast Fourier transformation, and interactive zeroth and first-order phase correction. The magnetization of PCr and ATP in myocardium was measured as the area under the respective resonance peaks. The cine data were processed manually using Argus software (Siemens Healthcare) to calculate end diastolic volume (EDV), end systolic volume (ESV), stroke volume (SV) and ejection fraction (EF). Papillary muscles

were excluded.

4.4 Results

Figure 4.4a shows an example of localizer image with 1D CSI grid (white) and green rectangle as shim region of *in vivo* lamb's heart obtained with the custom made $^{1}H/^{31}P$ double tuned transmit-receive RF coils. Figures 4.4(b~e) are the stacked plots of representative ^{31}P MR spectra from control (triplet), shunted (triplet), ox-treated shunted (doublet), and ox-treated control (doublet) lambs, respectively. The PCr peaks in blue, green and red spectra indicate M^{o}_{PCr} M^{ss}_{PCr}, and M^{TR}_{PCr}, respectively, that are needed to calculate the k_f. The values of k_f and SNR of the M^{o}_{PCr} peak obtained from these spectra and EDV, ESV, SV, and EF obtained from the cine MRI data are listed in Table 4.2. The low value of SNR of M^{o}_{PCr} indicates the poor shimming compared to the higher value. The k_f of the triplet shunted lamb is 0.09 sec^{-1} which is much smaller than either of the control lambs (0.22 sec^{-1} or 0.28 sec^{-1}) of the same set of triplet lambs. The k_f of the ox-treated shunted lamb of the last doublet is 0.30 sec^{-1} which demonstrates the increase of k_f with oxandrolone treatment towards the normal or its ox-treated control doublet (k_f = 0.31 sec^{-1}).

Figure 4.4f is the spectra for computing the rate of loss of PCr magnetization, η due to RF bleed-over effect where blue (MT saturation pulses at 2.5 ppm applied for 20 sec) and green spectra (MT pulses at 20 ppm applied for 20 sec) are with and without RF bleed-over effect, respectively. The peak height of PCr with RF bleed-over can be seen clearly decreased compared to that without RF bleed-over effect. The value of η was found to be 2.8%. The low value of η indicates that PCr, peak is not noticeably affected

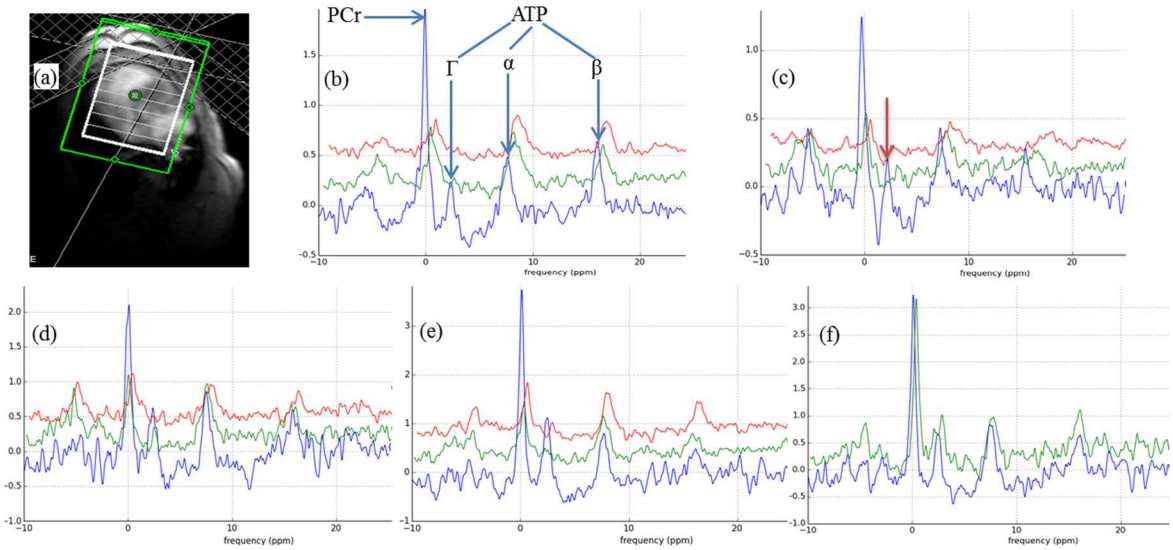

Figure 4.4: Scout image and ^{31}P spectra obtained with the home-built T/R switch and lamb RF coil. (a) A scout image with 1D CSI grid with green rectangle as a shim region. Saturation bands were used on the chest wall to avoid the contamination on the ^{31}P signal of heart from the chest wall. (b-e) *In vivo* stacked plots of ^{31}P MR spectra of control (triplet), shunted (twin), and ox-treated control (twin) lamb. Blue, green and red spectra indicate M^{o}_{PCr} (equilibrium), M^{ss}_{PCr} (saturation pulse for 3.5 sec and presaturation time of 2.5 sec), and M^{TR}_{PCr} (saturation pulse for 2 sec), respectively. The arrows indicate the positions where saturation pulse is applied. (f) ^{31}P spectra with (green) and without (blue) RF bleed-over effect. There is decrease in PCr peak due to RF bleed-over effect.

Table 4.2: k_f, SNR of $\mathbf{M_0^{PCr}}$, End Diastolic Volume (EDV), End Systolic Volume (ESV), Systolic Volume (SV), and Ejection Fraction (EF) of different groups of lambs.

Lamb Type	Lamb	K_f (s^{-1})	SNR (M_o^{PCr})	EDV (mL)	ESV (mL)	SV (mL)	EF (%)
Triplet	Control	0.22	49.75	31.0	16.4	14.6	47.2
(~ 4 weeks)	Shunted	0.09	25.0				
	control	0.28	23.75				
Twin	control	0.36	71.0				
(~8 weeks)	shunted	0.28	67.0	103.2	69.0	34.2	31.3
Single	Ox-treated shunt	0.32	37.7				
(~4 weeks)							
Twin	Ox-treated control	0.15	34.7				
(~6 weeks)	Shunted stillborn	-					
Twin	Ox-treated control	0.31	56.6	48.6	25.2	23.4	48.1
(~5 weeks)	Ox-treated shunt	0.30	30.5	100.5	62.5	38.0	37.8

by the MT pulses, so we did not take RF bleed-over effect into consideration while calculating k_f.

Figure 4.5 illustrates an example of the short axis images of a shunted lamb heart with red contours placed on endocardial myocardial boarders of the left ventricle from base to apex on all slices pertaining to a) end diastole and b) end systole. Papillary muscles were excluded from the contours. Similar contours were drawn for other lambs' heart (not shown in Figure) to calculate left ventricular (LV) parameters. The EF of controlled, shunted, ox-treated control, and ox-treated shunt were 47.2%, 31.3%, 48.1%, and 37.8%, respectively. The EDV of the shunted (103.2 mL) or ox-treated shunted lamb (100.5 mL) is 2- 3 times larger than EDV of either the control (31 mL) or the ox-treated control lamb (48.6 mL), which is consistent with our goal of generating a volume overloaded heart.

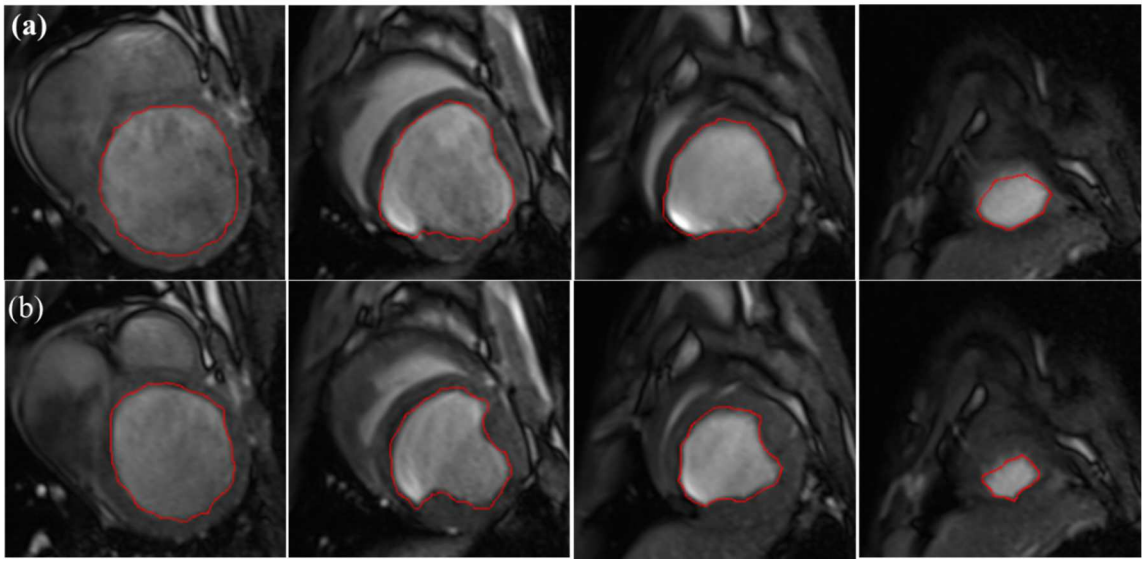

Figure 4.5. Representative short axis images of shunted lamb with (a) diastolic and (b) systolic contours (red) drawn using Argus software.

4.5 Discussion and Conclusions

The RF coil and T/R switches were developed to optimize the SNR of the ^{31}P signal and enable $^{1}H/^{31}P$ dual nuclear MRI/S automatically without the need to physically move and replace either the RF coil or T/R switch during the experiment. We implemented MT saturation technique in 1D CSI pulse sequence to measure k_f in different groups of ovine hearts mentioned above at 3T. An AHP pulse was used to generate a uniform excitation over the region of interest using the quadrature ^{31}P surface coil.

This study is the first to measure k_f and cardiac volume in surgically created SV and ox-treated lambs. We studied oxandrolone's effect on myocardial energetics and function not because it's a new drug but because we are proposing a novel use for it in treating growth failure in SV infants. The k_f of the *in vivo* ovine heart was measured using novel strategy method (90) with drastically shorter total data acquisition time compared to the conventional approach which requires progressive saturation experiments with long pre and MT saturation times to evaluate M_{PCr}^{ss} and R_1'. The PCr peak in blue spectra in Fig 4.5(b-e) for measuring M_{PCr}^{o} was reduced in green spectra for measuring M_{PCr}^{ss} due to the application of the MT pulses at the position of γ-ATP peak at 2.5 ppm away from PCr peak to suppress reverse transfer of magnetization from γ-ATP to PCr for 3.5 sec and even further reduced in red spectra for measuring M_{PCr}^{TR} due to short TR and MT saturation pulses (applied for 2 sec) used in this acquisition.

It is fairly reasonable to compare the k_f values between the lambs of the same twin or triplet. The values of k_f obtained from our results show that, compared with the control heart of the same twins/triplets, the forward reaction rate constant of CK reaction

is significantly lower in the shunted heart and it is increased in the ox-treated heart compared to the shunted heart which may indicate the increase in the rate of energy production in the ox-treated lamb. This result is consistent with the previous studies on *in vivo* human heart which reported substantial decrease in k_f in failing hypertrophic myocardium compared to healthy myocardium (103–105) and on a 7-month-old isolated cardiomyopathic hamster heart which showed an increase in the CK flux with enalapril-treatment (106). The value of k_f for the shunted or control heart of the triplets is smaller than that in the twins. The value of k_f for the control and ox-treated control lamb of the last twins of Table 4.2 is approximately the same as expected. The k_f values of shunted and control lambs of one twin or triplet is different from another twin or triplet lambs. This may be due to several reasons. The triplet shunt may not get enough nutrients as the twin shunt does before and after its birth. Those lambs which are rejected by the sheep after birth were bottle fed. One lamb may be much sicker than the other. The triplet shunt was scanned when it was ~ 1 month old and the twin shunt was scanned when it was ~ 2 months old. Chesky et al. (107) from the ^{31}P MRS on the male Fischer rat have shown that the myocardial creatine phosphokinase activity rises from 1 month of age to a maximum 2 months of age. There may not be the same experimental situation for the lambs though we tried hard to be the same as they were scanned on different dates.

Several methods such as cardiovascular ultrasound (108), angiocardiography (109), and computed tomography (110) have been used to quantitatively evaluate the ESV, EDV, SV, and EF of the left ventricle. These methods have certain limitations and demerits. For instance computed tomography is carcinogenic to the patient, the cardiovascular ultrasound method requires geometric premises etc. As an alternative to

these methods, cardiac MRI is a noninvasive method that has been frequently used as a standard tool for the cardiac volume measurements (111,112). In the present study, we used cine MRI for the volume measurements of *in vivo* ovine heart. The cine MRI measurement of the ovine heart shows that EF of control lamb is greater than that of the shunted heart and is similar to that of the ox-treated control lamb. There is some improvement of EF with oxandrolone treatment as expected. The EDV and ESV of ox-treated shunt are greater than that of the ox-treated control, which indicates the greater remodeling in the ventricle of the shunted lamb. Further studies on more lambs with and without surgically created SV physiology are needed for proper statistical analyses to confirm these findings.

CHAPTER 5

ULTRA-HIGH-b RADIAL DIFFUSION WEIGHTED IMAGING (UHb-rDWI) SIGNAL BEHAVIOR IN DIFFERENT TRACTS OF THE CERVICAL SPINAL CORD

This chapter is based on two manuscripts entitled "Ultra-high-b radial diffusion weighted imaging (UHb-rDWI) of the human cervical spinal cord" and "Ultra-High-b diffusion imaging of cervical spinal cord in multiple sclerosis" authored by Bijaya Thapa, Nabraj Sapkota, YouJung Lee, EunJu Kim, John Rose, Lubdha M Shah, and Eun-Kee Jeong. The manuscripts have been submitted to Neuroimage.

5.1 Abstract

This study sought to improve imaging of the cervical spinal cord (CSC) with quantitation of spinal cord injury using novel ultra-high-b DWI (UHB-DWI) in four subjects and two Multiple Sclerosis (MS) patients with new acute CSC lesions. Serial imaging was performed to demonstrate the stability and reproducibility of the method and quantitation of combined demyelination and axonal injury in evolving MS lesions. Using T2WI for planning, cross-sectional high-b diffusion images with b values ranging from 573 to 7348 s/mm^2 were acquired using 2D Singleshot Diffusion-Weighted Stimulated EPI with Reduced FOV (2D ss-STEPI-rFOV) and a CSC dedicated 8-channel array coil.

An additional b_0 image without diffusion gradient was obtained for correcting T_1 decay during the mixing time TM (time interval between 2nd and 3rd 90° RF pulses). The signal-b curve at various levels of healthy CSC shows the biexponential decay behavior, i.e., fast exponential decay at lower b-values and much slower decay at high b region (b > 4,000 s/mm^2). UHb-rDWI signal-b curves of the normal control were consistent on two successive measurements, demonstrating the reproducibility of this technique. While MS lesions revealed a marked decrease in signal intensities even at UHb-values most likely reflecting demyelination, the unaffected regions of the MS patients were similar to those in the normal control. The UHb-rDWI signal intensity of the lesions increased on serial observations over a 6-month duration, approaching increased myelination curves, concordant with improvement in the patient's clinical status which illustrates this technique's potential to detect the evolution of demyelinating lesions with axonal sparing and remyelination.

5.2 Introduction

Injury in the spinal cord may include local demyelination and/or axonal damage (113) and leads to varying degrees of neurologic deficit, which can cause persistent disability in the patient. Despite the superb contrast and spatial resolution provided by magnetic resonance imaging (MRI), conventional MRI, such as T_1- and T_2 weighted imaging, are limited in their ability to detect the very early stage of the spinal cord disease when clinical symptoms may be vague (113–116). Therefore, a noninvasive imaging biomarker for earlier disease detection, and for monitoring disease evolution, and treatment would be a significant advancement in the care of patients with injuries of

the spinal cord.

Diffusion tensor imaging (DTI) is considered to be a promising method to evaluate white-matter integrity and pathology. Quantitative DTI metrics, such as radial and axial diffusivities, and fractional anisotropy (FA) (117), may serve as biomarkers for the demyelination and axonal loss in the spinal cord diseases. Unlike the brain where overlapping of crossing fibers in multiple orientations requires DW signal measurement along many different directions to compute DTI metrics, for the spinal cord in which nerve fibers are one-dimensional and the principal direction of local symmetry is along the cord direction, DW signal measurements along the directions perpendicular and parallel to the nerve fiber are sufficient. Unfortunately, these measurements using the conventional DTI are limited with respect to the specific details of neuropathology and microstructural architecture and are not always consistent in detecting the axonal dysfunction (7,8,36,118). For instance, the decreased FA assessed with DTI for the spinal cord lesion cannot distinguish whether it is caused by increased water content in the extra axonal (EA) space (edema) or by increased water exchange between intra-axonal (IA) and EA spaces due to demyelination or by both. Also, the measured radial diffusivity is not objective, but dependent on b-values because of different signal contributions from IA and EA spaces at different b-values.

Unlike the brain, MR imaging of CSC is technically challenging because of the small cross-sectional area, susceptibility artifact due to cord-vertebral bone interface, chemical-shift artifact arising from the fat in the vertebral bones and other nearby structures, and motion induced artifact resulting from cerebrospinal fluid (CSF) pulsation, breathing, swallowing during the measurement (119–121). The variant magnetic

susceptibility artifact particularly limits the capability of diffusion-MRI (DWI, DTI) of CSC using 2D single-shot diffusion-weighted EPI (2D ss-DWEPI), which is commonly used for the brain.

While the conventional DTI measures and evaluates the DWI at low-b region, where the extra-axonal water dominates the signal behavior, ultra-high-b DWI provides better contrast between white-matter (WM) and gray-matter (GM) with greater diffusion weighted and less T_2 weighted effect (38). A pair of strong diffusion gradients, separated by a long diffusion time, sensitizes the water exchange effect (15), which is predicted by a Monte-Carlo simulation (MCS) of water diffusion MRI in one-dimensional white-matter (122). This technique produces DW images with greatly reduced: a) geometric distortion, which is caused by susceptibility difference at/near the interface between bone/tissue and common in EPI-type acquisition, by implementing reduced field of view (FOV) in the phase encoding direction (12,13), b) the motion induced artifact using single shot acquisition, and c) acquisition time by acquiring multiple slices within a single repetition time (TR) thereby making the sequence amenable for clinical purpose.

The radial diffusivity, i.e., diffusivity perpendicular to the cord depends strongly on b-value and relative concertation of IA and EA spaces. Because of long echotime TE in clinical MRI system due to the limited gradient strength, say larger than 50 ms for $b > 500$ s/mm^2, the signal from the myelin water, of which T_2 is short (< 10 ms), is mostly suppressed to noise-level. Therefore, no matter how heterogeneous the physical environment is inside the CSC white-matter, for the "radial DWI," we may compartmentalize the WM into, 1) water molecule "*restricted*" in IA space by myelin sheath where water cannot move more than an inner diameter of the axon (~1.2 μm)

(123), and 2) "*mobile*" water in EA space where water can move over the hindered boundaries including the membranes. Our previous finding based on MCS (122) demonstrated that the rDWI signal from the EA space of healthy CSC decays with increasing b-values and drops to background noise level in ultra-high-b (UHb) region (b > ~ 4,000 s/mm^2 at clinical MRI system) while that from the IA space remains constant in UHb region. Thus, at UHb region and for healthy cord, if there is no exchange of water molecules between IA and EA spaces, the signal intensity measured is solely from IA space. In the case of a demyelinated axon such as in multiple sclerosis (MS) patients, which permits water to exchange between IA and EA spaces, the rDWI signal from IA space decays at UHb values. Once the EA signal is filtered out with UHb diffusion gradient, we can quantify the high-b decay constant (D_H) of water molecules in the cord by fitting UHb-rDWI signal to an exponential decay function which may be used to characterize many white-matter diseases (39,124). The measured rDWI signal intensity which is the contribution from IA and EA spaces can be expressed as

$$S_r(b) = S_{EA}^0 e^{-bD_L} + S_{IA}^0 e^{-bD_H}, \qquad [5.1]$$

where D_L and D_H are, respectively low- and high–b decay constants and S_{EA}^0 and S_{IA}^0 are EA and IA signal intensities without diffusion decay, respectively.

During our early applications of UHb-DWI to a small number of healthy subjects, we observed different signal-b behaviors, particularly with different high-b decay constant, at different white-matter tracts and vertebral levels. This may be because of different means of axonal diameters and/or different fractions of nodes of Ranvier in different tracts. Our preliminary measurement on these normal CSCs demonstrates a fairly constant pattern. Thus, the purpose of this report is to study the signal behavior of

the UHb-rDWI signal at different tracts and levels of the *in vivo* cervical spinal cord of healthy volunteers and MS patients and validate the reproducibility of the technique by scanning each subject twice.

5.3 Methods

5.3.1 MRI Experiments

After approval from local institutional review board and informed consent, UHb-rDWI experiments were performed twice on four healthy volunteers (HC1, HC2, HC3, and HC4) in the interval of 2 months and three times on two relapsing/remitting MS (RRMS) patients (MS1 and MS2) in the interval of 7 months on a Siemens 3T MRI system (Trio, Siemens Medical Solutions, Erlangen, Germany). Each subject was positioned with cervical segment of the spinal cord as straight as possible from the anterior/posterior view.

MS1 was a 48-year-old male with RRMS of 14 years duration but not on immunotherapy for the past 5 years, who developed new onset of right lower extremity paresthesias and right leg weakness associated with unsteady ambulation. On the clinical T2WI, an intramedullary lesion was detected at the C3-C4 level. He was given methylprednisolone 1000 mg IV each day for 3 days after the first research UHB-rDWI study (after day 11), and the symptoms were resolving with improved strength and ambulation at time of the day 60 MRI exam. At day 200, the patient had returned to baseline clinical status.

MS2 was a 22-year-old female with RRMS of 4 years duration, who was also not on immunotherapy. She presented with an acute relapse manifested by impaired balance

and sensory complaints. The initial clinical MRI of the CSC revealed a new contrast-enhancing lesion in the posterior spinal cord at the C2-C3 level. She underwent treatment with 1000 mg of methylprednisolone every day for 3 days. Serial research imaging was performed on days 32, 75 and 210. The patient recovered to baseline over a 4-month time period.

At first, T2-weighted images of cervical spinal cord (CSC) were acquired in axial plane (TR/TE–4 s/ 95 ms and acquisition resolution 0.68×0.55×4.0 mm^3) and sagittal plane (TR/TE–4 s/112 ms and acquisition resolution 0.92×0.69×3.0 mm^3) using a turbo spin-echo (TSE) for planning the UHb-rDWI experiment. Then axial (diffusion gradient applied perpendicular to the spinal cord) high-b diffusion weighted images were acquired using our specifically developed 2D single-shot Diffusion-Weighted Stimulated Echo-Planar Imaging with Reduced Field of View (2D ss-DWSTEPI-rFOV) pulse sequence (15) and 8 channel (6 channel posterior and 2 channel anterior) CSC dedicated phased array RF receive-only coil (125). The imaging parameters were TR/TE = 3 s/64 ms, FOV read/phase = 128x44 mm^2, acquisition time = 6 min 19 sec, number of averages = 6, number of slices = 21, and voxel dimension = 1.0x1.0x4.0 mm^3. Diffusion-weighting was applied in left-right direction with 7 b-values: 573, 1702, 2832, 3691, 5090, 6219, and 7348 s/m^2 using fixed amplitude (38 mT/m) and duration (12 ms) of the diffusion gradient while varying mixing times TMs (time interval between 2^{nd} and 3^{rd} 90° RF pulses) with 9, 85, 161, 237, 313, 389, 465 ms, respectively. Spatial saturation bands were applied anterior and posterior of the CSC to suppress the signal contamination from outside of the FOV. An additional b_0 image without diffusion weighting gradient (b ~ 0 sec/mm^2) was obtained corresponding to each TM for correcting T_1 decay during TM.

5.3.2 T_1 Correction

In 2D ss-DWSTEPI imaging, diffusion-weighted longitudinal magnetization undergoes T_1 decay during the mixing-time. The signal equation for b-value images (S_b) and b_0 images (S_{b_0}) incorporating the diffusion and T_1 decay effects are:

$$S_b = (S_{EA}^0 e^{-bD_L} + S_{IA}^0 e^{-bD_H}) e^{-TM/T_1} \quad [5.2]$$

$$S_{b_0} = S_0\, e^{-TM/T_1} \quad [5.3]$$

where S_0 is the signal measured without T_1 and diffusion decay, and D is an apparent diffusion coefficient (ADC). The b-value signal undergoes both diffusion and T_1 decay, while b_0 signal undergoes only T_1 decay. The pure diffusion signal is obtained by dividing Eq. [5.2] by Eq. [5.3].

5.3.3 Curve Fitting

All DICOM images were postprocessed using home–built processing software written in python language. The signals from each pixel of b_0 image were fitted with bi-exponential function as suggested by Soellinger et al. (126) while those from b-value images were fitted with either biexponential (127,128) or monoexponential plus constant function (129) depending on a signal that best fits to either of these functions and the curves were normalized to the S_0. In particular, for demyelination pixel such as in MS lesion, where $S_{IA}^0 / (S_{IA}^0 + S_{EA}^0) < 0.1$, the signal-b curve is fit to a monoexponential plus constant function. The diffusion only curve is obtained by dividing the normalized fitted curve of each pixel of b-value images that has both T_1 and diffusion decay by corresponding normalized fitted curve of b_0 images that have only T_1 decay.

5.3.4 Monte-Carlo Simulation (MCS)

We performed a Monte-Carlo simulation of water diffusion for an one-dimensional white-matter tract using our home-developed MCS software, to understand the behavior of signal-b curve at UHb region. We introduced different permeability values from 0 to 100 μm/sec for the water exchange effect between IA and EA spaces to the signal-b curve.

5.4 Results

The series of b-value images at C3-C4 level of four volunteers (top series: volunteer HC1, middle series: volunteers HC2 and HC3, and bottom series: volunteer HC4) corresponding to the seven b-values are shown in Figures 5.1(a-d). Greater contrast between white-matter and gray-matter is seen at higher-b rDWI. At b_{max} = 7348 s/mm^2, GM signal drops to noise level while enough WM signal is preserved.

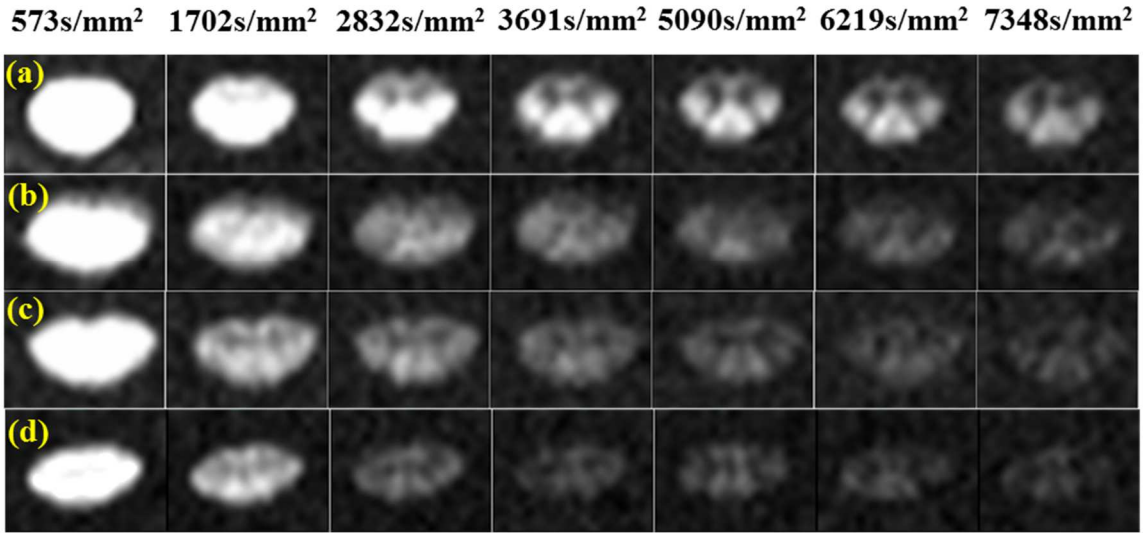

Figure 5.1: Series of b-value images at C3-C4 vertebral level slice in volunteers: (a) HC1, (b) HC2, (c) HC3, and (d) HC4.Clear contrast between white- and gray-matter is observed at high-b value images.

The rDWI signal-b curves of 4 volunteers at different levels of the CSC: upper curves at C2-C3 level, middle at C4 level, and bottom at C5 level shown in Figure 5.2. The curves at 1st, 2nd, 3rd, and 4th columns are of volunteers HC1, HC2, HC3, and HC4, respectively. Four one-point pixel (1x1x4 mm^3) ROIs: two on the lateral funiculus (points 1 and 2) and two on the posterior funiculus (points 3 and 4) were taken for plotting signal-b curves. These points were chosen ensuring minimal signal contamination from boundary and GM due to partial volume effects. We see that the signal-b curves decay at initial-b values and reach a nearly constant curve at high-b values. The plateau height of the curve varies slightly between different tracts within the same spinal cord section and

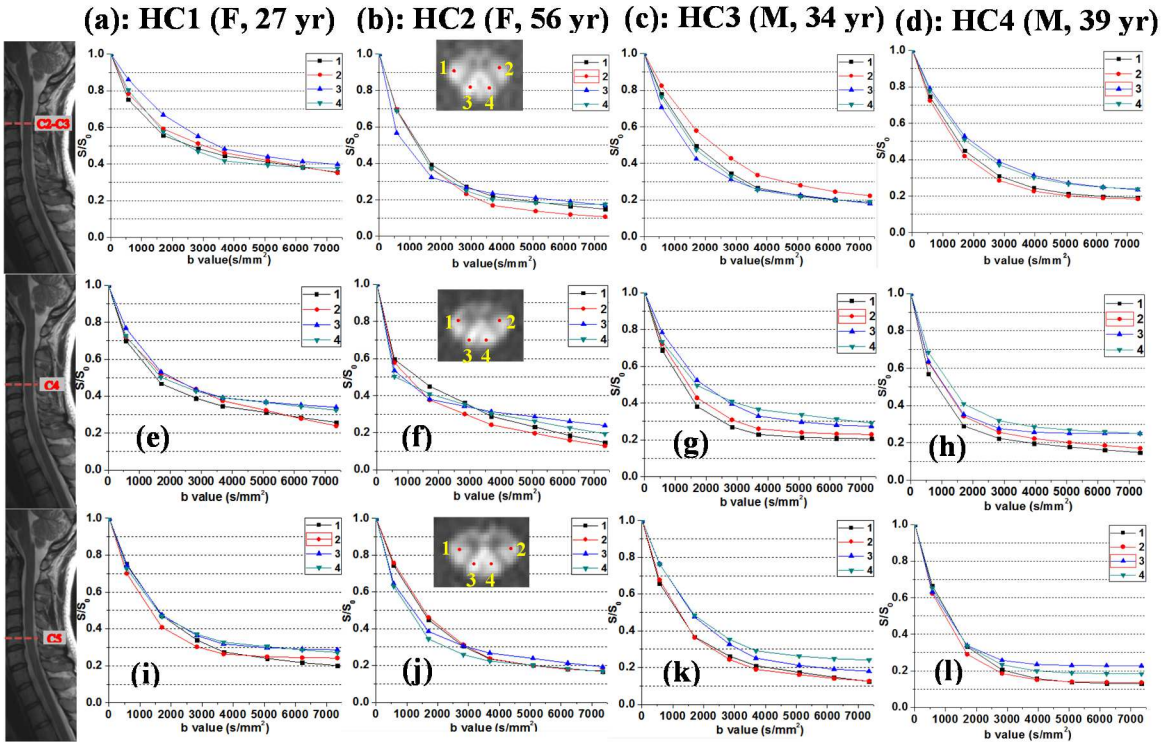

Figure 5.2: rDWI signal-b plots of volunteers: (a, e, i) HC1, (b, f, j) HC2, (c, g, k) HC3, and (d, h, l) HC4 at C2-C3, C4, and C5 levels, respectively. The red dotted line on the sagittal image at the left show these levels. Four point ROIs were chosen: two on lateral columns (1, 2) and two on posterior columns (3, 4). The plots on the left and right side of the cord within the same section are almost identical.

on different vertebral levels while it is similar on the left and right tracts within the same section. Moreover, the plateau heights in the lateral and posterior columns of one volunteer, a younger female, are consistently higher than those of the other healthy subjects most prominently at C3-C4 level and to a lesser extent at the middle C4 as well as C5 levels. This intersubject variability on the plateau of the signal-b curve may be due to various factors including age, gender, and/or cord morphology.

The comparison of signal-b curve at two successive scans of volunteer HC1 at C3-C4 level is illustrated in Figure 5.3. The plots are consistent in two time points. The consistency over time was also observed at other vertebral levels. This reproducibility of signal-b curves behavior between two time points was observed in all vertebral levels of other volunteers. Figures 5.3(a-b) are the representative of all curves at different levels of all volunteers under study. Figure 5.3c shows the scatter plot of D_H values measured at four regions: two on the lateral funiculus with diamond shaped 5 pixel ROIs centered at point 1 and 2 (shown in rDW image in Figure 5.3a) and two on posterior funiculus with

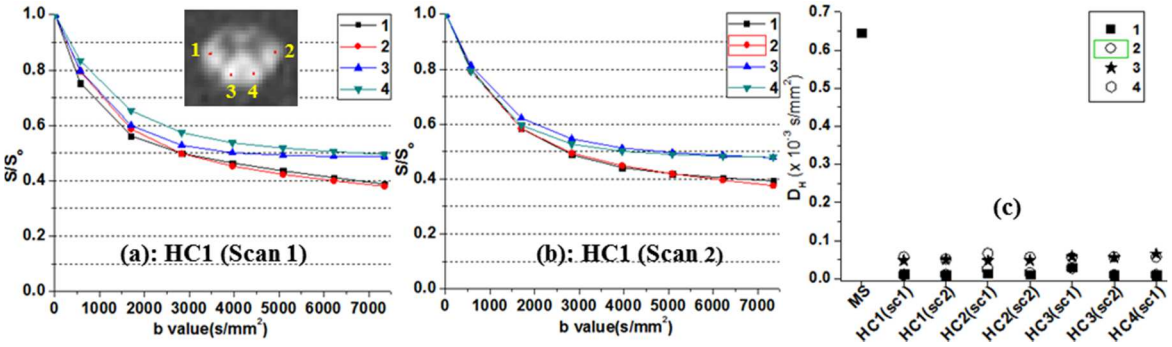

Figure 5.3: rDWI signal-b plot comparison between two scans: (a) scan 1 and (b) scan 2 at C3-C4 level in HC1. The plots are consistent in two successive scans, indicating high reproducibility of the measurement. Similar behavior of the curve was seen on all levels of the spinal cord and on other volunteers HC2, HC3, and HC4. (c)D_H values measured at two regions of the lateral columns (1, 2) and at two points of the posterior columns (3, 4). Five-pixel ROIs (diamond shaped) at lateral columns and 3-pixel ROIs (on vertical line) at posterior columns are used to measure D_H.

3-pixel ROIs on vertical line centered at points 3 and 4. Both curves and D_H values are nearly identical on left and right tracts and in two scans. The D_H values measured on these 4 regions in C2-C3, C4, and C5 levels of all volunteers are listed in Table 5.1 and plotted in Figure 5.4. The D_H values of the healthy volunteers at C3-C4 level are compared with the D_H value from a lesion on right lateral column of MS patient at C3-C4 level. This preliminary study demonstrates that variability in the D_H values of healthy controls is low compared to the D_H value in the lesion from the MS patient. Figure 5.5a shows the plot of diffusion-weighted signal calculated using the position data of MCS for twenty b-values (0~ 40,000 sec/mm^2) for two different diffusion times (Δ = 50 and Δ = 200 ms) and Figure 5.5b represents the curves that show the variation of D_H with a series of permeability P (0 ~ 100 μm/sec) for two diffusion times. The high-b decay constant D_H is calculated by fitting the signal-b curve to an exponential curve at b >5,000 sec/mm^2.

Table 5.1: D_H values measured at two regions of the lateral columns (RLC and LLC: right and left lateral columns) and two regions of the posterior columns (RPC and LPC: right and left posterior columns) on C2-C3, C4, and C5 vertebral levels in all volunteers. Five-pixel ROIs (diamond shaped) at lateral column and 3-pixel ROIs (on vertical line) at posterior column are used to measure D_H.

volunteers	Levels	RLC	LLC	RPC	LPC
HC1	C2-C3	0.0533	0.0478	0.0100	0.0100
HC2		0.0939	0.0920	0.0353	0.0222
HC3		0.0951	0.0877	0.0100	0.0100
HC4		0.0363	0.0332	0.0541	0.0572
HC1	C4	0.0732	0.0705	0.0632	0.0664
HC2		0.0904	0.0828	0.0626	0.0658
HC3		0.0252	0.0243	0.0391	0.0291
HC4		0.0868	0.0887	0.0648	0.0544
HC1	C5	0.0375	0.0246	0.0127	0.0162
HC2		0.0451	0.0314	0.0436	0.0375
HC3		0.0571	0.0519	0.0286	0.0269
HC4		0.0786	0.0488	0.0194	0.0182

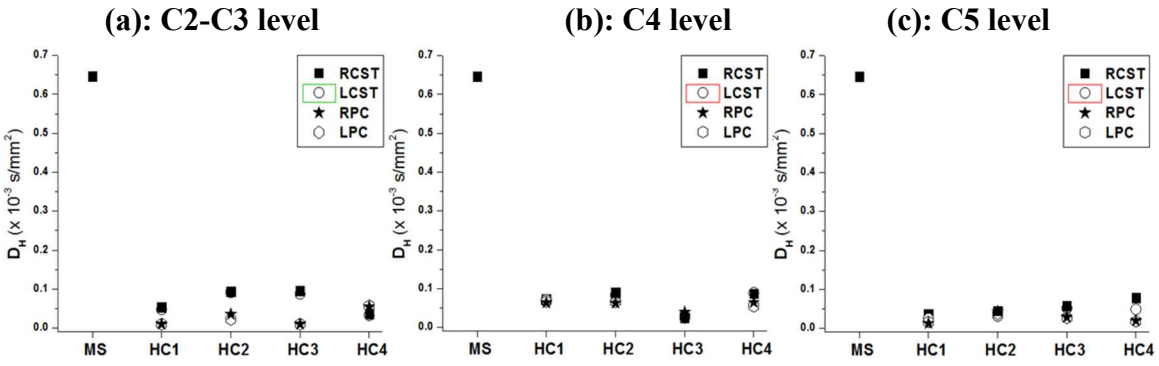

Figure 5.4: Scatter plot of D_H values of Table 5.1 of 4 healthy volunteers at (a) C2-C3, (b) C4 level, and (c) C5 levels. The D_H values of the control volunteers at different levels are compared with that obtained from multiple sclerosis (MS) patient with lesion on right lateral column at C3-C4 level.

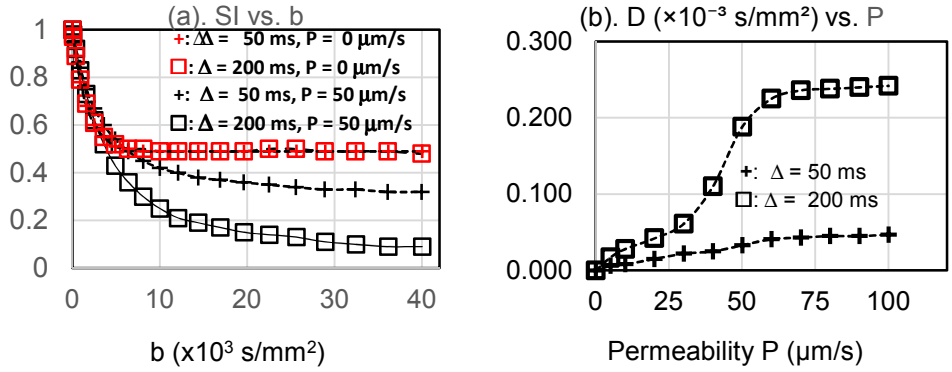

Fig. 5.5: Numerical diffusion-weighting with a short (50 ms) and long (200 ms) diffusion times: (a) signal-b curves and (b) decay constant (D_H) vs. permeability P. The plots with red and black markers in (a) represent P = 0 and 50 µm/sec permeability, respectively. (b) The decay constant D_H (calculated at b > 5,000 s/mm^2) versus permeability plot for diffusion times $\Delta = 50$ ms and $\Delta = 200$ ms.

The first RRMS patient (MS1) was imaged three times within 200 days at days 11, 60, and 200 with UHb-rDWI. The sagittal (1st three images) and axial image (4th image) of the CSC in Figure 5.6 demonstrated a new enhancing, T_2 hyperintense lesion in the right lateral column at the C3-C4 level (denoted by a red dotted line in the sagittal images) as well as an old T_2 hyperintense, nonenhancing lesion in the left posterior column (indicated by two red arrows in the axial image). The plots in Figure 5.7 indicate the time evolutions of signal-b curves of two selected contralateral pixels (denoted by two small red circles), including a pixel within lesion. The UHb-rDWI signal in the selected pixel in Figure 5.7a shows a prominent decaying pattern compared to the decay pattern for the contralateral pixel (Figure 5.7b). In Figure 5.7a, the blue signal-b curve of the lesion at day 200 approaches that of the normal region, which is concordant with the patient's return to clinical baseline. Interestingly, UHb-rDWI of the relatively unaffected contralateral lateral column exhibited signal intensity curves similar to those of the normal volunteers. Figure 5.7c demonstrates that at b values greater than 4000 sec/mm^2, the acute right lateral column lesion and the older left posterior column lesion show rapid decay as compared to the healthy CSC. Over 200 days, the D_H values approach that of the healthy CSC.

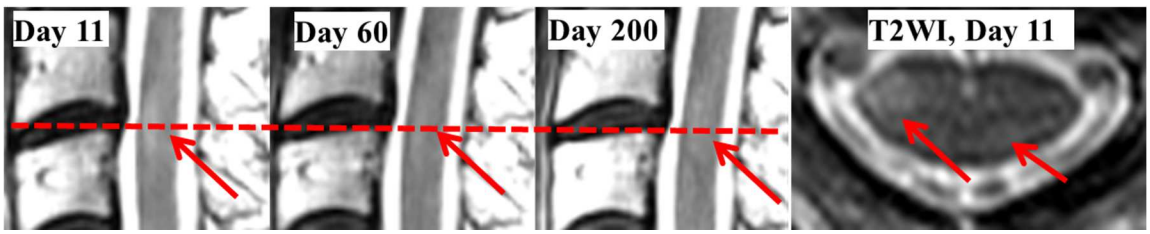

Figure 5.6: Sagittal T2WI images at days 11, 60, 200 and axial image at day 11 of patient MS1. The T_2 hyperintense lesion in right lateral column at C3-C4 level is indicated by red arrow.

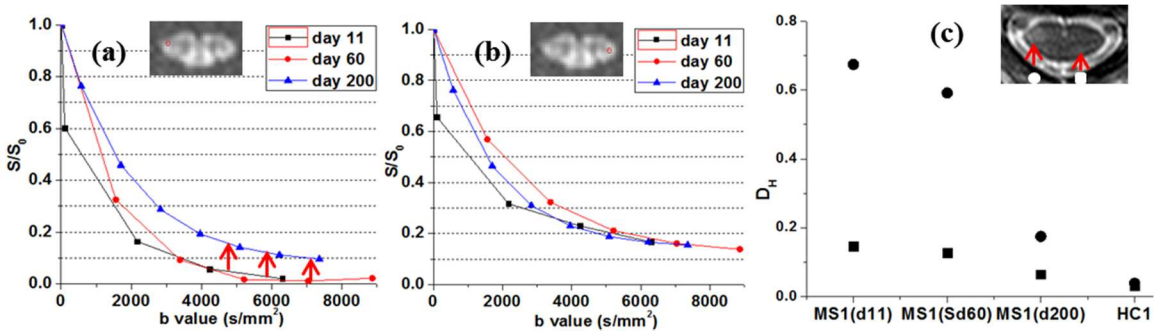

Figure 5.7: The signal-b curves of two single pixel ROIs of MS1 at (a) the lesion region and (b) the normal region of the lateral column evolve over days 11, 60 and 200 after an acute attack. The curve in the lesion increases toward that of normal in day 200. (c) At b values greater than 4000 mm^2/s, the D_H values measured in lesion approach those of the healthy CSC (HC1) over 200 days.

The second RRMS patient (MS2) was imaged three times at days 32, 75, 210 after an acute attack at day 1. The sagittal T2WI showed an ovoid hyperintense lesion in the posterior column at the C2 level when she presented after an acute attack (Figure 5.8). The craniocaudal extent and conspicuity of the lesion decreased over the serial scans. The T_2 hyper-intensity indicates increased parenchymal water content only. Figure 5.9a shows evolution of the signal-b curves in the posterior column lesion over time, while Figure 5.9b shows evolution of the signal-b curves in the right lateral column during the same time period. The curves for days 32 and 75 in Figure 5.9a mimic rDWI with increased water exchange between IA and EA spaces, as is seen with a demyelinated nerve. The signal-b curve at day 210 has approached normal values. The right lateral column also demonstrated abnormal UHb-rDWI extending over multiple levels (C1-C3), although this area did not reveal abnormal T_2 signal intensity. Figure 5.9c shows that at b-values greater than 4000 s/mm^2, the acute posterior column lesion and lateral columns demonstrate high value of D_H as compared to the healthy CSC. On day 210, the D_H values approach those of the healthy CSC.

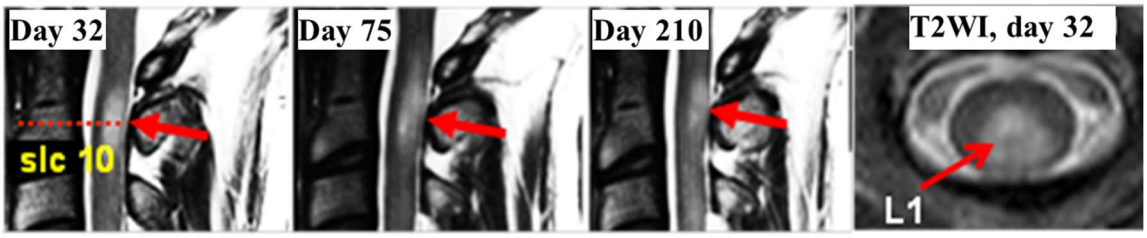

Figure 5.8: Sagittal T2WI images at days 32, 75, 210 and axial image at day 32 of patient MS2. The posterior column T2 hyperintense lesion (red arrow) is decreased in size over a 200-day period.

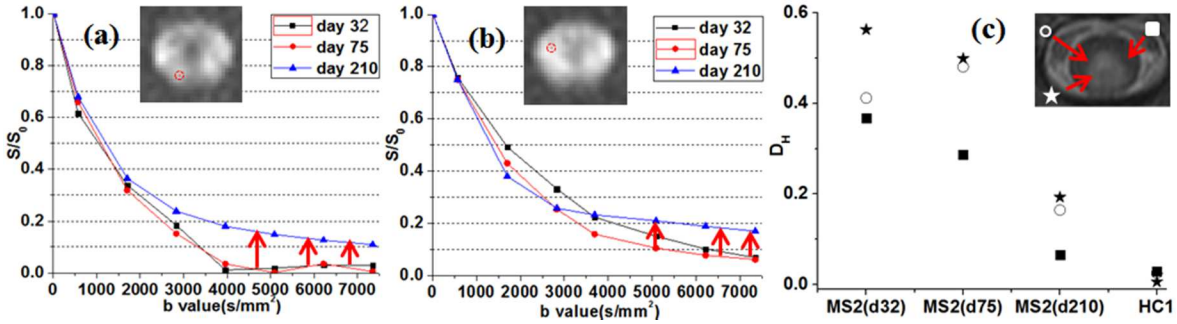

Figure 5.9: Signal-b curves of two single pixels, (a) one in posterior column lesion and (b) right lateral column over same time period. The curve at day 210 is increased toward that of normal. (c) At b values greater than 4000 mm^2/s, the D_H values measured in the acute posterior column lesion and lateral column white-matter are comparable to that of healthy CSC (HC1) over 200 days.

5.5 Discussion

The UHb-rDWI technique using a CSC dedicated coil allows us to acquire high resolution UHb-rDW images of the CSC in four healthy control volunteers and two RRMS patients with clear distinction between WM and GM at high b diffusion MRI. The increased GM-WM contrast at high b is mainly due to the non-monoexponential signal behavior in the WM (127,129). Our MCS result predicts the constant signal intensity in UHb-rDW images of white-matter with no water exchange between the intra- and extra-axonal spaces, although we have been observing decaying signal with respect to b-value

at high b. The signal intensity of b-value images of volunteer HC1 is higher than that of others. This may be due to factors such as different tuning, coupling, loading of the RF coil, and depth of the spinal cord from the skin surface.

The signal-b curve plotted at various levels of spinal cord in healthy volunteers shows the biexponential decay behavior, i.e., fast exponential decay at lower b-values and much slower decay at high b region, say $b > 4{,}000 s/mm^2$ in a clinical MRI system using a CSC dedicated RF coil. The diffusion signal from the EA space decays with increasing b-values while that from the IA space decays very slowly at high-b for the normal healthy spinal cord. Thus, the behavior of signal-b curve at low b-value is mainly predominated by fast decay of diffusion signal from EA space while at UHb-value the signal behavior is governed solely by the constant or slow-decaying signal from IA space. This may be explained as follows. The axons in the healthy spinal cord are surrounded by the myelin layers which prohibit or greatly limit the exchange of water molecules between IA and EA spaces. The applied radial diffusion-weighting does not create a noticeable phase dispersion that is responsible for signal decay for the spins in restricted water molecules in the IA space whose motion along the radial direction is limited by axonal diameter (~ 1.2 μm) while it does create a phase dispersion for the spins in mobile water molecules in EA space where water can move over the hindered boundaries including the membranes. The myelin water does not contribute to the signal intensity of DW images because of relatively long TE used in the experiment compared to the short T_2 of myelin water.

We hypothesize that the slow decaying component of the signal-b curve corresponds to the axonal density, which is slightly different in different tracts within a spinal cord section. This may be due to the differences in axonal diameter, fiber packing

density between different tracts (130–132) of the section, different leakage effect due to variations in myelination of the myelinated segment, and fractions of node of Ranvier. The slightly decaying pattern of the UHb signal may be due to leakage of water molecule via nodes of Ranvier, application of imperfect rDW gradients, imperfect shielding of water by myelin, angular dispersion of axons within an imaging voxel, and technical problem such as asynchronous motion between the table and the subjects during DWI experiment. Note that each myelin segment is about 100 μm long for a 1 μm diameter axon, and a gap between two adjacent myelin sheaths, the node of Ranvier, is in the range of 0.8 to 1 μm (133).

The MCS performed to evaluate the effect on the signal-b curve by exchange effect between IA and EA spaces for two different diffusion times of 50 and 200 ms as shown in Figure 5.5 indicates the exponential decay of signal b curve with b value due to permeability. It can also be seen that for zero permeability, the decay constant is identical for both diffusion times, as indicated by red markers in Figure 5.5a; however, the sensitivity of the D_H to the exchange rate is dramatically increased with longer diffusion time, as shown in Figure 5.5b. This result indicates that DWI with extended diffusion time, using diffusion-weighted stimulated-echo, is needed to sensitize the water-exchange effect. In principle, the plot of Figure 5.5b can be used to estimate the mean permeability within an imaging voxel.

As depicted in Figure 5.3C, Figure 5.4, and Table 5.1, the D_H values measured on the left and right side of the lateral and posterior columns within the same section of cord are almost identical. The mean value of D_H with inter/intrasubject standard deviation on lateral columns was $(0.0607 \pm 0.02531)\ 10^{-3}$ sec/mm^2 and that on posterior columns was

(0.0357 ± 0.02072) 10^{-3} sec/mm^2 which is close to the ADC value (0.068 ± 0.021) 10^{-3} sec/mm^2 reported by Rangwala et al. (24) on white-matter. The mean D_H is smaller in the posterior column than that in the lateral column which agrees with Rangwala's result. The UHb-rDWI signal curve of the normal controls was consistent in all vertebral levels on two successive scans. The curves are very similar on the left and right sides of every tract in the spinal cord. These results demonstrate high reproducibility and reliability of the technique. In D_H plots of healthy controls, their values are compared with the D_H value from a 5 pixel ROI in a lesion at C3-C4 level from a representative MS patient (MS1) participating in our preliminary studies to show that the inter/intrasubject variability of healthy controls is insignificant compared to the D_H at lesion. This indicates also that this imaging technique has strong potential for clinical imaging of the spinal cord in demyelinating disease and other disease states.

In the RRMS patients, the regions affected by active lesions revealed marked decrease in signal intensities in the UHb zone. A demyelinating lesion may enable the exchange of water molecules between IA and EA spaces, which results in an increase in the displacement of the IA water molecules during the diffusion time and consequently increased signal decay. In RRMS patients, UHb-rDWI revealed the extent of lesions in the CSC during acute relapse and over the course of the recovery period. Our MCS suggests that this rapid decay in the MS lesions and eventual increase towards the normal control curves indicates demyelination with axonal sparing and remyelination, respectively.

UHb measurements may be a powerful biomarker to monitor lesion evolution, recovery, and response to therapy. As spinal cord inflammation can resolve and

demyelination may be in part reparable secondary to remyelination while axonal loss is irreparable and the principal cause of disability in MS and related neurological diseases, it is crucial to establish a clear marker to distinguish demyelination from axonal loss. The height of the slow decaying component is useful in distinguishing the inflammation from demyelination. Based on MCS results, we can infer that the height of the plateau decreases with inflammation as the axonal density decreases with inflammation, while demyelination causes the signal-b curve to decay exponentially much like EA water. Using the same technique but with the diffusion gradient along axial direction (i.e., UHb-aDWI), we may be able to study the axonal degeneration (134,135). The height of the plateau is also very useful to evaluate the degree of remyelination in a lesion with axonal sparing, which is important with the emergence of the therapies that facilitate axonal remyelination.

This study has a few limitations. The advanced diffusion technique, UHb-rDWI, is a specialized protocol and has been adapted for 3T MRI. The optimal signal to noise ratio with the highest contrast and spatial resolution is achieved with proprietary CSC coils. Although the 7-minute sequence is feasible in the clinical realm, it does require good patient cooperation during the imaging. Our experience has revealed that the best imaging results are in the upper CSC where the spinal alignment is straight. With normal cervical lordosis in the mid and lower cervical spine, there can be field inhomogeneity with distortion. Therefore, adjustments must be made to accommodate for the cervical spine curvature below C4.

5.6 Conclusions

UHb-rDWI is effective, quantitative, qualitative, and reproducible in normal healthy volunteers and provides much deeper insight about the microscopic environment in the WM than the conventional DTI, which could be used for establishing an imaging biomarker to distinguish inflammation, demyelination and axonal loss in the spinal cord. The concordance of the clinical findings in correlation with serial UHb-rDWI signal-b plots of the lesions suggests the ability of UHB-rDWI to detect the evolution of demyelination with axonal sparing to axonal preservation with remyelination in MS lesions.

CHAPTER 6

CONCLUSIONS

6.1 Summary

This dissertation incorporates two separate subjects: 1) quantitative assessment of k_f in the heart of ox-treated SV lambs to study the effect of oxandrolone on the cardiac energy utilization and 2) study of signal behavior of UHb-rDWI signal in the cervical spinal cord of healthy and MS subjects.

^{31}P MRS is a noninvasive tool to measure the change in myocardial energy consumption due to oxandrolone in ox-treated SV lambs. In order to perform ^{31}P MRS in the lamb's heart, heart dedicated ^{1}H/^{31}P double tuned RF coil, T/R switches, and magnetization transfer ^{31}P MRS pulse sequence are required. We designed and built ^{1}H/^{31}P double tuned RF coil optimized at ^{31}P frequency and at the depth of the lamb heart, ^{1}H/^{31}P T/R switches, and high power RF switches for automatically directing RF pulses to the respective T/R switch. We modified 1D CSI-FID pulse sequence by adding OVS pulses with a user-selectable number of iterations, AHP RF pulse for excitation, and a train of MT pulses to saturate γ-ATP. We performed ^{31}P MT MRS for k_f measurements and cine MRI for measurement of the ejection fraction on lambs.

MRI is noninvasive and the most versatile technique that could be used for diagnosis, prognosis, multiple-site studies, and ultimate clinical trials of a variety of

neurological diseases associated with the spinal cord. However, MRI of the spinal cord is extremely challenging because of the small cross section of the spinal cord, motion, and susceptibility induced artifacts.

The conventional MRI techniques such as T_1 and T_2- weighted imaging that are used for structural MRI are known for their incapability to detect the disease at its early stage. The advanced MRI technique such as conventional diffusion MRI is not always consistent in detecting the axonal dysfunction. In this dissertation, we used 2D-ssDWSTEPI-rFOV and spinal cord dedicated phased array coil to acquire the rDWI signal from healthy control volunteers and the MS patients at different b values ranging from 573 to 7,348 s/mm^2. This sequence is immune to motion and susceptibility related artifacts due to the implementation of single shot acquisition and reduced field of view in the phase encoding direction features. The rDWI signal initially decreases exponentially with b value up to 4000 s/mm^2 and comes to a slowly decaying curve for the b values > 4000 s/mm^2 in the case of HCs. The high-b decay is markedly increased with reduced fraction at the lesion of MS patients. The decreased signal fraction from the IA space in MS patients is caused by the phase dispersal due to the exchange of water molecules between EA and IA spaces of the demyelinated axons of the lesion.

6.2 Conclusions

The T/R switch, high power RF switch, and lamb's heart dedicated ^{1}H/^{31}P double tuned RF coil enabled the acquisition of scout image for the localization and shimming and ^{31}P spectra from the lamb's heart. The T/R switch is versatile such that it can be made compatible to any T/R RF coils such as linear, quadrature, and double tuned coils

of any MR active nuclei. ^{31}P MT MRS and cine MRI data obtained from the limited number of lambs indicated the increased values of both k_f and EF on ox-treated shunted lamb compared to the shunted lamb.

The UHb-rDWI experiments performed on HC volunteers for multiple times show that the UHb-rDWI method is effective, quantitative, reproducible, and stable for quantitative evaluation of the spinal cord. The UHb-rDWI signal-b curves obtained from the active lesions of MS patients in three longitudinal time points after an acute attack show a remarkable decrease in signal intensities in the 1st and 2nd scans and noticeable recovery towards the normal in the last scan in concordance with the clinical recovery in these patients. The signal behavior of NAWM slice in the patents is similar to that of HC volunteers. This demonstrates the potential of UHb-rDWI method to study the evolution of lesions and the response to the medication.

6.3 Future Works

Although UHb-rDWI method from HC and MS patient data has demonstrated its potential to study the evolution of MS lesion with axonal sparing, there are still considerable latitudes to modify the technique for other neurological disorders. For instance many prior studies on animal spinal cords have shown the decrease in axial diffusivity for the cord with axonal loss. We can study the signal behavior of patients such as amyotrophic lateral sclerosis (ALS) patients by applying diffusion sensitized gradient along axial direction.

Although the UHb-DWI technique has shown its potential to quantitate the cord damage, we strongly feel a need to validate its findings on an animal by inducing a local

demyelination using lysolecithin, of which lesion typically evolves through, (i) active demyelination in 1-3 days, (ii) oligodendrocyte precursor cells recruitment in 3-7 days, (iii) oligodendrocyte differentiation during 7-10 days, and (iv) active remyelination during 10-21 days.

So far, we have been performing the UHb-DWI experiment with an MRI system equipped with 40 mT/m gradient strength for diffusion gradient. We should vary the mixing-time to achieve the long diffusion-time and high-efficiency of data acquisition, which requires correction of the T_1 decay in the measured signal. On the latest whole-body system with increased gradient strength and digital receiver, UHb-DWI technique will produce DWI with increased signal-to-noise ratio.

REFERENCES

1. Moeller HE, Wiedermann D. Magnetization-transfer ^{31}P NMR of biochemical exchange in vivo: application to creatine kinase kinetics. Spectroscopy 2002;16:207–216.

2. Joubert F, Mazet JL, Mateo P, Hoerter JA. ^{31}P NMR detection of subcellular creatine kinase fluxes in the perfused rat heart: Contractility modifies energy transfer pathways. J Biol Chem 2002;277:18469–18476. doi: 10.1074/jbc.M200792200.

3. Gonen O, Hu J, Stoyanova R, Leigh JS, Goelman G, Brown TR. Hybrid three dimensional (1D-hadamard, 2D-chemical shift imaging) phosphorous localised spectroscopy of phantom and human brain. Magn Reson Med 1995;33:300–306.

4. Silverthorn DU, Ober WC, Garrison CW, Silverthorn AC. Human physiology: an integrated approach. Prentice Hall; New Jersey 2001.

5. Abdel-Aziz K, Alexander DC, Assaf Y, et al. Quantitative MRI of the spinal cord. Academic Press; San Diego, CA 2014.

6. Meindl T, Wirth S, Weckbach S, Dietrich O, Reiser M, Schoenberg SO. Magnetic resonance imaging of the cervical spine: Comparison of 2D T2-weighted turbo spin echo, 2D T2*weighted gradient-recalled echo and 3D T2-weighted variable flip-angle turbo spin echo sequences. Eur Radiol 2009;19:713–721.

7. Oh J, Zackowski K, Chen M, et al. Multiparametric MRI correlates of sensorimotor function in the spinal cord in multiple sclerosis. Mult Scler J 2012;19:427–35.

8. Zollinger LV, Kim TH, Hill K, Jeong EK, Rose JW. Using diffusion tensor imaging and immunofluorescent assay to evaluate the pathology of multiple sclerosis. J Magn Reson Imaging 2011;33:557–564.

9. Wheeler-Kingshott CA, Hickman SJ, Parker GJ, Ciccarelli O, Symms MR, Miller DH, Barker GJ. Investigating cervical spinal cord structure using axial diffusion tensor imaging. Neuroimage 2002;16:93–102.

10. Elshafiey I, Bilgen M, He R, Narayana PA. In vivo diffusion tensor imaging of rat spinal cord at 7 T. Magn Reson Imaging 2002;20:243–247.

11. Dvorakova L, Jirik R, Burian M, Hejcl A, Starcuk Z. In vivo diffusion tensor imaging of the rat spinal cord at 9.4T. J Magn Reson Imaging 2008;27:634–642.

12. Jeong E-K, Kim S, Kholmovski EG, Parker DL. High-resolution DTI of a localized volume using 3D imaging (3D ss-DWSTEPI). Magn Reson Med 2006;56:1173–1181.

13. Jeong E-K, Kim S, Guo J, Kholmovski EG, Parker DL. High-resolution DTI with 2D interleaved multislice. Magn Reson Med 2005;54:1575–1579.

14. Jin N, Deng J, Zhang L, Zhang Z, Lu G, Omary RA, Larson AC. Targeted single-shot methods for diffusion-weighted imaging in the kidneys. J Magn Reson Imaging 2011;33:1517–1525.

15. Sapkota N, Shi X, Shah LM, Bisson EF, Rose JW, Jeong E-K. Two-dimensional single-shot diffusion-weighted stimulated EPI with reduced FOV for ultra-high-b radial diffusion-weighted imaging of spinal cord. Magn Reson Med 2016;77:2167–2173. doi: 10.1002/mrm.26302.

16. Storey P, Gimmi B, Chen XJ, et al. Magnetic resonance imaging methods and biologic applications. Humana Press Inc.; Totowa, New Jersey 2006.

17. Slichter CP. Principles of magnetic resonance. Springer; New York 1990.

18. Bloch F. Nuclear induction. Phys Rev 1946;70:460–473.

19. Jackson JD. Claasical electrodynamics. John Wiley & Sons, Inc.; Singapore 2002.

20. Liang Z-P, Lauterbur PC. Principles of magnetic resonance imaging. Spie optical engineering press; Washington 2000.

21. McRobbie DW, Moore EA, Graves MJ, Prince MR. MRI from picture to proton. Cambridge University Press; New York 2006.

22. Engle JL. Low noise broadband transmit/receive circuit for NMR. J Magn Reson 1980;37:547–549.

23. Mispelter J, Lupu M, Briguet A. NMR probeheads for biophysical and biomedical experiments. Imperial College Press; London 2006.

24. Fujita H, Zheng T, Yang X, Finnerty MJ, Handa S. RF surface receive array coils: the art of an LC circuit. J Magn Reson Imaging 2013;38:12–25.

25. Papoti D, Yen CC, Mackel JB, Merkle H, Silva AC. An embedded four-channel receive-only RF coil array for fMRI experiments of the somatosensory pathway in conscious awake marmosets. NMR Biomed 2013;26:1395–1402.

26. Nordmeyer-Massner JA, De Zanche N, Pruessmann KP. Noise figure characterization of preamplifiers at NMR frequencies. J Magn Reson 2011;210:7–15.

27. Hoult DI, Lauterbur PC. The sensitivity of the zeugmatographic experiment involving human samples. J Magn Reson 1979;34:425–433.

28. Hayes CE, Axel L. Noise performance of surface coils for magnetic resonance imaging at 1.5T. Am Assoc Phys Med 1985;12:604–607.

29. Li L, Kruger RA. An electrodeless measuring technique for determining conductivity of biological tissues at radio frequencies. Phys Med Biol 1988;33:1443–1452.

30. Hayes CE, Axel L. Noise performance of surface coils for magnetic resonance imaging at 1.5 T. Med Phys 1985;12:604–607.

31. Gilbert KM, Scholl TJ, Chronik BA. RF coil loading measurements between 1 and 50 MHz to guide field-cycled MRI system design. Concepts Magn Reson Part B 2008;33B:177–191.

32. Roemer PB, Edelstein WA, Hayes CE, Souza SP, Mueller OM. The NMR phased array. Magn Reson Med 1990;16:192–225.

33. Keil B, Wald LL. Massively parallel MRI detector arrays. J Magn Reson 2013;229:75–89.

34. Stejskal EO, Tanner JE. Spin diffusion measurements: spin echoes in the presence of a time-dependant field gradient. J Chem Phys 1965;42:288–292.

35. Basser PJ, Mattiello J, LeBihan D. MR diffusion tensor spectroscopy and imaging. Biophys J 1994;66:259–267.

36. Alexander AL, Lee JE, Lazar M, Field AS. Diffusion tensor imaging of the brain. Neurotherapeutics 2007;4:316–329.

37. Song S-K, Sun S-W, Ramsbottom MJ, Chang C, Russell J, Cross AH. Dysmyelination revealed through MRI as increased radial (but unchanged axial) diffusion of water. Neuroimage 2002;17:1429–1436.

38. Seo HS, Chang KH, Na DG, Kwon BJ, Lee DH. High b-value diffusion (b = 3000 s/mm^2) MR imaging in cerebral gliomas at 3T: visual and quantitative comparisons with b = 1000 s/mm^2. Am J Neuroradiol 2008;29:458–463.

39. Thapa B, Sapkota N, Lee Y, Kim E, Rose J, Shah LM, Jeong E-K. Signal behavior of ultra-high-b radial DWI (UHb-rDWI) signal in different tract of the cervical spinal cord. In Proceedings of the 25th Annual Meetings of ISMRM. Honolulu, Hawaii, USA; 2017. Abstract 1876.

40. Zhang H, Sun A, Li H, Saiviroonporn P, Wu EX, Guo H. Stimulated echo diffusion weighted imaging of the liver at 3 Tesla. Magn Reson Med 2017;309:300–309.

41. Merboldt K-D, Hanicke W, Frahm J. Self-diffusion NMR imaging using stimulated echoes. J Magn Reson 1985;64:479–486.

42. Merboldt K-D, Hanicke W, Frahm J. Diffusion imaging using stimulated echoes. Magn Reson Med 1991;19:233–239.

43. Tanner JE. Use of the stimulated echo in NMR diffusion studies. J Chem Phys 1970;52:2523–2526.

44. Ha S, Hamamura MJ, Nalcioglu O, Muftuler LT. A PIN diode controlled dual-tuned MRI RF coil and phased array for multi nuclear imaging. Phys Med Biol 2010;55:2589–2600.

45. Giovannetti G, Frijia F, Hartwig V, et al. Design of a quadrature surface coil for hyperpolarized ^{13}C MRS cardiac metabolism studies in pigs. Concepts Magn Reson Part B 2013;43B:69–77.

46. Robin A, Graaf D. In vivo NMR spectroscopy. John Wiley & Sons, Ltd.; Connecticut 2007.

47. Meyerspeer M, Roig ES, Gruetter R, Magill AW. An improved trap design for decoupling multinuclear RF coils. Magn Reson Med 2014;72:584–590.

48. Yan X, Xue R, Zhang X. A monopole / loop dual-tuned RF coil for ultra-high field MRI. Quant Imaigng Med Surg 2014;4:225–231.

49. Brand RC, Webb AG, Beenakker J-WM. Design and performance of a transformer-coupled double resonant quadrature birdcage coil for localized proton and phosphorus spectroscopy in the human calf muscle at 7 T. Concepts Magn Reson Part A 2013;42A:155–164.

50. Alfonsetti M, Sotgiu A, Alecci M. Design and testing of a 1.5 Tesla double-tuned ($^{1}H/^{31}P$) RF surface coil with intrinsic geometric isolation. Measurement 2010;43:1266–1276.

51. Asfour A. Design and development of a new dedicated RF sensor for the MRI of rat brain. J Biomed Sci Eng 2010;3:167–180.

52. Potter W, Wang L, McCully K, Zhao Q. Evaluation of a new $^{1}H/^{31}P$ dual-tuned birdcage coil for ^{31}P spectroscopy. Concepts Magn Reson Part B 2013;3:90–99.

53. Kaggie JD, Hadley RJ, Campbell JR, Daniel PJ, Parker DL, Morrell G, Newbould RD, Wodd AF, Bangerter NK. A 3T sodium and proton composite array breast coil.

Magn Reson Med 2014;6:2231–2242.

54. Alecci M, Romanzetti S, Kaffanke J, Celik A, Wegener HP, Shah NJ. Practical design of a 4 Tesla double-tuned RF surface coil for interleaved ^{1}H and ^{23}Na MRI of rat brain. J Magn Reson 2006;181:203–211.

55. Street AM. RF switch design. In Proceedings of How to design RF circuits, IEE training course. Vol. 4; 2000. pp. 1–7.

56. Subramanian VS, Epel B, Mailer C, Halpern HJ. A passive dual-circulator based transmit/receive switch for use with reflection resonators in pulse EPR. Concepts Magn Reson Part B 2009;35B:133–138.

57. Tokumitsu T, I. T, Aikawa M. A low voltage high-power T/R switch MMIC using LC resonators. In Proceedings of Microwave and milimeter wave monolithic circuits symposium, IEEE. Atlanta, GA, USA; 1993. pp. 27–30.

58. Naegle KM, Gupta S, Allstot DJ. Design considerations for a 10 GHz cmos transmit-receive switch. In Proceedings of IEEE International Symposium on Circuits and Systems. Kobe, Japan; 2005. pp. 2104–2107. doi: 10.1109/ISCAS.2005.1465034.

59. Spence D, Macro A. Custom MEMS switch for MR surface coil decoupling. In Proceedings of the 23rd Annual Meeting of ISMRM. Toronto, Ontario, Canada; 2015. p. 704.

60. Doherty WE, Joose RD. The PIN diode circuit designers' handbook. Microsemi Corp.; Watertown MA 1999.

61. Kumar A, Bottomley PA. Optimized quadrature surface coil designs. MAGMA 2008;21:41–52.

62. Sosnovik DE, Dai G, Nahrendorf M, Rosen BR, Seethamraju R. Cardiac MRI in mice at 9.4 tesla with a transmit-receive surface coil and a cardiac-tailored intensity-correction algorithm. J Magn Reson Imaging 2007;26:279–287.

63. Adriany G, Gruetter R. A half-volume coil for efficient proton decoupling in humans at 4 tesla. J Magn Reson 1997;125:178–184.

64. Dabirzadeh A, Chang C-W, McDougall MP. An insertable P-31 RF coil for dual-frequency magnetic resonance imaging & spectroscopy. In proceedings of the 30th Annual International IEEE EMBS Conference. Vancouver, British Columbia, Canada; 2008. pp. 2036–2038.

65. Gerbennikov A. RF and microwave transmitter design. John Wiley & Sons; New Jersey 2011.

66. D.I. H. Fast recovery with a conventional probe. J Magn Reson 1969;57:394–403.

67. Matson GB, Vermathen P, Hill TC. A practical double-tuned $^{1}H/^{31}P$ quadrature birdcage headcoil optimized for ^{31}P operation. Magn Reson Med 1999;42:173–182.

68. Klomp DWJ, Kentgens APM, Heerschap A. Polarization transfer for sensitivity-enhanced MRS using a single radio frequency transmit channel. NMR Biomed 2008;21:444–452.

69. Fitzsimmons JR, Brooker HR and, Beck B. A comparsion of double tuned surface coils. Magn Reson Med 1989;10:302–309.

70. Schnall MD, Subramanian VH, Leigh JS, JR., Chance B. A new double tuned probe for concurrent ^{1}H and ^{31}P NMR. J Magn Reson 1985;65:122–129.

71. Xiao Y, Zhao Z, Qian Z, Zhou H. A high isolation switching unit for MRI system. Procedia Eng 2010;7:265–269.

72. Herlihy DJ, Collins A, Hajnal J. A multi-nuclear MRI system incorporating local T/R switches. In Proceedings of the 10th Annual Meeting of ISMRM. Honolulu, Hawaii, USA; 2002.

73. Hancock CL, Forbess JM. Surgical management of the single ventricle. Prog Pediatr Cardiol 2002;16:47–68.

74. Schwalbe-Terilli CR, Hartman DH, Nagle ML, Gallagher PR, Ittenbach RF, Burnham NB, Gaynor JW, Ravishankar C. Enteral feeding and caloric intake in neonates after cardiac surgery. Am J Crit Care 2009;18:52–57.

75. Anderson JB, Beekman RH, Eghtesady P, Kalkwarf HJ, Uzark K, Kehl JE, Marino BS. Predictors of poor weight gain in infants with a single ventricle. J Pediatr 2010;157:407–413.

76. Nydegger A, Bines JE, P. F. Energy metabolism in infants with congenital heart disease. Nutrition 2006;22:697–704.

77. Leitch CA. Growth, nutrition and energy expenditure in pediatric heart failure. Prog Pediatr Cardiol 2000;11:195–202.

78. Maria MV Di, Glatz AC, Ravishankar C, Quartermain MD, Rush CH, Nance M, Gaynor JW, Goldberg DJ. Supplemental tube feeding does not mitigate weight loss in infants with shunt-dependent single-ventricle physiology. Pediatr Cardiol 2013;6:1350–1356.

79. Fox-wheeler S, Heller L, Salata CM, Kaufman F, Loro ML, Gilsanz V, Haight M, Umman GC, Barton N, Church JA. Evaluation of the effects of oxandrolone on

malnourished hiv-positive pediatric patients. Pediatrics 1999;104:1–7.

80. Porro LJ, Herndon DN, Rodriguez NA, Jennings K, Klein GL, Mlcak RP, Meyer WJ, Lee JO, Suman OE, Finnerty CC. Five-year outcomes after oxandrolone administration in severely burned children : a randomized clinical trial of safety and efficacy. Am Coll Surg 2012;214:489–502.

81. Rosenfeld RG, Frane J, Attie KM, et al. Six-year results of a randomized, prospective trial of human growth hormone and oxandrolone in Turner syndrome. J Pediatr 1992;121:49–55.

82. Wilson DM, McCauley E, Brown DR, Dudley R. Oxandrolone therapy in constitutionally delayed growth and puberty. Pediatrics 1995;96:1095–1100.

83. Hart DW, Wolf SE, Ramzy PI, Chinkes DL, Beauford RB, Ferrando AA, Wolfe RR, Herndon DN. Anabolic effects of oxandrolone after severe burn. Ann Surg 2001;233:556–564.

84. Przkora R, Jeschke MG, Barrow RE, et al. Metabolic and hormonal changes of severely burned children receiving long-term oxandrolone treatment. Ann Surg 2005;242:384–391.

85. Wolf SE, Thomas SJ, Dasu MR, Ferrando A a, Chinkes DL, Wolfe RR, Herndon DN. Improved net protein balance, lean mass, and gene expression changes with oxandrolone treatment in the severely burned. Ann Surg 2003;237:801–811.

86. Reddy VM, Meyrick B, Wong J, Khoor A, Liddicoat JR. In utero placement of aortopulmonary shunts a model of postnatal pulmonary hypertension with increased pulmonary blood flow in lambs. Circulation 1995;92:606–613.

87. Neubaur S, P. FRC. The failing heart — an engine out of fuel. N Engl J Med 2007;356:1140–1151.

88. Bottomley PA, Hardy CJ. Mapping creatine kinase rates in human brain and heart with 4 tesla saturation transfer ^{31}P NMR. J Magn Reson 1992;99:443–448.

89. Bottomley PA, Ouwerkerk R, Lee RF, Weiss RG. Four-angle saturation transfer (FAST) method for measuring creatine kinase reaction rates in vivo. Magn Reson Med 2002;47:850–863.

90. Xiong Q, Li Q, Mansoor A, Jameel MN, Du F, Chen W, Zhang J. Novel strategy for measuring creatine kinase reaction rate in the in vivo heart. Am J Physiol Heart Circ Physiol 2009;297:H1010–H1019.

91. Schaer M, El-Sharkawy AMM, Weiss RG, Bottomley PA. Triple repetition time saturation transfer (TRiST) ^{31}P spectroscopy for measuring human creatine kinase

reaction kinetics. Magn Reson Med 2010;63:1493–1501.

92. Schär M, Gabr RE, El-Sharkawy A-MM, Steinberg A, Bottomley PA, Weiss RG. Two repetition time saturation transfer (TwiST) with spill-over correction to measure creatine kinase reaction rates in human hearts. J Cardiovasc Magn Reson 2015;17:1–11.

93. Bashir A, Gropler R. Reproducibility of creatine kinase reaction kinetics in human heart: a ^{31}P time-dependent saturation transfer spectroscopy study. NMR Biomed 2014;27:663–671.

94. Clarke WT, Robson MD, Neubauer S, Rodgers CT. Creatine kinase rate constant in the human heart measured with 3D-localization at 7 tesla. Magn Reson Med 2016. doi: 10.1002/mrm.26357.

95. Ugurbil K. Magnetization-transfer measurements of individual rate constants in the presence of multiple reactions. J Magn Reson 1985;64:207–219.

96. Kingsley-Hickman PB, Sako EY, Mohanakrishnan P, Robitaille PM, From AH, Foker JE, Uğurbil K. ^{31}P NMR studies of ATP synthesis and hydrolysis kinetics in the intact myocardium. Biochemistry 1987;26:7501–7510.

97. Kingsley PB, Monahan WG. Corrections for off-resonance effects and incomplete saturation in conventional (two-site) saturation-transfer kinetic measurements. Magn Reson Med 2000;43:810–819.

98. Jeong E-K, Sung Y-H, Kim S-E, Zuo C, Shi X, Mellon EA, F. RP. Measurement of creatine kinase reaction rate in human brain using magnetization transfer image-selected in vivo spectroscopy (MT-ISIS) and a volume ^{31}P/^{1}H radiofrequency coil in a clinical 3-T MRI system. NMR Biomed 2011;24:765–770.

99. Thapa B, Dahal M, Frank D, Burch P, Jeong E-K. Quantitative evaluation of the first-order rate constant of creatine-kinase reaction in ovine heart using magntization transfer ^{31}P Magnetic Resonance Spectroscopy (MT-^{31}P-MRS). In Proceedings of the 23rd Annual Meeting of ISMRM. Toronto, Ontario, Canada; 2015. Abstract 6071.

100. Thapa B, Kaggie J, Sapkota N, Frank D, Jeong E-K. Design and development of a general purpose transmit/recieve (T/R) switch for 3T MRI, compatible for a linear, quadrature and double tuned RF coil. Concepts Magn Reson Part B 2016;46B:56–65.

101. Adriany G, Gruetter R. A half-volume coil for efficient proton decoupling in humans at 4 tesla. J Magn Reson 1997;125:178–84.

102. Thapa B, Kaggie J, Sapkota N, Jeong E-K. Design and develpoment of general purpose transmit-receive (TR) switch for a linear, quadrature and dual tuned coils. In Proceedings of the 23rd Annual Meeting of ISMRM. Toronto, Ontario, Canada; 2015. Abstract 1784.

103. Weiss RG, Gerstenblith G, Bottomley PA. ATP flux through creatine kinase in the normal, stressed, and failing human heart. Proc Natl Acad Sci U. S. A. 2005;102:808–813.

104. Smith CS, Bottomley PA, Schulman SP, Gerstenblith G, Weiss RG. Altered creatine kinase adenosine triphosphate kinetics in failing hypertrophied human myocardium. Circulation 2006;114:1151–1158.

105. Abraham MR, Bottomley PA, Dimaano VL, Pinheiro A, Steinberg A, Traill TA, Abraham TP, Weiss RG. Creatine kinase ATP and phosphocreatine energy supply in a single kindred of patients with hypertrophic cardiomyopathy. Am J Cardiol 2013;112:861–866.

106. Luigino N, Friedrich J, Ronglih L, Paolo P, C. PA, S. IJ. Congestive heart failure/ventricular hypertrophy/valvular heart disease: enalapril treatment increases cardiac performance and energy reserve via the creatine kinase reaction in myocardium of Syrian myopathic hamsters with advanced heart failure. Circulation 1995;91:1824–1833.

107. Chesky JA, Rockstein M, Lopez T. Changes with age of myocardial creatine phosphokinase in the male fischer rat. Mech Ageing Dev 1980;12:237–243.

108. Chen C, Guerrero JL, Vazquez de Prada JA, et al. Intracardiac ultrasound measurement of volumes and ejection fraction in normal, infarcted, and aneurysmal left ventricles using a 10-MHz ultrasound catheter. Circulation 1994;90:1481–1491.

109. Wisneski J., Pfeil CN, George WD, Mitchell R, Rahimtoola S, Gertz EW. Left ventricular ejection fraction calculated from volumes and areas: underestimation by area method. Circulation 1981;63:149–151.

110. Rich S, Chomka E V, Stagl R, Shanes JG, Kondos GT, Brundage BH. Determination of left ventricular ejection fraction using ultrfast computed tomography. Am Heart J 1986;112:392–396.

111. Bellenger NG, Burgess MI, Ray SG, Lahiri A, Coats AJS, Cleland JGF, Pennell DJ. Comparison of left ventricular ejection fraction and volumes in heart failure by echocardiography, radionuclide ventriculography and cardiovascular magnetic resonance. Eur Heart J 2000;21:1387–1396.

112. Malayeri AA, Johnson WC, Macedo R, Bathon J, Lima JAC, Bluemke DA. Cardiac cine MRI: quantification of the realtionship between fast gradient echo and steady state free precession for determination of myocardial mass and volumes. J Magn Reson Imaging 20008;28:60–66.

113. Bergers E, Bot JCJ, De Groot CJ, Polman CH, Lycklama à Nijeholt GJ, Castelijns JA, van der Valk P, Barkhof F. Axonal damage in the spinal cord of MS patients occurs

largely independent of T2 MRI lesions. Neurology 2002;59:1766–1771.

114. Yuh WT, Marsh EE, Wang AK, Russell JW, Chiang F, Koci TM, Ryals TJ. MR imaging of spinal cord and vertebral body infarction. Am J Neuroradiol 1992;13:145–154.

115. Bammer R, Fazekas F, Augustin M, Simbrunner J, Strasser-Fuchs S, Seifert T, Stollberger R, Hartung H-P. Diffusion-weighted MR imaging of the spinal cord. Am J Neuroradiol 2000;21:587–591.

116. Facon D, Ozanne A, Fillard P, Lepeintre JF, Tournoux-Facon C, Ducreux D. MR diffusion tensor imaging and fiber tracking in spinal cord compression. Am J Neuroradiol 2005;26:1587–1594.

117. Le Bihan D, Mangin JF, Poupon C, Clark CA, Pappata S, Molko N, Chabriat H. Diffusion tensor imaging: concepts and applications. J Magn Reson Imaging 2001;13:534–46.

118. Arnold DL, Riess GT, Matthews PM, Francis GS, Collins DL, Wolfson C, Antel JP. Use of proton magnetic resonance spectroscopy for monitoring disease progression in multiple sclerosis. Ann Neurol 1994;36:76–82.

119. Shanmuganathan K, Gullapalli RP, Zhuo J, Mirvis SE. Diffusion tensor MR imaging in cervical spine trauma. Am J Neuroradiol 2008;29:655–659.

120. Maier SE, Mamata H. Diffusion tensor imaging of the spinal cord. Ann. N Y Accad Sci 2005;1064:50–60.

121. Sąsiadek MJ, Szewczyk P, Bladowska J. Application of diffusion tensor imaging (DTI) in pathological changes of the spinal cord. Med Sci Monit 2012;18:73–79.

122. Sapkota N, Yoon S, Thapa B, Lee Y, Bisson EF, Bowman BM, Miller SC, Shah LM, Rose JW, Jeong E-K. Characterization of spinal cord white-matter by suppressing signal from hindered space. A Monte Carlo simulation and an *ex vivo* ultra-high-b diffusion-weighted imaging study. J Magn Reson 2016;272:53–59.

123. Kim TH, Zollinger L, Shi XF, Kim SE, Rose J, Patel AA, Jeong E-K. Quantification of diffusivities of the human cervical spinal cord using a 2D single-shot interleaved multisection inner volume diffusion-weighted echo-planar imaging technique. Am J Neuroradiol 2010;31:682–687.

124. Lee Y, Thapa B, Sapkota N, Kim E, Shah LM, Jeong E, Rose JW. Ultra-high-b diffusion imaging of cervical spinal cord in multiple sclerosis. In Proceedings of the 25th Annual Meetings of ISMRM. Honolulu, Hawaii, USA; 2017. Abstract 2561.

125. Sapkota N, Thapa B, Lee Y, Kim T, Bisson EF, Shah LM, Rose JW, Jeong E. Eight-

channel decoupled array for cervical spinal cord imaging at 3T : six- channel posterior and two- channel anterior array coil. Concepts Magn Reson Part B 2016;46B:90–99.

126. Soellinger M, Langkammer C, Seifert-Held T, Fazekas F, Ropele S. Fast bound pool fraction mapping using stimulated echoes. Magn Reson Med 2011;66:717–724.

127. Yoshiura T, Wu O, Zaheer A, Reese TG, Gregory Sorensen A. Highly diffusion-sensitized MRI of brain: dissociation of gray and white-matter. Magn Reson Med 2001;45:734–740.

128. Niendorf T, Dijkhuizen RM, Norris DG, van Lookeren Campagne M, Nicolay K. Biexponential diffusion attenuation in various states of brain tissue: implications for diffusion-weighted imaging. Magn Reson Med 1996;36:847–857.

129. Rangwala NA, Hackney DB, Dai W, Alsop DC. Diffusion restriction in the human spinal cord characterized in vivo with high b-value STEAM diffusion imaging. Neuroimage 2013;82:416–425.

130. Onu M, Gervai P, Cohen-Adad J, Lawrence J, Kornelsen J, Tomanek B, Sboto-Frankenstein UN. Human cervical spinal cord funiculi: investigation with magnetic resonance diffusion tensor imaging. J Magn Reson Imaging 2010;31:829–837.

131. Ong HH, Wright AC, Wehrli SL, Souza A, Schwartz ED, Hwang SN, Wehrli FW. Indirect measurement of regional axon diameter in excised mouse spinal cord with q-space imaging: simulation and experimental studies. Neuroimage 2008;40:1619–1632.

132. Takahashi M, Hackney DB, Zhang G, Wehrli SL, Wright AC, O'Brien WT, Uematsu H, Wehrli FW, Selzer ME. Magnetic resonance microimaging of intraaxonal water diffusion in live excised lamprey spinal cord. In Proceedings of National Academy of Sciences of the United States of America. Vol. 99; 2002. pp. 16192–16196.

133. Hildebrand C, Remahl S, Persson H, Bjartmar C. Myelinated nerve fibers in the CNS. Prog Neurobiol 1993;40:319–384.

134. Pierpaoli C, Barnett A, Pajevic S, Chen R, Penix L, Virta A, Basser P. Water diffusion changes in Wallerian degeneration and their dependence on white-matter architecture. Neuroimage 2001;13:1174–1185.

135. Wheeler-kingshott CAM, Cercignani M. About " axial " and " radial " diffusivities. Magn Reson Med 2009;61:1255–1260.